THE REST-FRAME OPTICAL PROPERTIES OF z ≃ 3 GALAXIES [1]

Alice E. Shapley and Charles C. Steidel[2]
Palomar Observatory, California Institute of Technology, MS 105–24, Pasadena, CA 91125

Kurt L. Adelberger
Harvard-Smithsonian Center for Astrophysics, 60 Garden Street, Cambridge, MA 02138

Mark Dickinson and Mauro Giavalisco
Space Telescope Science Institute, 3700 San Martin Drive, Baltimore, MD 21218

Max Pettini
Institute of Astronomy, Madingley Road, Cambridge CB3 0HA, UK

ABSTRACT

We present the results of a near-infrared imaging survey of $z \sim 3$ Lyman Break Galaxies (LBGs). The survey covers a total of 30 arcmin^2 and includes 118 photometrically selected LBGs with K_s band measurements, 63 of which also have J band measurements, and 81 of which have spectroscopic redshifts. Using the distribution of optical $\mathcal{R}$ magnitudes from previous work and $\mathcal{R} - K_s$ colors for this sub-sample, we compute the rest-frame optical luminosity function of LBGs. This luminosity function is described by an analytic Schechter fit with a very steep faint end slope of $\alpha = -1.85 \pm 0.15$, and it strikingly exceeds locally determined optical luminosity functions at brighter magnitudes, where it is fairly well constrained. The V-band luminosity density of only the observed bright end of the $z \sim 3$ LBG luminosity function already approaches that of all stars in the local universe.

For the 81 galaxies with measured redshifts, we investigate the range of LBG stellar populations implied by the photometry which generally spans the range 900–5500 Å in the rest-frame. The parameters under consideration are the star-formation rate as a function of time, the time since the onset of star-formation, and the degree of reddening and extinction by dust. While there are only weak constraints on the parameters for most of the individual galaxies, there are strong trends in the sample as a whole. With a wider wavelength baseline than most previous studies at similar redshifts, we confirm the trend that intrinsically more luminous galaxies are dustier. We also find that there is a strong correlation between extinction and the age of the star-formation episode, in

[1]Based on data obtained at the W.M. Keck Observatory, which is operated as a scientific partnership among the California Institute of Technology, the University of California, and NASA, and was made possible by the generous financial support of the W.M. Keck Foundation.

[2]Packard Fellow

the sense that younger galaxies are dustier and have much higher star-formation rates. The strong correlation between extinction and age, which we show is unlikely to be an artifact of the modeling procedure, has important implications for an evolutionary sequence among LBGs. A unified scenario which accounts for the observed trends in bright LBGs is one in which a relatively short period of very rapid star-formation (hundreds of $M_\odot$ yr^{-1}) lasts for roughly 50–100 Myr, after which both the extinction and star-formation rate are considerably reduced and stars are formed at a more quiescent, but still rapid, rate for at least a few hundred Myr. In our sample, a considerable fraction ($\sim 20\%$) of the LBGs have best-fit star-formation ages $\gtrsim 1$ Gyr, implied stellar masses of $\gtrsim 10^{10}$ $M_\odot$, and are still forming stars at ~ 30 $M_\odot$ yr^{-1}.

Subject headings: early universe — galaxies: high-redshift — galaxies: formation — galaxies: evolution — galaxies: stellar content — galaxies: starburst — infrared: galaxies — catalogs

1. INTRODUCTION

In the past few years, considerable progress has been made in our understanding of the nature of high redshift galaxies, driven mostly by the availability of large samples that have been photometrically selected using rest-frame UV spectral features. The largest existing sample at present is at $z \sim 3$, where it is efficient to use ground-based imaging through optical filters designed to isolate the Lyman limit spectral discontinuity at 912 Å in the rest-frame, and where the spectroscopic follow-up has proved to be straightforward because many important spectral features are well-placed at wavelengths where optical spectrographs are most sensitive (Steidel *et al.* 1996a, Steidel *et al.* 1999). Very deep Hubble Space Telescope (HST) imaging such as that provided by the Hubble Deep Fields has also proved to be very effective, using similar techniques for $z \gtrsim 2$ (Steidel *et al.* 1996b, Madau *et al.* 1996, Lowenthal *et al.* 1997). The HST data reach much deeper into the high redshift galaxy UV luminosity function, but are confined to very small areas on the sky; as such, the ground-based and space-based surveys have been largely complementary (cf. Steidel *et al.* 1999).

To date, most of the work on these high redshift galaxy samples has focused on the large-scale clustering properties of the galaxies (e.g., Adelberger *et al.* 1998, Giavalisco *et al.* 1998, Steidel *et al.* 1998, Giavalisco & Dickinson 2001), on the properties of individual galaxies as deduced from their spectra (e.g., Pettini *et al.* 1998, 2000, 2001), or on inferences concerning the universal star-formation history as deduced from the global UV luminosity density (e.g., Madau *et al.* 1996, Steidel *et al.* 1999, Meurer, Heckman, & Calzetti 1999, Adelberger & Steidel 2000). The strong clustering of the bright Lyman Break Galaxies (LBGs) has generally been interpreted as indirect evidence that the observed galaxies reside in relatively massive dark matter halos, but how these galaxies are linked to present-day galaxies is far from clear, and has been quite controversial. While

considerable, the directly-observed UV luminosity of LBGs is clearly very significantly modified by extinction (see Adelberger & Steidel 2000, hereafter AS2000, for an extensive discussion of this topic), and at best provides information on the instantaneous formation rate of O and B stars.

While the far-UV properties of the LBGs are the most straightforward to study observationally, it is also of interest to explore additional properties of these galaxies that require longer wavelength observations, to be used in concert with the existing far-UV measurements. For example, one would like to determine the distribution of rest-frame optical luminosities, and the star-formation histories, ages, dust content, and stellar masses— all necessary for understanding the range of objects selected with the typical Lyman Break photometric criteria, and the relationship of these objects to galaxies in the lower redshift universe. Indeed, different models provide quite divergent descriptions of the nature and fate of the objects which are identified as LBGs. According to one model, the galaxies selected as LBGs are bright in the rest-frame UV because they are experiencing merger-induced starburst events. The intense starburst events occur on relatively short timescales (less than 100 Myr), and produce 10-100 times less stellar mass than what is seen in a typical L^* galaxy. Such low-mass bursting objects would then be the precursors of local low-mass spheroids, unless they merge with similar objects to form more massive systems (Lowenthal *et al.* 1997; Sawicki & Yee 1998; Somerville, Primack, & Faber 2001). Alternatively, LBGs are the central objects in relatively massive dark matter halos, which form stars steadily but relatively quiescently over longer than 1 Gyr timescales, accumulate $\geq 10^{10} M_{\odot}$ by $z \sim 3$, and evolve eventually into the ellipticals and spiral galaxies at the bright end of the local luminosity function (Steidel *et al.* 1996a; Baugh *et al.* 1998).

It is not possible to determine the nature of LBG stellar populations— and thereby distinguish between the above scenarios— with only optical observations probing the rest-frame UV. Both an aging stellar population and increasing dust extinction result in redder rest-frame UV colors, so that the effects of age and dust are degenerate without longer wavelength data. Recent studies (Sawicki & Yee 1998; Dickinson 2000; Papovich, Dickinson, & Ferguson 2001) have shown that the addition of near-IR photometric measurements at rest wavelengths longer than the location of an age-sensitive spectral break at ~ 3600 Å removes some of the degeneracy between dust and age in the modeling of LBG stellar populations. Here we present the results of a moderately large near-IR survey of optically selected LBGs, designed to determine the distribution of rest-frame optical luminosities of LBGs, and, where possible, information about their star-formation histories. In §2, we present the details of the optical and near-IR observations and data reduction. §3 summarizes the distribution of optical-IR colors of LBGs. In §4, we describe the derivation of the LBG rest-frame optical luminosity function, and compare it to local galaxy luminosity functions. §5 presents the procedure and results of population synthesis modeling of the LBG spectral energy distributions between 900 Å and 5500 Å in the rest-frame, using the measured optical/IR colors. Extensions of the model results to rest-frame UV spectroscopy are discussed in §6, and an evolutionary sequence for LBGs is proposed in §7. Our general conclusions are summarized in §8.

2. OBSERVATIONS AND DATA REDUCTIONS

2.1. Optical Imaging

Optical images were obtained for all the fields included here as part of our extensive survey for $z \sim 3$ galaxies; the field centers are given in Table 1. The optical imaging data were collected during the interval 1995 - 1998 at the William Herschel Telescope (3C 324, B2 0902+34, and CDFa), the Palomar 200 inch Hale Telescope (CDFa, DSF2237a, DSF2237b, HDF, Q0201, Q0256, SSA22a, and SSA22b), and the Kitt Peak Mayall 4 meter Telescope (Westphal). The details of our survey have been presented elsewhere (Steidel *et al.* 1996a, Giavalisco *et al.* 1998, Steidel *et al.* 1999), so here we present only a summary of its relevant features. In deep U_n, G, $\mathcal{R}$ (Steidel & Hamilton 1993) images, with typical 1σ surface brightness limits of 29.1, 29.2, 28.6 AB magnitudes per arcsec^2, respectively, we identify $z \sim 3$ galaxy candidates by their distinctive colors. To select the objects in the sample centered at $z \sim 3$, the photometric criteria consist of the following:

$$\mathcal{R} \leq 25.5, \quad G - \mathcal{R} \leq 1.2, \quad U_n - G \geq G - \mathcal{R} + 1$$

These criteria effectively isolate star-forming galaxies whose redshifts place the Lyman continuum discontinuity within the U_n band, and result in a redshift distribution that is reasonably well-described by a Gaussian with $\langle z \rangle = 2.97$ and a standard deviation of $\sigma(z) = 0.27$. The various biases inherent in such photometric selection have been discussed extensively by Steidel *et al.* (1999). At the time of this writing, there are approximately 1000 LBGs in this redshift range that have been spectroscopically confirmed using the Low Resolution Imaging Spectrometer (LRIS; Oke *et al.* 1995) at the W. M. Keck Observatory. The full optical survey and spectroscopic catalogs will be presented elsewhere.

2.2. Near-IR Imaging

To explore the range of optical/near-IR colors present in our sample of high redshift galaxy candidates and spectroscopically confirmed $z > 2$ galaxies, a subset of objects was selected for follow-up near-IR imaging. Objects bright in $\mathcal{R}$ were preferentially selected for near-IR imaging, as can be seen by the relative distributions of $\mathcal{R}$ apparent magnitude in the near-IR sample and that in our $z \sim 3$ sample as a whole (Figure 1a). We deliberately selected objects whose rest-UV-inferred extinction properties (see Steidel *et al.* 1999 and AS2000 for a discussion) spanned the entire range seen in the full LBG survey, from zero to several magnitudes of extinction in the rest-frame UV. Within the LBG $z \sim 3$ selection function, galaxies with higher redshifts suffer greater absorption by intergalactic H I, resulting in systematically redder $G - \mathcal{R}$ colors for a fixed intrinsic spectral energy distribution (SED). Figure 1b shows the distributions of $(G - \mathcal{R})_0$, the $G - \mathcal{R}$ color statistically corrected for IGM absorption, for both the NIRC LBG sample and the LBG $z \sim 3$ sample as a whole. This figure shows that, in an effort to target galaxies with extreme

values of implied extinction with NIRC, we over-sampled the reddest $(G-\mathcal{R})_0$ bins by roughly a factor of 2 relative to the rest of the distribution.

All of the near-IR data were obtained with the facility near-IR camera (NIRC) (Matthews & Soifer 1994) on the W.M. Keck I Telescope during the course of 9 separate observing runs in the interval 1997 May - 1999 May. NIRC has a 256×256 InSb array, with a pixel scale of $0.15''$/pixel, resulting in a $38.4''$ field. This field size represents less than 1% of the large optical pointings used to find LBGs (typically $9'$ by $9'$) which contain 100-150 $z \sim 3$ candidates to $\mathcal{R} = 25.5$. To maximize efficiency, we preferentially targeted objects having at least one other LBG within $\sim 40''$. A typical pointing included 2–3 LBGs, but this number varied from 1 to 7 LBGs per pointing. Each NIRC pointing contained at least one primary target galaxy with a spectroscopic redshift, and, in many cases, additional LBG candidates for which spectra have not yet been obtained. There are spectroscopic redshifts for about 75% of the full $\mathcal{R} - K_s$ sample.

We observed at 1.25μm and 2.15μm, using the standard J and K_s filters. Using integration times of 4×15 seconds (J) and 6×10 seconds (K_s) per exposure, we dithered the telescope between exposures to form a 9-point box pattern on the sky, each box position separated by a few arcseconds. In most cases, we aimed to complete 6 or more sets of the 9-point dither pattern for each NIRC pointing. During the dither pattern the telescope was guided with an off-set CCD camera, with the orientation of the NIRC detector chosen so that a suitable guide star would fall on the guider chip. Table 1 summarizes the coverage of the NIRC survey with respect that of the optical survey for LBGs, listing the angular area and number of LBGs covered in K_s and J for each optical survey field. The optical fields listed in Table 1 do not represent the entire optical LBG survey, but only the fields which contain NIRC pointings. Table 2 summarizes all of the NIRC target pointings, the objects contained in each pointing, and the total integration times for each pointing.

The data were reduced using standard procedures with the aid of the DIMSUM[3] package. On clear nights, we determined the photometric zeropoints for the J and K_s bandpasses with observations of faint (11th - 12th magnitude) near-infrared standard stars from the list of Persson *et al.* (1998). During 5 of our 9 NIRC runs, we experienced stable, photometric conditions, while the remaining 4 runs contained variable cirrus. On runs with variable conditions, we carefully calibrated observing sequences with observations obtained when the conditions were judged to be photometric. As measured from the FWHM of standard stars, the seeing during our several NIRC runs ranged from $0.3''$ to $0.7''$ in both J and K_s, with FWHM$\simeq 0.5''$ being typical. Figure 2 shows two different examples of $\mathcal{R}$ and K_s images of LBGs surveyed with NIRC. Westphal-MMD11 has the reddest $\mathcal{R} - K_s$ color and brightest K_s magnitude in the NIRC LBG sample, while B20902-C6 is in the bluer and fainter half of the NIRC LBG sample.

[3]Deep Infrared Mosaicing Software, a package of IRAF scripts by Eisenhardt, Dickinson, Stanford, and Ward, available at ftp://iraf.noao.edu/contrib/dimsumV2/

2.3. Optical/Near-IR Photometry

Prior to the measurement of optical/near-IR colors, each NIRC frame was smoothed with a Gaussian to match the image quality in the corresponding optical images, which generally had $FWHM \simeq 1.0''$. The photometry was then performed in a manner analogous to that used for $z \sim 3$ galaxy searches, described elsewhere (Steidel *et al.* 1995; Steidel & Hamilton 1993). In brief, using a modified version of the FOCAS (Valdes 1982) image detection and analysis routines, a catalog of isophotal and "total" object detections was generated in the $\mathcal{R}-$band (where "total" refers to the FOCAS definition, which is the flux measured within an aperture grown to twice the area of the initial detection isophote). The $\mathcal{R}-$band isophotal detection apertures were applied to the J and K_s images, to measure $\mathcal{R}-J$ and $\mathcal{R}-K_s$ colors. Table 3 lists the $\mathcal{R}$ *total* magnitudes, $G-\mathcal{R}$, $\mathcal{R}-J$, $\mathcal{R}-K_s$ *isophotal* colors, and redshifts for all objects in the NIRC sample. Optical magnitudes (G and $\mathcal{R}$) and colors are referenced to the AB system, whereas the near-IR magnitudes (J, and K_s) are on the Vega system. [4]

2.4. Photometric Uncertainties

To quantify the uncertainties in the measured $\mathcal{R}-J$ and $\mathcal{R}-K_s$ colors, we ran Monte Carlo simulations mimicking the actual process used to measure magnitudes and colors from the real data. Artificial galaxies, with a reasonable range of intrinsic sizes and with $\mathcal{R}$ magnitudes and $\mathcal{R}-K_s$ colors drawn randomly from the observed range of both quantities, were added to the images after convolution with the seeing disk. We then produced detection catalogs in $\mathcal{R}$ and measured the $\mathcal{R}-K_s$ colors with matched apertures in the K_s image. The process of adding fake galaxy sets (the number of galaxies added in a given trial was kept small enough so as not to alter the systematics of the observed data frames) and recovering the magnitudes and colors using the same procedures used for the real data was repeated until enough detections were obtained to study the scatter between true and recovered $\mathcal{R}-K_s$ color as a function of recovered $\mathcal{R}$ and $\mathcal{R}-K_s$. The Monte-Carlo generated photometric uncertainties are significantly larger than those that would result from the application of simple Poisson counting statistics that neglect systematics.

The detections of artificial objects were binned in 0.5 mag steps in measured $\mathcal{R}$ magnitude and 0.2 mag steps in measured $\mathcal{R}-K_s$ color. The mean and standard deviation were then computed for the distribution of $\Delta(\mathcal{R}-K_s) = (\mathcal{R}-K_s)_{true} - (\mathcal{R}-K_s)_{measured}$ in each $(\mathcal{R}, \mathcal{R}-K_s)$ bin. In general we did not find a significant systematic offset between the measured and true colors, so the color uncertainties are treated as symmetric. Accordingly, we adopted the standard deviation

[4]To convert from Vega magnitudes to AB magnitudes, we adopt the transformations: $K_s(AB) = K_s(Vega) + 1.82$, $J(AB) = J(Vega) + 0.90$. The standard relation between AB magnitude and flux-density, f_ν, is: $m_{AB} = -48.6 - 2.5 \log f_\nu$ where f_ν is in units of ergs s^{-1} cm^{-2} Hz^{-1}.

of the $\Delta(\mathcal{R}-K_s)$ distribution as the 1σ color uncertainty, $\sigma(\mathcal{R}-K_s)$ for each $(\mathcal{R},\mathcal{R}-K_s)$ bin.

To be conservative, we initially treated each NIRC pointing independently for the estimation of photometric uncertainties in order to explore possible variations due to slightly different depths, seeing conditions, and sky background. We subsequently determined that the trend of $\sigma(\mathcal{R}-K_s)$ with $(\mathcal{R},\mathcal{R}-K_s)$ was similar enough in all K_s NIRC pointings that we simply combined the simulation results from all pointings to calculate an average trend of $\sigma(\mathcal{R}-K_s)$ with $(\mathcal{R},\mathcal{R}-K_s)$ for our entire $\mathcal{R}-K_s$ sample. Uncertainties were then assigned to the measured $\mathcal{R}-K_s$ colors in the NIRC sample, based on the magnitude and color of each object.

An identical procedure was used to generate uncertainties in the $\mathcal{R}-J$ colors of all of the observed galaxies. The $G-\mathcal{R}$ uncertainties were computed from a separate, but similar, set of Monte Carlo simulations (Adelberger 2001). All the color uncertainties are listed along with the optical/IR photometry in Table 3.

3. THE OPTICAL/IR COLORS OF LYMAN BREAK GALAXIES

The distribution of measured optical-IR colors for the 118 galaxies with NIRC K_s data is shown in Figure 3. 107 of these measurements are K_s detections significant at the 5σ level, while 11 of them are only upper-limits, whose $\mathcal{R}-K_s$ limits correspond to the typical 5σ detection limit of $K_s = 22.5$ in our images. We find a mean $\mathcal{R}-K_s$ color of $<\mathcal{R}-K_s>=2.85$ and a standard deviation $\sigma(\mathcal{R}-K_s)=0.59$. Of these 118 galaxies, 81 have measured redshifts, with a mean of $<z>=2.996$. There are J band measurements for 63 of the galaxies in the $\mathcal{R}-K_s$ sample. The mean $J-K_s$ color is $<J-K_s>=1.52$ with $\sigma(J-K_s)=0.77$. At $z\sim 3$, the J and K_s filters correspond to $\lambda_{eff}(J)=3100$Å, and $\lambda_{eff}(K_s)=5400$Å in the rest-frame, respectively, whereas the optical passbands U_n, G, and $\mathcal{R}$ sample the galaxies at rest-frame $\lambda_{eff}\simeq 900$, 1200, and 1700 Å, respectively.

Clearly, there is a wide range of optical/near-IR color among the rest-UV selected $z\sim 3$ LBGs; the bluest galaxies in $\mathcal{R}-K_s$ have colors that are essentially flat in f_ν units from the far-UV to the optical in the rest-frame, whereas the reddest LBGs approach the colors of "extremely red objects". The typical $\mathcal{R}-K_s$ color of $z\sim 3$ LBGs is more than 2.5 magnitudes redder than that expected for an unreddened instantaneous burst of star-formation at the mean redshift of our sample ($\mathcal{R}-K_s=0.30$), but is significantly bluer than most galaxies in the present-day universe (cf. Papovich *et al.* 2001). Unfortunately, in the absence of high quality spectra covering the same large wavelength range, the interpretation of the colors of LBGs in the context of understanding their stellar populations and extinction must rely heavily on models. In §5, we use the full set of optical-IR colors ($G-\mathcal{R}, \mathcal{R}-J$, and $\mathcal{R}-K_s$) of LBGs in the NIRC sample in an attempt to disentangle the degenerate effects of dust and age on LBG broadband spectral energy distributions.

4. REST-FRAME OPTICAL LUMINOSITY FUNCTION

The distribution of redshifts and observed $\mathcal{R}$ and I magnitudes have been used to construct rest-frame far-UV luminosity functions for LBGs at $z \sim 3$ and $z \sim 4$ respectively (Steidel *et al.* 1999). With near-IR K_s magnitudes and optical-IR $\mathcal{R} - K_s$ colors for a sample of 118 LBGs, we have the necessary information to construct the rest-frame *optical* luminosity function of $z \sim 3$ LBGs, which is much more easily compared with galaxies in the present-day universe. Optical emission is much less attenuated than far-UV light by the presence of dust, and expected to be less directly linked to the instantaneous star-formation rate, as the stars giving rise to the optical emission sample a larger swath of the main sequence and include stars with longer lifetimes than the O/B stars producing the far-UV light. Thus, one might hope that the optical luminosities provide more information on the integrated stellar populations of the LBGs than can be obtained from far-UV measurements.

At $z \simeq 3$, the mean redshift of the LBG spectroscopic sample (and of the NIRC sample as well), the K_s-band central wavelength of 2.15μm is quite a good match to the central wavelength of the standard V optical filter. While the NIRC sample contains galaxies with a range of redshifts, the K_s-band central wavelength falls within the rest-wavelength range $5100 - 5700$Å for the bulk of the sample. Furthermore, the "photometric depth" of the LBG redshift selection function corresponds to a difference in absolute magnitude of only $\Delta M_V \sim 0.30$ magnitudes for a given apparent magnitude; consequently, given our typical measurement uncertainties, we view it as a reasonable approximation for this analysis to treat all the galaxies in the NIRC sample as if they were located at the mean redshift of the entire LBG spectroscopic sample. This of course allows us to use the whole NIRC sample, and not just the objects with spectroscopic redshifts, for the luminosity function analysis.

Two pieces of information are required to construct the rest-frame optical luminosity function for LBGs at $z \sim 3$: the LBG rest-frame UV luminosity function (i.e. the distribution of $\mathcal{R}$ apparent magnitudes), and the LBG distribution of $\mathcal{R} - K_s$ as a function of $\mathcal{R}$ magnitude for the NIRC sample. The best-fit $\mathcal{R}$ apparent magnitude luminosity function parameters for LBGs (uncorrected for the effects of dust extinction) are a faint-end slope of $\alpha = -1.57$, a characteristic apparent magnitude of $m^*_{\mathcal{R}} = 24.54$, and an overall normalization of $\phi^* = 4.4 \times 10^{-3} h^3 \mathrm{Mpc}^{-3}$ (AS2000).[5] In §3, we presented the overall distribution of $\mathcal{R} - K_s$ colors for the NIRC sample. A correlation with 98% confidence (better than 2σ) is detected between $\mathcal{R} - K_s$ color and $\mathcal{R}$ magnitude, such that fainter galaxies have redder $\mathcal{R} - K_s$ colors (see Figure 4). This correlation probability was computed including the 11 upper limits in the sample of 118 galaxies with $\mathcal{R} - K_s$ measurements, so the result should not be biased by our typical detection limit of $K_s = 22.5$. The trend of $\mathcal{R} - K_s$ with $\mathcal{R}$ is included in the luminosity function analysis by using the relationship implied by the best-fit regression slope to the correlation: $\frac{d\langle \mathcal{R} - K_s \rangle}{d\mathcal{R}} = 0.17$. There is a lot of scatter

[5]These parameters were fit assuming the currently favored cosmology of $\Omega_m = 0.3, \Omega_\Lambda = 0.7$.

around this regression slope, but it provides a means of encoding the trend between the two variables.

We generated a large sample (15000) of LBG $\mathcal{R}$ apparent magnitudes between $\mathcal{R} = 22.5$ and $\mathcal{R} = 27$, by randomly drawing luminosities from the LBG $z \sim 3$ rest-frame UV luminosity function placed at z=2.972, the mean redshift of the current $z \sim 3$ LBG spectroscopic sample. An $\mathcal{R} - K_s$ color was then assigned to each of the $\mathcal{R}$ magnitudes, drawn randomly from the distribution of $\mathcal{R} - K_s$ colors for galaxies in the NIRC sample with $24 \leq \mathcal{R} \leq 24.5$, and then shifted by the amount, $\Delta(\mathcal{R} - K_s) = 0.17 \times (\mathcal{R} - 24.25)$, according to the correlation between $\mathcal{R}$ and $\mathcal{R} - K_s$. The fiducial $(\mathcal{R}, \mathcal{R} - K_s)$ distribution was restricted to $\mathcal{R} = 24.0 - 24.5$ because this 0.5 magnitude range contained the largest number of $\mathcal{R} - K_s$ measurements (36). Also, the $\mathcal{R} - K_s$ measurements for $\mathcal{R} = 24.0 - 24.5$ were virtually all detections, rather than mixture of upper limits and detections. Combining each randomly generated pair of $\mathcal{R}$ and $\mathcal{R} - K_s$ measurements, we obtained an ensemble of K_s magnitudes, which were grouped into 0.5 magnitude bins.

To determine how the photometric uncertainties of both the $\mathcal{R}$ magnitudes and $\mathcal{R} - K_s$ colors translated into uncertainties in the derived K_s luminosity function, the procedure of generating an ensemble of random ($\mathcal{R}$, $\mathcal{R} - K_s$) pairs was repeated a large number (10000) of times. In each trial, we perturbed the sample of actual ($\mathcal{R}$, $\mathcal{R} - K_s$) measurements by random amounts consistent with the photometric uncertainties. In so doing, we assumed that the errors in $\mathcal{R}$ and $\mathcal{R} - K_s$ were uncorrelated, which is a valid approximation since the error in $\mathcal{R} - K_s$ for galaxies in our sample is dominated by the K_s photometric error. Due to the slight differences in the sample of $\mathcal{R}$ magnitudes drawn from the LBG $\mathcal{R}$ apparent luminosity function, and the more significant differences of the perturbed ($\mathcal{R}$, $\mathcal{R} - K_s$) measurements, a different K_s distribution was produced in each trial. The analytic Schechter function (1976) was fit to each perturbed distribution of K_s-band apparent magnitudes. We restricted the fitted region to span only $19 \leq K_s \leq 22.5$, reflecting the K_s range for which we have actual measurements. The average number from all the trials was adopted for each 0.5 K_s magnitude bin, and the adopted 1σ uncertainty was the standard deviation among the realizations (which does not include the uncertainties in the LBG $\mathcal{R}$-band luminosity function best-fit parameters (AS2000)).

The Schechter function was then fit to the average luminosity function values. The best-fit parameters we obtain are an overall normalization of $\phi^* = 1.8 \pm 0.8 \times 10^{-3}\ h^3\mathrm{Mpc}^{-3}$, a faint end slope of $\alpha = -1.85 \pm 0.15$, and a characteristic apparent magnitude of $m^*_{K_s} = 20.70 \pm 0.25$. The uncertainties on the fitted parameters represent the confidence intervals generated by fitting the Schechter function to each perturbed K_s distribution. Since it was assumed that all the galaxies comprising the K_s luminosity function were at the mean redshift of the LBG spectroscopic sample, it is straightforward to convert the distribution of K_s apparent magnitudes into a 5400Å (i.e. rest-frame V-band) absolute magnitude distribution. With our adopted $\Omega_m = 0.3, \Omega_\Lambda = 0.7$ cosmology, $m^*_{K_s} = 20.70$ corresponds to $M^*_V = -22.21 + 5 \log h$. The overall shape of the rest-frame optical luminosity function is determined by the way in which the $\mathcal{R} - K_s$ distribution as a function of $\mathcal{R}$ magnitude redistributes $\mathcal{R}$ magnitudes into K_s magnitudes. Accordingly, the

faint end slope of the LBG rest-frame optical luminosity function is steeper than that of the UV luminosity function, due to the positive correlation between $\mathcal{R}$ and $\mathcal{R} - K_s$. Figure 5 shows the apparent K_s luminosity function (and the absolute optical magnitudes to which it corresponds), as well as the confidence intervals on the best-fit Schechter luminosity function parameters. Immediately apparent from Figure 5 is the fact that the well-constrained bright end of the LBG luminosity function greatly exceeds locally determined optical luminosity functions.

To calculate the rest-frame optical co-moving luminosity density for LBGs brighter than $K_s = 22.5$, we integrate over the luminosity-weighted luminosity function in the appropriate magnitude range to obtain $\rho_{5400\mathring{A}} = 6.86 \times 10^{26}\,\mathrm{erg\,s^{-1}Hz^{-1}}h\,\mathrm{Mpc^{-3}}$. We use the V-band absolute magnitude of the Sun, $M_{V\odot} = 4.83$ (Binney & Merrifield 1998), to express this quantity in solar units: $\rho_V = 1.35 \times 10^8\, L_\odot h\,\mathrm{Mpc^{-3}}$. If the luminosity function were integrated to $K_s = 25.0$, the derived luminosity density would be more than 2 times larger than the value determined down to the typical survey detection limit of $K_s = 22.5$. However, such an extrapolation depends sensitively on the value of the faint end slope of the luminosity function, which is poorly constrained by our observed sample. Fukugita *et al.* 1998 summarize recent local determinations of the B-band luminosity density, most of which are in the range $\rho_B = 1.8 - 2.2 \times 10^8 L_\odot\,\mathrm{Mpc^{-3}}$. Thus, the LBG V-band optical luminosity density down to only $K_s = 22.5$ is within a factor of 2 of local measurements of the B-band optical luminosity density, which were obtained by integrating over the entire B-band luminosity function.

The optical luminosity function of local galaxies has been computed from numerous surveys over the past thirty years. Some recent determinations from magnitude limited redshift surveys include the Two-Degree Field Galaxy Redshift Survey (2dFGRS) b_j luminosity function (Folkes *et al.* 1999), the Las Campanas Redshift Survey (LCRS) R-band luminosity function (Lin *et al.* 1996), and the Sloan Digital Sky Survey (SDSS) luminosity functions in five optical bands (Blanton *et al.* 2001). These local optical luminosity functions have much shallower faint end slopes (α), fainter characteristic luminosities (M_*), and higher overall normalizations (ϕ^*) than the rest-frame optical luminosity function of LBGs. To demonstrate these differences, we plot the 2dFGRS b_j luminosity function in Figure 5 along with the LBG rest-frame optical luminosity function. The best-fit parameters of the 2dFGRS luminosity function are $\phi^* = 1.69 \pm 0.17 \times 10^{-2}\ h^3\mathrm{Mpc^{-3}}$, $\alpha = -1.28 \pm 0.05$, and $M^* = -19.73 \pm 0.06 + 5\log h$. For a direct comparison with the LBG luminosity function, which specifically probes the rest-frame V band, the 2dFGRS luminosity function has been shifted 0.5 magnitudes brighter (i.e. $M^* = -20.23 + 5\log h$), reflecting the typical $b_j - V$ color of local galaxies.

At the brightest absolute magnitudes, where the LBG V-band luminosity function is well-constrained by our observations, the $z \sim 3$ LBG V-band luminosity function greatly exceeds the local function, and has a different shape. For this reason, we caution against over-interpreting the differences in the best-fit Schechter function parameters relative to other luminosity functions; for example, the very steep faint end slope, very bright value of M^*, and relatively low value of ϕ^* may well result from fitting the function over a small range of luminosity that does not actually

extend as faint as the true "knee" in the luminosity distribution. In practice, it will be extremely difficult to extend this distribution to much fainter near-IR magnitudes from the ground, but it should be quite possible from space.

The obvious implication of the bright end of the V-band luminosity function of LBGs is that the mass-to-light ratio M/L_V of LBGs must be very different from that of galaxies in the local universe. Since the co-moving optical luminosity density in the $z \sim 3$ universe is evidently as large or larger than that in the $z \sim 0$ universe despite the fact that most of the stars observed in the local universe probably formed after $z \sim 3$, the V band light at $z \sim 3$ is apparently dominated by relatively massive stars associated with greatly enhanced current star-formation rates, and carries little information about total stellar mass. Unfortunately, this also means that no observations from the ground are likely to act as a direct proxy for stellar mass in objects that are actively forming stars at high redshift. Indeed, these observations, at 2.15 μm, are still dominated by the light from ongoing star-formation. In any case, *the V-band luminosity density of LBGs at $z \sim 3$ probably exceeds that of all stars in the present-day universe.*

5. THE STELLAR POPULATIONS OF LYMAN BREAK GALAXIES

Given photometry that extends from $\sim 900 - 5500$ Å in the rest-frame for a reasonably large sample of $z \sim 3$ LBGs, it is of interest to use the data to constrain the star-formation histories and extinction properties of the galaxies with reference to models. Because the galaxy luminosity at even the longest wavelengths observed in our sample is still dominated by stars with small mass-to-light ratios, it is impossible to constrain the integrated stellar mass of galaxies without understanding something about the star-formation history. As it turns out, our sensitivity to the star-formation history using optical and near-IR data is coarse, at best— at the corresponding rest-frame far-UV to optical wavelengths, active star-formation can easily mask the evidence for previous generations of stars (see, e.g., Papovich *et al.* 2001), and dust extinction has a significant effect on the emergent SED. In order to interpret the color information of the LBGs in terms of interesting constraints on physical parameters, we must rely on models of both dust extinction *and* the intrinsic spectral energy distributions of stellar populations as a function of metallicity, initial mass function (IMF), star-formation history, and age. There is a large range of possible parameterizations of the extinction law and the intrinsic stellar population, and in general these cannot be well-constrained independently from fits to the galaxy SEDs. Consequently, in what follows, we adopt simple models for the attenuation law, and for the metallicity, IMF, and star-formation history of the stellar population, which external observations have shown to be reasonable for star-forming galaxies in the nearby and high redshift universe. Where relevant, we point out where different assumptions yield significantly different results. Extensive grids of models have been fitted to (generally fainter) LBGs observed in the HDF-North by Papovich *et al.* 2001; we refer the reader to that paper for a more detailed discussion of the effects of varying the modeling assumptions.

5.1. Age-Dust Degeneracy

With only optical (U_n, G, $\mathcal{R}$, and I) photometry for $z \sim 3$ galaxies, it is not possible to distinguish between a young galaxy spectral energy distribution (≤ 30 Myr) which is considerably reddened by dust, and the spectral energy distribution of a galaxy which has been continuously forming stars over a much longer time scale (~ 1 Gyr), but with much less dust extinction (Sawicki & Yee 1998). Figure 6 shows the results of fitting only the $G - \mathcal{R}$ color of the galaxy 3C324-C2 with Bruzual & Charlot (1996) constant star-formation galaxy spectral templates of different ages. As the template age increases, the amount of dust reddening necessary to fit the observed $G - \mathcal{R}$ color decreases. Both the 1 Myr model with $A_{1600} = 2.84$ and the 1 Gyr model with $A_{1600} = 1.61$ fit the observed optical photometry equally well (where A_{1600} is magnitudes of extinction at 1600Å rest-frame). Indeed, the model rest-frame UV slope can be modified to match the observed (U_n, G, $\mathcal{R}$, I) colors, by simultaneously tuning its age and dust-content. The degeneracy results from the fact that, at $z \sim 3$, commonly used optical filters probe a short-wavelength region of the rest-frame spectrum which does not contain any age-sensitive features that can be easily recognized from broad-band photometry. However, there is an age-sensitive break in the spectral energy distributions of actively star-forming galaxies that occurs near 3648Å, often referred to as the "Balmer break". The Balmer break feature, which is is age sensitive over star-formation timescales of ~ 50 Myr-1 Gyr, cannot be described equally well by any combination of stellar population aging and dust-content. Longer wavelength photometry which includes the discontinuity can in principle be used to break the degeneracy between model fits.

The Balmer break feature in galaxy spectra is due to the stellar bound-free absorption coefficient, which has a sharp edge at 3648Å, (the wavelength of the $n = 2 \longrightarrow$ *continuum* transition in neutral hydrogen), causing photons with wavelengths shortward of the edge to be absorbed much more efficiently than those with longer wavelengths. The prominence of this feature in a stellar spectrum depends on the temperature and gravity of the stellar atmosphere, which determines the form of hydrogen that is prevalent in the stellar atmosphere, and therefore which component of the total stellar absorption coefficient is dominant. In cooler late-type stars (such as F, G, and K), H^- opacity dominates the total absorption coefficient, and the Balmer decrement is not very pronounced. In the early-type massive O and B stars the high temperatures result in the increased ionization of hydrogen, so again, the Balmer absorption coefficient is reduced. The Balmer break is most prominent in A-stars with temperatures around $10,000^\circ$K (Gray 1976).

At the onset of star-formation, a galaxy spectrum is dominated in the rest-frame UV and blue by the most-massive (O and B) stars, most of which have lifetimes shorter than 10 Myr. In a continuous star-formation model, after roughly 10 Myr, the rate at which O stars are being formed balances the rate at which they are dying, and the number of O stars levels off to a constant value (Leitherer *et al.* 1999). Meanwhile, the lifetimes of less massive A stars range from several hundred Myr to 1 Gyr. Therefore, as the O star population levels off, the number of A stars continues to increase. At the age where the increasing number of A stars relative to the constant number of O stars causes the galaxy spectrum at ~ 3600Å to be dominated by an A-star spectrum, we start to

see an increasing Balmer break in the galaxy spectrum. After 100 Myr the magnitude difference on either side of the Balmer break in an unreddened galaxy model is 0.3 mag, and by 1 Gyr, the break has increased to a 0.6 magnitudes.

Thus, the strength of the Balmer break can be used as a rough guide to the duration of the current episode of star-formation on timescales $\lesssim 1$ Gyr. The details will depend on the star-formation history (e.g., whether the star-formation rate (SFR) is an increasing, or declining, function of time), the shape of the initial mass function, and the metallicity of the stellar population. Because the Balmer break even at its strongest is a relatively subtle spectral feature, and because only broad-band photometry is available for the galaxies, a measurement of the Balmer break strength requires removing the effects of continuum reddening. This requirement introduces some covariance into the simultaneous estimates of extinction and the age of the star-formation episode; we discuss this covariance extensively in §5.3.2.

5.2. Population Synthesis Modeling

5.2.1. Spectroscopic Sample

In order to examine the range of stellar population properties present in the NIRC sample of LBGs, we considered only the subsample of galaxies with measured redshifts and near-IR detections at least in K_s. The spectroscopic sample so defined consists of 81 galaxies. We included the $G-\mathcal{R}$, $\mathcal{R}-J$, and $\mathcal{R}-K_s$ colors of these galaxies in the modeling; the U_n band is strongly affected by H I absorption in both the galaxy and the IGM. A substantial fraction of the spectroscopic sample also has available I band photometry, but for these high redshift objects the I band adds little information because of its proximity to $\mathcal{R}$ and because the measurements are generally noisier than in other bands. Nevertheless, U_n and I data points (when they exist) are included in figures indicating the best-fit spectral template with respect to the observed LBG photometry,

The model galaxy templates used to fit the LBG photometry include no Lyman α emission, and typically contain Lyman α absorption with observed equivalent widths of $40-60$Å ($10-15$Å in the rest-frame). However, the sample of LBGs for which there are rest-frame UV spectra exhibit a wide range of Lyman α equivalent widths, some of which are ten times larger than the model line widths, and appear in either absorption, emission, or a combination of both. The *observed* Lyman α equivalent width was used to correct the $G-\mathcal{R}$ color for line emission for each of the 81 galaxies in the spectroscopic sample. Figure 7 displays the distribution of Lyman α observed equivalent widths for the LBGs with both NIRC data and Keck LRIS spectra (cf. Steidel *et al.* 2000).

Nebular line emission redshifted into the K_s-band might also bias the results of population synthesis modeling. The [OIII] $\lambda 5007, 4959$ Å doublet and Hβ $\lambda 4861$ Å line all fall within the K_s-band window for $z \geq 3.094$. In the NIRC LBG spectroscopic sample, 49 out of 81 galaxies

(60%) have $z \geq 2.974$ such that at least [OIII] λ5007 Å, the strongest of the three lines, is located within the K_s-band. Nebular line strengths have been measured for only a small sample of LBGs at the current time (see Pettini *et al.* 2001), nine of which are in the NIRC sample. The combined equivalent width from all the nebular lines affecting the K_s magnitude was calculated by comparing the line fluxes from Pettini *et al.* 2001 to the continuum flux, measured with NIRC. For each galaxy, the total nebular equivalent width in the K_s filter was compared to the effective width of the K_s filter, $\Delta\lambda(K_s)_{eff} = 3300$Å, to evaluate the necessary correction to the K_s magnitude and $\mathcal{R} - K_s$ color. In every case, the indicated corrections for nebular emission reduce the K_s continuum flux, resulting in a bluer $\mathcal{R} - K_s$ color. The $\mathcal{R} - K_s$ corrections ranged from $0.03 - 0.27$ magnitudes with a median $\Delta(\mathcal{R} - K_s) = 0.14$ mag.

In order to determine the effect of these $\mathcal{R} - K_s$ color corrections on best-fit model parameters, we fit Bruzual & Charlot (1996) constant star-formation models to the colors of the nine galaxies with measured nebular equivalent widths. Models were fit to both the uncorrected colors and the colors corrected for nebular line emission. The $\mathcal{R} - K_s$ correction resulted in little or no change to the best-fit $E(B-V)$ value (since most of the lever arm for extinction estimation comes from the rest-UV data). The effect on the best-fit age was more significant, in that the nebular line correction will result in a systematically younger inferred age. The median correction for the nebular line contamination results in stellar population ages that are ∼35% younger than if no corrections for line emission are applied. It should be emphasized that nebular line contamination is negligible for the 40% of the spectroscopic NIRC sample with $z < 2.974$. With such a small sub-sample having near-IR spectroscopy at the time of this writing, there is not enough information available to determine how corrections for emission line contamination should be implemented for objects without near-IR spectroscopic measurements. We have chosen, therefore, not to apply these corrections, but to emphasize that in some cases the inferred ages may be influenced by the emission line contamination of the broad-band K_s measurements.

5.2.2. Modeling Procedure

The two main theoretical elements which we used were (1) model galaxy spectra generated with the Bruzual & Charlot 1996, (hereafter BC96) population synthesis code, and (2) a dust effective attenuation law empirically derived by Calzetti (1997) for local starbursts. [6] There are few constraints on the appropriate reddening model to use for high redshift star forming galaxies, and so we have adopted the form that works quite well for local starburst galaxies, which are arguably the best local analogs of LBGs. The validity of this reddening/extinction law

[6]The Calzetti attenuation law relates the observed flux, F_λ, in units of ergs s^{-1}Å^{-1}, to the intrinsic flux, $F_{0\lambda}$, with the relation: $F_\lambda = F_{0\lambda} 10^{-0.4E(B-V)k(\lambda)}$, where $k(\lambda)$ is a decreasing function of wavelength, reflecting the fact that shorter wavelengths suffer more extinction than longer wavelengths. The attenuation curve is parameterized by an overall normalization, $E(B-V)$.

at high redshift has yet to be tested adequately, due to the difficulty in measuring bolometric star-formation luminosities at high redshift (see Meurer *et al.* 1999; AS2000). We simply use it as the most realistic representation of the attenuation in in $z \sim 3$ LBGs; we will briefly discuss how the results depend on the assumed attenuation law in §3.2.

At the time this work began, the newest Bruzual and Charlot software available to us was the BC96 version, so that the results discussed in detail are based on BC96 model fits. In order to verify that the population synthesis fits did not change significantly with the most recent version of the Bruzual and Charlot package, BC2000 (Charlot 2000, private communication; Liu, Charlot, & Graham 2000), we compared the BC96 and BC2000 results for a subset of models. BC96 results were also compared with those from the Starburst99 models (Leitherer *et al.* 1999).

Models with both solar and sub-solar metallicity were fit to the observed colors of LBGs, but we discuss results for only solar metallicity models. Recent measurements of LBG metallicities are not very well constrained, ranging from $0.1 - 0.5 Z_{\odot}$ (Pettini *et al.* 2001), indicating that these galaxies are more metal-rich than Damped Lyman α systems at the same redshift, but have slightly lower metallicites than H II regions in the Milky Way near the Sun. Even so, we prefer to use solar metallicity stellar models, since they are the only models which have been directly calibrated against empirical stellar spectra of many spectral types. Specifically, in the grid of theoretical stellar spectra compiled by Lejeune, Buser, and Cuisinier (1996, 1997), which was used for the BC96 modeling, the only spectra which have been extensively tested against empirical stellar spectra are those with solar abundance. Papovich *et al.* 2001 report that the effects of using $0.2\ Z_{\odot}$ rather than solar metallicity models to fit LBG colors include best-fit ages systematically younger by a factor of 2, best-fit UV extinction factors systematically higher by a factor of 3, and derived stellar masses smaller by a factor of 2. These effects stem from the fact that the uncalibrated sub-solar metallicity models have intrinsically bluer UV continuum slopes and slightly larger Balmer breaks than solar metallicity models, for a given stellar population age. However, Leitherer *et al.* 2001 recently presented observations of O stars in the Large and Small Magellanic clouds with an average metallicity of $Z = \frac{1}{4} Z_{\odot}$, showing that metallicity does not have very drastic effects on the empirical rest-frame UV spectra of hot stars. Leitherer *et al.* concluded that modeling the spectra of $\sim \frac{1}{4} Z_{\odot}$ galaxies with solar metallicity models is an approximately valid approach. Until theoretical stellar libraries are updated with empirically calibrated sub-solar metallicity models of many spectral types, we believe that solar metallicity models are preferable.

For all of the BC96 models, a Salpeter IMF extending from $0.1 M_{\odot}$ to $125 M_{\odot}$ was assumed. Papovich *et al.* (2001) have investigated the effects of varying the IMF on the estimated stellar population parameters. Acceptable model fits are obtained for IMFs with various slopes and lower mass cutoffs, with slightly different results. For example, use of the steeper Scalo IMF results in younger ages, lower attenuation values, higher star-formation rates, and larger formed stellar masses. The effect of changing the IMF on the formed stellar mass is small, however, compared with the associated uncertainties. We choose not to include the form of the IMF as another parameter in our model, although clearly the shape of the IMF, if allowed to vary arbitrarily, can

have a very significant effect on the stellar population parameters.[7]

Evolutionary tracks distributed by the "Padova School" (the default for BC96) were used to describe the evolution of all the formed stars through the H-R diagram. Several different simple star-formation histories were considered: a continuous star-formation rate, $\Psi(t) = \Psi_0$; and exponentially declining star-formation rates, $\Psi(t) = \Psi_0 \exp(-t/\tau)$, with $\tau = 100, 50, 10$ Myr. The set of time constants, τ, was chosen to span the range between the two extremes of an instantaneous burst and continuous star-formation. For each star-formation history, two parameters were allowed to vary: 1) the *extinction*, parameterized by $E(B-V)$, and 2) the *age* since the onset of the most recent episode of star-formation, t_{sf}.

The model dust-attenuated, rest-frame galaxy spectra were shifted to the measured redshift of the actual galaxy, and further attenuated in a manner simulating absorption by the intergalactic medium of neutral hydrogen (Madau 1995). Each internally reddened, redshifted, IGM-absorbed galaxy spectrum was then integrated through the ($G, \mathcal{R}$, J, and K_s) filter transmission curves to calculate its predicted colors. For each $(E(B-V), t_{sf})$ combination, the predicted ($G-\mathcal{R}$, $\mathcal{R}-J$, and $\mathcal{R}-K_s$) colors were compared with the observed colors using the χ^2 statistic. The best-fit $(E(B-V), t_{sf})$ combination was chosen to minimize χ^2, and the intrinsic instantaneous star-formation rate was determined by normalizing the best-fit model to the observed $\mathcal{R}$ magnitude (taking into account the best-fit extinction). By our definition, the "formed stellar mass" m_{star} is simply the integral of the star-formation rate and the age of the star-formation episode obtained from the best-fit model.

Once the best-fit $E(B-V)$, t_{sf}, $\Psi(t_{sf})$, and m_{star}, were obtained for the galaxies in the spectroscopic sample, we computed the 68.3% and 90% confidence intervals associated with each parameter. For each galaxy we generated a large sample of fake "observed" colors, by perturbing the observed colors in a manner consistent with the photometric errors. We assumed the errors were Gaussian, based on the results of Monte Carlo simulations (§2.4). We also assumed that the color errors were uncorrelated, a valid assumption given that the near-IR uncertainties tend to be much larger than the $\mathcal{R}$ uncertainty. The large sample of fits to the perturbed colors indicated the region of $(E(B-V), t_{sf}, \Psi(t_{sf}), m_{star})$ parameter space allowed by each galaxy's observed colors and photometric uncertainties.

5.2.3. Comparison of Models

As described above, a range of BC96 star-formation histories was considered, and the differences between BC96, BC2000, and Starburst99 were investigated. For the purpose of this analysis, and given our relatively large photometric uncertainties, the BC96 and BC2000 model

[7]An analysis of the gravitationally-lensed LBG MS 1512-cB58 by Pettini *et al.* 2000 has shown that a Salpeter IMF is very successful in reproducing the details of the far-UV spectrum.

fits are virtually indistinguishable. For the solar metallicity constant star-formation models, the BC2000 model SEDs have slightly bluer rest-frame far-UV slopes and slightly larger Balmer breaks than the BC96 SEDs for a given star-formation history. Therefore, best-fit ages from BC2000 are typically 70% as old, while extinction values are larger ($\Delta E(B-V) \lesssim 0.06$). The BC2000 best-fit extinction-corrected star-formation rates $\Psi(t_{sf})$ are typically 25% larger than in the BC96 models, and so the BC2000 m_{star} is typically 85% of the BC96 m_{star}. These differences are insignificant, given the large confidence intervals allowed for the best-fit and derived parameters for any given set of models.

The differences between the BC96 and the Starburst99 constant star-formation models were also explored. The Starburst99 models use stellar evolutionary tracks from the "Geneva School", and the model atmosphere grid of Lejeune *et al.* 1997. For the sake of consistency, we chose solar metallicity Starburst99 templates with a Salpeter IMF, which we re-normalized by roughly a factor of 0.5 in luminosity, to remove the effects of the larger minimum mass cutoff in the Starburst99 Salpeter IMF ($1\ M_{\odot}$). As in the case of BC2000, the Starburst99 best-fit $E(B-V)$ and t_{sf} parameters tended towards younger ages (45% of the BC96 t_{sf}), and slightly larger values of $E(B-V)$, ($0 < \Delta E(B-V) \leq 0.07$). The higher $E(B-V)$ values in the Starburst99 fits lead to extinction-corrected $\Psi(t_{sf})$ values which are 65% larger than the BC96 values on average, and therefore the m_{star} values for the Starburst99 models were typically 70% of the BC96 m_{star} values. The differences between the BC96 and Starburst99 $E(B-V)$ and t_{sf} parameters are also small compared with the allowed confidence intervals.

For all three sets of models: BC96, BC2000, and Starburst99, the relative ordering of $E(B-V)$ and t_{sf} is preserved— galaxies best described by higher $E(B-V)$ [t_{sf}] galaxies in the BC96 models also have higher $E(B-V)$ [t_{sf}] according to the Starburst99 and BC2000 models. Finally, we note that for each galaxy in our sample, the BC96, BC2000, and Starburst99 constant star-formation models all provide statistically indistinguishable fits— i.e. there are no cases where one set of models has significantly lower χ^2 values than the others. Evidently, even for identical star-formation histories, there are significant differences in the predictions of each of the models that can amount to a factor of 2 in inferred age and a factor somewhat less than 2 in formed stellar mass. Thus, it would be a mistake to take the results from any of the models as anything but approximate until both the models and the data improve.

The model results for different BC96 star-formation histories were also compared in detail. We did not consider a very large number of star-formation histories, but enough to bracket a range of star-formation decay time (τ) parameter space. For the majority of the galaxies successfully modeled, *all* of the star-formation histories considered yielded best-fit models with χ^2 values allowed at the 90% level. For 8 of the galaxies we were able to rule out the models with time constants smaller than $\tau = 100$ Myr— this sub-sample is comprised of galaxies which are simultaneously blue in $G-\mathcal{R}$ and red in $\mathcal{R}-K_s$, and which have among the largest inferred continuous star-formation ages.

For the rest of the galaxies, whose star-formation histories cannot be usefully constrained, the best-fit $E(B-V)$ and, especially, t_{sf}, parameters demonstrate quite a large spread depending on which star-formation history is chosen to fit the photometry. In contrast, the formed stellar mass, m_{star}, derived from such best-fit parameters is a more robust quantity (cf. Papovich *et al.* 2001). We investigated the m_{star} implied by each best-fit $(E(B-V), t_{sf})$ combination as a function of star-formation history, and find that for the $\tau = 100$ Myr and $\tau = 50$ Myr models, the m_{star} derived is typically within a factor of 2 of the m_{star} derived for the constant star-formation model. For the $\tau = 10$ Myr models (these are effectively equivalent to an "instantaneous burst" model), the derived m_{star} is typically a factor of four smaller than the constant star-formation prediction— this relatively large difference is caused mostly by the degeneracy between an aging starburst and one which is relatively strongly reddened by dust. Star-formation histories with star-formation rates that are *increasing* functions of time pose even more significant problems for the models; for example, Papovich *et al.* (2001) have shown that an underlying maximally old stellar population (hidden by the most recent episode of star-formation) can contain up to 5× the stellar mass derived from the rest-frame UV-to-optical SED. In this sense, as emphasized by Papovich *et al.* , the inferred m_{star} based on the modeling should be treated as lower limits on the total stellar mass of the galaxies.

In short, broad-band photometry is not particularly effective in constraining star-formation histories— the root cause of this problem is that the far-UV flux is determined solely by the instantaneous rate of O and B star-formation, whereas the rest-frame optical flux is dominated by previous star-formation if the SFR is declining, and by the instantaneous star-formation if the rate is increasing. There is of course no good *a priori* reason to favor declining star formation rates over increasing ones. The simplest assumption is that the observed instantaneous star-formation rate is representative of the rate since the onset of the current episode of star-formation. Under these simplifying assumptions, short-lived "bursts" of star-formation for which the SFRs are much higher than the past average, will appear "young", and protracted periods of star-formation with relatively constant SFRs on timescales $\gtrsim 100$ Myr will have significant Balmer breaks that can be recognized in the broad-band photometry.

We summarize the best-fit and derived parameters for each galaxy assuming the BC96 constant star-formation models in Table 4. In Figure 8a, the measured photometry for three NIRC LBGs is plotted along with the best-fit constant star-formation models for the galaxies. These examples demonstrate the range of stellar population parameter space which is probed with NIRC LBGs. Figure 8b shows the $E(B-V) - t_{sf}$ confidence regions for these three galaxies.

5.2.4. Anomalous Galaxies

Most of the NIRC LBG spectroscopic sample was adequately described by the simple models detailed above. Statistically acceptable fits were obtained for 74 of the 81 LBGs in the NIRC sample with redshifts. Three of the remaining seven galaxies have suspect J and K_s photometry

upon closer inspection,[8] and fourth galaxy has a clear Seyfert-2-like spectrum. The remaining galaxies have colors that defy the simple models considered above. Two of the most anomalous galaxies are Westphal-MMD11 and DSF2237b-MD81. MMD11 and MD81 are the two reddest galaxies in $\mathcal{R} - K_s$ and $\mathcal{R} - J$ in the entire NIRC LBG sample, with $\mathcal{R} - K_s$ colors of 4.54 and 4.27, respectively, and $\mathcal{R} - J$ colors of 2.67 and 2.23. MMD11 is also in the reddest quartile of IGM-absorption corrected $G - \mathcal{R}$ measurements for the sample, while MD81 is in the bluest quartile (see Figure 1b). Neither MMD11 nor MD81 has a LRIS rest-frame UV spectrum with anomalously strong Lyman α emission or absorption, or notable interstellar or stellar features (though the signal-to-noise ratio in these spectra does not enable a quantitative examination). As discussed by AS2000, at $S_{850} = 5.5 \pm 1.4\,\mathrm{mJy}$ (Chapman *et al.* 2000), the 850μm flux of MMD11 is the strongest detection from the sample of optically selected LBGs that have been observed with SCUBA. Furthermore, MMD11 has a complex [OIII] 5007 nebular line profile, extended into two components along the spatial direction. While there is substructure present, the [OIII] equivalent width is one of the smallest which has been measured in LBGs (Pettini *et al.* 2001), and could not have contaminated the $\mathcal{R} - K_s$ colors by any significant amount. MD81 is not detected at 850μm at the $\sim$ 3mJy level (Chapman *et al.* , in preparation), and has not been studied with near-IR spectroscopy.

When we attempt to fit simultaneously the $G - \mathcal{R}$, $\mathcal{R} - J$, and $\mathcal{R} - K_s$ colors for either MMD11 or MD81, we are unsuccessful, mainly due to the extremely red optical-IR colors. Since MMD11 and MD81 are so bright in the near-IR, their well-determined colors have more power to discriminate the quality of a model fit than the more poorly determined optical-IR photometry for the majority of the NIRC sample. However, even if MMD11 and MD81 had $\mathcal{R} - J$ and $\mathcal{R} - K_s$ uncertainties which were more typical of the NIRC LBG sample, no satisfactory model fits would be obtained for MD81, and only marginally acceptable fits would be obtained for MMD11. Figure 9 shows various attempts to fit the colors of these anomalous galaxies. Estimates of dust reddening are obtained from fitting only the $G - \mathcal{R}$ color, assuming BC96 constant star-formation, and ages of 1 Myr and 1 Gyr. Clearly, the J and K_s points for both galaxies are significantly brighter than the predictions for even the 1 Gyr model. While a model with an age older than 1 Gyr might be able to fit the K_s points, the Balmer break present between J and K_s in such an old template spectrum would not be consistent with the well-determined, and bright, J measurements. For most of the galaxies in the NIRC LBG sample, this is not the case— even when fitting the $G - \mathcal{R}$ color alone, it is easy to find a model with the appropriate age and dust extinction to describe all of the photometry within the errors.

If we neglect the $G - \mathcal{R}$ color, and fit $\mathcal{R} - J$ and $\mathcal{R} - K_s$ alone, the best-fit models predict more than 7 magnitudes of extinction in the rest-frame UV and would significantly under-predict the

[8] the "suspect" photometry was obtained during variable observing conditions. an attempt was made to flux calibrate these measurements, but the optical-IR SED's for the relevant galaxies still indicate anomalous near-IR photometric points.

rest-frame far-UV fluxes. The very red optical-IR colors of these galaxies may indicate a problem with the Calzetti extinction law in cases where dust extinction is very extreme. In these cases, as in the case of local ultra-luminous infrared galaxies (ULIRGs), the details of the geometry and distribution of the dust relative to where star-formation is occurring become more important and the simple recipe for extinction breaks down (Trentham, Kormendy, and Sanders 1999; Meurer and Seibert 2001). For example, based on the $G - \mathcal{R}$ color alone, we would infer a moderate to low amount of dust extinction in MD81 (which may still be true). But such a small amount of extinction, with any age or star-formation history considered in this work, cannot account for the very red $\mathcal{R} - J$ and $\mathcal{R} - K_s$ colors of MD81. Alternatively, the inability to model these unusual galaxies might be due to the over-simplified nature of the star-formation histories considered.

5.3. Model Results

Using the sample of 74 galaxies for which acceptable BC96 continuous star-formation fits were obtained, we explore the trends present among observed and modeled quantities. These galaxies, all of which have redshifts, are brighter by an average of ~ 0.2 magnitudes in $\mathcal{R}$ than the NIRC LBG sample as a whole, and brighter by ~ 0.5 mag than the larger optical LBG photometric sample. It should be emphasized that the sample of HDF-N LBGs recently analyzed by Papovich *et al.* (2001) includes only four (of 33) galaxies brighter than L^* in the rest-frame UV LBG luminosity function, whereas 75% of the galaxies in the sample analyzed here are brighter than L^*. Differences between the two samples might then be ascribed to UV-luminosity-dependent effects, although we see only subtle trends with UV luminosity within our full ground-based sample spanning a factor of ~ 10 in UV luminosity.

Steidel *et al.* 1999 and AS2000 have computed the distribution of LBG $E(B-V)$ values based on IGM-absorption-corrected $G - \mathcal{R}$ colors alone, assuming a fixed intrinsic stellar population that corresponds to a BC96 continuous star-formation model with $t_{sf} = 1$ Gyr. With the addition of near-IR data, we have been able to model the extinction and variations in the stellar populations simultaneously. The inferred distribution of reddening, assuming the starburst attenuation relation of Calzetti (1997) and a suite of BC96 continuous star-formation models, has a median $E(B-V) = 0.155$, corresponding to $A_{1600} = 1.62$ magnitudes, similar to the median extinction presented in the earlier works. This reflects the fact that the previously-assumed galaxy SED is a reasonable approximation for the bulk of the sample in the rest-frame UV, and that most of the information on reddening comes from the far-UV data points even for a relatively "gray" extinction law.

The median age for our sample is $t_{sf} = 320$ Myr. More than 40% of the galaxies have $t_{sf} > 500$ Myr, while 25% have $t_{sf} < 40$ Myr. There were nine galaxies with formal best-fit t_{sf} values smaller than 10 Myr. Such small ages are not physically plausible for episodes of star-formation, given the dynamical timescales of the star-forming regions (see §7). Furthermore, the conversion between extinction-corrected UV luminosity and star-formation rate becomes

highly non-linear at ages shorter than 10 Myr. On these grounds, we restricted the best-fit constant-star-formation t_{sf} parameter space to ages of at least 10 Myr, which still provides acceptable fits for the nine youngest galaxies. We also applied the constraint that best-fit t_{sf} values could not be older than the age of the universe at $z \sim 3$ (assuming an $\Omega_m = 0.3$, $\Omega_\Lambda = 0.7$, $h = 0.7$ cosmology), which affected the fits for seven galaxies whose formal best-fit t_{sf} values were then too old. These galaxies, however, all had colors which were statistically consistent with being younger than the age of the universe at $z \sim 3$. As discussed in §5.2.3, the t_{sf} values for the NIRC LBG sample are affected in a systematic way by varying the star-formation history or the population synthesis models, but the sample as a whole should broadly represent the significant range in these parameters spanned by the LBGs at $z \sim 3$. We have noted that the distribution of t_{sf} values does not reflect corrections to the $\mathcal{R} - K_s$ color for nebular line emission for the 60% of the galaxies in the NIRC LBG sample which are at high enough redshift that the K_s measurement could be affected. However, there is no apparent systematic offset towards higher t_{sf} values for the higher-redshift portion of the sample as might be expected if the higher redshift objects were significantly biased due to nebular line contamination. Histograms of best-fit t_{sf} and $E(B-V)$ are shown in Figure 10a.

The median derived star-formation rate for the sample is $\Psi(t_{sf}) = 45h^{-2}M_\odot \mathrm{yr}^{-1}$, and the distribution of values is quite broad, ranging from $\sim 5h^{-2}M_\odot \mathrm{yr}^{-1}$ to as high as $\sim 940h^{-2}M_\odot \mathrm{yr}^{-1}$. Multiplying the best-fit t_{sf} and $\Psi(t_{sf})$ yields a distribution of m_{star}, with a median of $m_{star} = 1.2 \times 10^{10}h^{-2}M_\odot$, smaller but comparable to the present-day L^* stellar mass, $m_{star}(L^*) \sim 4.0 \times 10^{10}h^{-2}M_\odot$ (Cole *et al.* 2000; Papovich *et al.* 2001). However, we find that about 20% of the sample have m_{star} smaller than $4 \times 10^9 h^{-2}M_\odot$ (roughly the same sample with best-fit $t_{sf} < 40$ Myr). Histograms of the inferred m_{star} and $\Psi(t_{sf})$ distributions are shown in Figure 10b.

As mentioned above, a similar modeling technique for extracting physical parameters from observed colors of LBGs was used in recent work by Papovich *et al.* (2001); their sample of 33 galaxies in the HDF-N is a superset of earlier work by Sawicki & Yee (1998) on 17 HDF-N galaxies. The Papovich *et al.* HDF study, while containing all of the Sawicki & Yee galaxies, finds somewhat different results from Sawicki & Yee, including lower typical extinction factors, older ages, and larger formed stellar masses. The authors attribute some of these differences to their higher-quality HST NICMOS J and H data (compared to the Sawicki & Yee ground-based J and H), more accurate matching of optical and infrared photometry to compute colors, and larger galaxy sample. Here and above we have focused primarily on the more recent HDF-N analysis of Papovich *et al.* (2001).

The main difference between our modeling procedure and that of Papovich *et al.* is that the latter work allowed τ, the exponential star-formation decay time constant, to vary as a free parameter in fitting the models. As discussed above, there were few cases in which our data could discriminate between different values of τ that were significant compared to the inferred value of t_{sf}. However, a direct comparison of the model results is possible for 19 of the 33 galaxies in the

Papovich *et al.* work because the best-fit τ values are either longer than or much shorter than the inferred t_{sf}, so that the star-formation history is essentially indistinguishable from a constant star-formation model. For these 19 HDF-N galaxies, the median inferred age is $t_{sf} = 453\,\mathrm{Myr}$, and the median $E(B-V) = 0.095$. The median t_{sf} is thus higher, while similar, to the NIRC LBG median t_{sf}, and the median $E(B-V)$ is slightly smaller than that of the NIRC LBG sample. The remaining 14 HDF-N galaxies have best-fit $t_{sf} > \tau$, and t_{sf} values which are systematically lower than the $t_{sf} < \tau$ sample. However, the τ values for these galaxies are not very well constrained, and larger τ values also provide acceptable fits. The older t_{sf} values resulting from larger τ parameters would be roughly consistent with the t_{sf} values for the other 19 galaxies. Thus, given the uncertainties, it is probably fair to compare broadly the whole Papovich *et al.* sample to the NIRC-LBG sample. Our results are consistent with the inferred parameters for the small subset of the brightest HDF galaxies, including two galaxies in common between the two samples (see Table 3). Generally speaking, the UV-brighter NIRC LBG sample has a higher proportion of objects with large inferred extinction and with large values of the inferred stellar mass (these are generally distinct sets of objects, as discussed further below), both of which may be due to the different range of UV luminosity spanned within the two samples.

5.3.1. Extinction and Luminosity

Using observed optical and far-infrared (FIR) data, AS2000 and Meurer *et al.* (1999) demonstrated that at both low and high redshifts, there appears to be a correlation between dust-obscuration and bolometric luminosity ($L_{\mathrm{bol,dust}}/L_{UV} \approx L_{\mathrm{bol,dust}}$). The results of our modeling of the LBG SEDs support the assertion that more heavily obscured galaxies have larger bolometric luminosities; however, because many of our assumptions are similar— most notably, the adopted starburst attenuation relation, our new results cannot be taken as independent evidence. As in AS2000, we find that the rest-frame UV luminosity is uncorrelated with the inferred value of $E(B-V)$, so that applying the inferred extinction correction naturally results in a strong correlation between bolometric luminosity and extinction. As emphasized by AS2000, inferences about extinction in the high redshift galaxies are very difficult to test observationally, but the trends are very similar to what is observed for star-forming galaxies in the local universe and, so far, the starburst attenuation relation is consistent with available cross-checks at high redshift. We note in passing that internally consistent application of the inferred extinction corrections to the rest-frame optical luminosities results in a similar correlation of dust obscuration and optical luminosity, and a net correction to the V-band luminosity density of a factor of ~ 2 compared to the uncorrected numbers presented in §4. The correlations of the UV and optical luminosities with best-fit $E(B-V)$ are shown in Figure 11 for BC96 continuous star-formation models. These correlations hold for the all of the star-formation histories used in this work to model the galaxy colors, and would hold for any assumed extinction relation that is correlated with rest-UV color.

5.3.2. Extinction and Age

In Figure 12 we plot the best-fit $E(B-V)$ and t_{sf} parameters for the 74 galaxies successfully fit with BC96 constant-star-formation models. There is a very strong anti-correlation between $E(B-V)$ and t_{sf} in the sense that younger galaxies are more heavily extinguished than older galaxies. Given the strong correlation between $\Psi(t_{sf})$ and $E(B-V)$ discussed in §5.3.1, the relationship between extinction and age translates into a link between age and star-formation rate, where the youngest galaxies also have the highest star-formation rates. The correlation in the sample between $E(B-V)$ and t_{sf} falls roughly in the same direction as the observed covariance of the $(E(B-V), t_{sf})$ parameters for each individual galaxy. The covariance of $E(B-V)$ and t_{sf} is dominated in most cases by response of the fitted parameters to perturbations in the $G-\mathcal{R}$ color. Typically, a positive perturbation to the $G-\mathcal{R}$ results in a *positive* perturbation to the best-fit $E(B-V)$ and a *negative* perturbation to the best-fit t_{sf}, the latter due to the effect of the extinction estimate on the predicted $\mathcal{R}-K$ color for a given t_{sf}. The covariance of the two parameters is clearly demonstrated by the NIRC LBG confidence regions shown in Figure 8b.

Given the strong covariance between best-fit $E(B-V)$ and t_{sf} parameters inherent in the modeling procedure, further tests are necessary to evaluate whether the trend of increasing extinction with decreasing t_{sf} is significant. In other words, does the apparent correlation arise solely due to objects' covariant confidence regions in $E(B-V)-t_{sf}$ space, because measurement errors can scatter intrinsically uncorrelated points along the same direction as an $E(B-V)-t_{sf}$ correlation? In order to test the strength of such an apparent correlation, we constructed a sample of 74 uncorrelated $E(B-V)$ and t_{sf} pairs (to match the size of the observed sample of 74 galaxies). This sample was generated by randomly selecting $E(B-V)$ and t_{sf} values independently from the *intrinsic* marginal distributions of each of the parameters. These *intrinsic* marginal distributions were estimated by assuming that the *observed* marginal distributions (shown in Figure 10a) represented the *intrinsic* marginal distributions broadened by photometric measurement errors. In addition to $E(B-V)$ and t_{sf}, $\mathcal{R}$ apparent magnitude and z were randomly selected from the observed distributions of $\mathcal{R}$ and z for NIRC LBGs, in order to compute the colors that would be observed from a galaxy with the randomly selected $E(B-V)$ and t_{sf} parameters. A fake galaxy was retained only if its $E(B-V)$ and t_{sf} parameters implied a $G-\mathcal{R}$ color satisfying the LBG selection criterion of $G-\mathcal{R} \leq 1.2$, and a K_s magnitude brighter than the typical NIRC LBG detection limit of $K_s = 22.5$. Photometric uncertainties were assigned to each fake galaxy's predicted set of colors, based on the galaxy's $\mathcal{R}$ magnitude and colors, and the previously determined functions of $\sigma(\mathcal{R}, G-\mathcal{R})$, $\sigma(\mathcal{R}, \mathcal{R}-J)$, and $\sigma(\mathcal{R}, \mathcal{R}-K_s)$ (see §2.4).

The sample of fake galaxies was then "observed" a large number (1000) of times. Each time, the colors of the fake galaxies were perturbed in a manner consistent with their photometric errors (a process similar to the one used to construct the confidence intervals for the 74 real observed galaxies). The result of observing the fake galaxies numerous times with measurement errors was a large distribution of best-fit $E(B-V)$ and t_{sf} values (the number of fake galaxies (74) multiplied by the number of trials (1000)). The marginal distributions of $E(B-V)$ and t_{sf} for

this large simulated distribution matched the observed marginal distributions of $E(B-V)$ and t_{sf} in Figure 10a — which verifies that our estimate of the intrinsic marginal distribution was reasonable. We then randomly selected a large number of groups of 74 best-fit $E(B-V)-t_{sf}$ pairs from the sample of 74,000 "observed" galaxies, and computed the correlation coefficient between $E(B-V)$ and t_{sf} for each randomly selected sample. In 1000 random samples of 74 fake best-fit $E(B-V)-t_{sf}$ values, *no* sample had a correlation coefficient as strong as the one seen in the real sample. Thus, *it appears that the age/extinction correlation for NIRC LBGs has less than a* 0.1% *chance of being the result of correlated measurement errors alone.*

A related question is whether the detection limits and selection criteria for the sample could have created an apparent dearth of young, unreddened galaxies, and old, dusty galaxies, which would mimic a real correlation between $E(B-V)$ and t_{sf}. For the redshift range of the sample, the BC96 constant star-formation models with $E(B-V)\sim 0$ and $t_{sf}\leq 100\,\mathrm{Myr}$ have $G-\mathcal{R}$ within the range for LBGs ($-0.02 < G-\mathcal{R} < 0.35$), but also very blue $\mathcal{R}-K_s$ colors ($\mathcal{R}-K_s \leq 1.86$). A detection limit in K_s translates into a limit in $\mathcal{R}-K_s$ as a function of $\mathcal{R}$. However, since there are $\mathcal{R}-K_s$ limits rather than detections for only 3 out of 81 galaxies with redshifts in the NIRC sample, we conclude that our K_s detection limit has not prevented us from detecting a significant population of young, unreddened galaxies. At any redshift in the NIRC sample, old and reddened galaxies, with $E(B-V) > 0.15$ and $t_{sf} \geq 1\,\mathrm{Gyr}$, have predicted $\mathcal{R}-K > 3.00$, which means that all such galaxies with $\mathcal{R} < 25.5$, should be detected in $\mathcal{R}-K_s$. At the median redshift of the NIRC sample, the LBG selection limit of $G-\mathcal{R} < 1.20$ implies that we should be able to detect old galaxies with $E(B-V) \leq 0.30$, which is more than one standard deviation to the red of the mean of the sample. At increasing redshift, the upper limit on $E(B-V)$ decreases until at the highest redshift in the NIRC sample, $z = 3.396$, it is only possible to select a 1 Gyr model with $E(B-V) \leq 0.14$ as a LBG, based on $G-\mathcal{R}$. Such a redshift dependent effect discriminates against old and very dusty objects at the high redshift end of the LBG redshift selection function. To test the significance of such an effect, the sample of 74 galaxies was divided into low and high redshift subsamples, using the median redshift as a discriminator. All of the galaxies in the low redshift sample have $z \leq 3.061$, at which redshift a 1 Gyr stellar population could be detected with $E(B-V) \leq 0.300$. Despite the fact that $E(B-V)$ is barely restricted for the low redshift sample, a strong correlation between $E(B-V)$ and t_{sf} is recovered from this sample, as well as from the high redshift and total samples. We conclude that the redshift-dependent bias against detecting old and dusty galaxies cannot account for the strong correlation found between $E(B-V)$ and t_{sf} in the NIRC sample either.

The inferred strong correlation between star-formation age and extinction does depend on the details of the attenuation law applied to correct observed galaxy colors and magnitudes to their intrinsic, unobscured values. At low redshift, relatively "gray" starburst galaxy attenuation relations such as that of Calzetti (1997) provide a much better predictor of bolometric luminosity from far-UV observations than the reddening curves derived from observations of single stars, such as the SMC, LMC, and Galactic reddening curves (Meurer *et al.* 1999). There are very few

observations to constrain the nature of dust extinction in galaxies at high redshift; however, the limited information which exists favors the starburst attenuation relation over a much steeper curve such as the SMC law (Meurer *et al.* 1999, AS2000). Nevertheless, if the SMC law is used with the BC96 constant star-formation models, instead of the Calzetti relation, the best-fit extinction values at 1600 Å (A_{1600}) are systematically smaller, by a median factor of 2.7, and the t_{sf} values are systematically larger. The ratio between SMC and Calzetti t_{sf} values increases as a function of increasing extinction, but the median ratio is 3.7. Qualitatively, the larger SMC t_{sf} values result from interpreting a larger fraction of the $\mathcal{R} - K_s$ color as due to the Balmer break (aging stellar population), and a smaller fraction as due to the effects of dust extinction.[9] The result of using the SMC law is that the correlation between inferred extinction and inferred age is very much diminished.

5.3.3. Stellar Mass

The formed stellar mass, m_{star}, for the constant star-formation models is simply the product of the best-fit t_{sf} and $\Psi(t_{sf})$. Figure 13 shows the relationship between m_{star} and observed and intrinsic (extinction-corrected) luminosity values. When the sample is restricted to galaxies with best-fit $t_{sf} > 320$ Myr (the median for NIRC LBGs), there are significant correlations between both UV and optical extinction-corrected luminosities and m_{star}. However, when the whole NIRC LBG sample is considered, the extinction-corrected UV and optical luminosities are only weakly correlated with m_{star}, indicating that, for the wide range of extinction and age parameters found in the NIRC LBG sample, even rest-frame optical luminosities (the longest accessible wavelengths for $z \sim 3$ galaxies until the Space Infrared Telescope Facility (SIRTF) flies) often have more to do with current star-formation rates than with formed stellar masses. Thus, as emphasized by Papovich *et al.* (2001), the estimates of the formed stellar mass associated with the most recent star-formation episode must rely on the IMF-dependent population synthesis modeling until longer wavelength observations are possible. However, Papovich *et al.* also explored the dependence of inferred m_{star} on the modeling assumptions for a given observed galaxy SED, concluding that, while variation of the modeling parameters yields highly variable results for parameters such as age and extinction, the combination of best-fit pairs of these parameters generally results in much more tightly constrained m_{star} estimates for the modeled star formation episode. While exploring a smaller volume of parameter space, we confirm this trend for the formed stellar mass values (cf. §5.2.3).

Our results should be compared directly with the solar metallicity, Salpeter IMF models of Papovich *et al.* (2001) (their Figure 17), where the characteristic formed stellar mass is $\sim$ a few $\times 10^{10}$ $M_\odot$ for objects with UV luminosities of L^* in the far-UV luminosity function of Steidel

[9]In fact, the inverse effects on extinction and age from using an SMC law tend to cancel out in the calculation of formed stellar mass, which is typically only 30% larger when using the SMC rather than Calzetti law.

et al. (1999). Our NIRC sample, which has a median luminosity of somewhat brighter than L^*, has a median inferred stellar mass of 2.5×10^{10} $M_\odot$ using the $h = 0.7$ cosmology adopted by Papovich *et al.* al. Thus, in the small region of overlap, the ground-based sample yields results similar to the brightest HDF-N galaxies. In contrast to Papovich *et al.* , who found that the UV luminosity was well correlated with the inferred stellar mass, we find that the UV luminosity is uncorrelated with the inferred m_{star}. This may reflect a real difference between the brighter and fainter samples. One possible explanation could be that we see a wider range of extinction among the NIRC LBGs than is found at fainter UV luminosities (e.g., objects of a given UV luminosity can be either heavily extinguished very luminous objects, or modestly extinguished, much less luminous objects) such that the relationship between UV luminosities uncorrected and corrected for extinction is much less tight (see AS2000). Because of the very small overlap in UV luminosity between the two samples, the differences are at present statistically insignificant.

There are 9 objects[10] from the NIRC sample which also have nebular line width measurements from near-IR spectroscopy (Pettini *et al.* 2001). We use the nebular line widths and the measured near-IR half-light radii to compute the dynamical mass enclosed within the half-light radius. The mass inferred from the nebular line widths is probably not indicative of the total mass in the dark-matter halo containing the LBG, but is likely to represent a lower limit (see Pettini *et al.* 2001). Similarly, since the inferred stellar mass estimates are only sensitive to the most recent episode of star-formation, they should also represent lower limits on the total stellar mass present. However, the near-infrared spectroscopic and photometric measurements generally span the same physical region, which contains not only stellar mass, but also gas and dark matter. The spectroscopic line widths should be sensitive to all this matter, while the photometry only probes the luminous stellar matter. Therefore, the mass inferred from the nebular line widths should represent a rough upper limit to the m_{star} values derived from the BC96 model fits. We would suspect a problem in the population synthesis modeling technique if the derived m_{star} values were much larger and statistically discrepant with the inferred dynamical masses. As shown in Figure 14, for the majority of the galaxies, the m_{star} value is consistent with the inferred dynamical mass; in two cases where it is not, the best-fit stellar mass is significantly smaller than the inferred dynamical mass. We refrain from drawing conclusions from Figure 14, given the very large uncertainties in both mass estimates, but there is no evidence that the two mass scales are wildly inconsistent with one another.

6. "Young" and "Old" LBGs: Spectral Differences

One of the more striking results from the modeling of LBG stellar populations is the strong correlation between extinction and age, such that the galaxies best fit by younger stellar

[10]One is Westphal MMD11, which we were unable to model successfully, and so it has not been included in this discussion.

populations are also best described by larger amounts of extinction and reddening. As discussed in §5.3.2, we believe that this correlation is significant, despite the tendency for the individual $(E(B-V), t_{sf})$ covariance intervals to lie in a similar direction to the observed sample correlation, and despite a $G-\mathcal{R}$ selection criterion which prevents a galaxy older than 1 Gyr with significant amounts of dust extinction from being classified as a LBG at the highest redshifts in the sample. Assuming that the correlation is real, there are implications for interpreting the range of LBG best-fit stellar populations and extinction parameters. It appears that the distributions of LBG star-formation ages, extinction, and inferred stellar masses fall along a continuum in the parameter space, the extremes of which might be viewed as separate "populations". To illustrate this point, we isolate 16 galaxies with best-fit $t_{sf} \geq 1$ Gyr, and 16 galaxies with $t_{sf} \leq 35$ Myr. In the discussion which follows, the ~ 1 Gyr subsample is referred to as the "old" sample, and the ≤ 35 Myr subsample is labeled "young." The "young" sample has $\langle E(B-V) \rangle = 0.260$, $\langle \Psi(t_{sf}) \rangle = 210 h^{-2} M_{\odot} \mathrm{yr}^{-1}$, and $\langle m_{star} \rangle = 2.9 \times 10^9 h^{-2} M_{\odot}$. In contrast, the "old" sample has $\langle E(B-V) \rangle = 0.100$, $\langle \Psi(t_{sf}) \rangle = 25 h^{-2} M_{\odot} \mathrm{yr}^{-1}$, and $\langle m_{star} \rangle = 4.0 \times 10^{10} h^{-2} M_{\odot}$. The young sample is characterized by 2 magnitudes more dust extinction in the rest-frame UV than the old sample, star-formation rates at least an order of magnitude higher (even when restricting the best-fit t_{sf} values to be above a reasonable minimum age), and formed stellar masses more than an order of magnitude smaller.

To investigate further the distinctions between galaxies in the young, dusty subsample and those in the older, less reddened group, we drew from our database of LBG rest-frame far-UV spectra, collected by our group between October 1995 and November 1999 (Steidel *et al.* 1996a,b, 1998, 1999). By combining individual rest-frame UV spectra of galaxies in the "young" and "old" subsamples described above, we constructed "young" and "old" composite spectra following a method similar to that described in Steidel, Pettini, & Adelberger (2001).

The young and old composite spectra are plotted in Figure 15, and Figure 16 shows an expanded view of four specific regions of the spectra for more detailed comparison. There are several clear differences to note, the most dramatic of which is in the relative Lyman α line profiles. The old spectrum has strong Lyman α emission with rest-frame $W_\lambda = 20$ Å, whereas the young spectrum has a broad absorption trough plus much weaker emission which combine to give roughly $W_\lambda = 0$. The radiative transfer of Lyman α photons in galaxies is a complex process which depends not only on the amount of dust present in the ISM but also, and perhaps more importantly, on the geometry and kinematics of the neutral interstellar hydrogen gas (Charlot & Fall, 1993; Chen & Neufeld 1994; Kunth *et al.* 1999; Tenorio-Tagle *et al.* 1999). However, due to resonant scattering, Lyman α photons will on average traverse a much longer path before escaping the galaxy than nearby continuum photons, so that they are more prone to absorption by dust in the ISM. Therefore, the amount of dust present in the ISM should have a non-negligible effect on the emergent Lyman α profile. The fact that the composite "young" spectrum exhibits a Lyman α profile with a combination of absorption and only weak emission, while the composite "old" spectrum has very strong Lyman α emission, offers independent support for a scenario in which

the youngest galaxies have significantly dustier interstellar media than more mature LBGs.

Additionally, the young spectrum has much stronger Lyman β absorption, stronger low-ionization interstellar metal absorption lines of Si II $\lambda 1192, 1260,$ and $1526,$ C II $\lambda 1334$, Fe II $\lambda 1608$, and a stronger P-Cygni C IV $\lambda 1549$ profile. The only interstellar metal absorption line which is stronger in the old spectrum is Al II $\lambda 1670$. While the S/N ratios of the composite spectra represent large improvements over that of the individual spectra, the significance of the differences in line strengths between the old and young spectra is still difficult to quantify, given the noise in the composite spectra and the relatively small sample of objects whose spectra were combined. We therefore choose to make more qualitative observations. The low-ionization interstellar absorption lines are probably optically thick, and therefore on the flat part of the curve of growth, where equivalent width is determined mainly by velocity width, and not column density (Steidel *et al.* 1996a, Gonzalez Delgado *et al.* 1998, Heckman & Leitherer 1997). Accordingly, the stronger interstellar absorption lines in the young spectrum may indicate interstellar medium velocity widths larger than those in the old spectrum. Larger velocity widths are consistent with a scenario in which a higher supernova rate (based on the higher $\Psi(t_{sf})$) deposits larger amounts of mechanical energy into the ISM, accelerating the interstellar gas to higher velocities.

7. A Proposed Evolutionary Sequence for LBGs

A picture begins to emerge from the range of stellar populations observed in the NIRC LBG sample. At one extreme of the continuum, there is a group of galaxies with best-fit ages younger than or equal to the dynamical timescale associated with the luminous portions of LBGs. Based on NIRC and HST-WFPC2 observations, the typical LBG angular half-light radius is $0\farcs25$ (Giavalisco *et al.* 1996; Pettini *et al.* 1998). This angular size translates into $r_{hl} = 1.3\,h^{-1}$ kpc at $z = 3$. Furthermore, from near-IR spectroscopic measurements of a sample of 15 LBGs, the typical nebular line widths are $\sigma \simeq 80$ km s^{-1}(Pettini *et al.* 2001). The associated dynamical timescale is $t_{dyn} \simeq \frac{2r_{hl}}{\sigma}$. With typical values for r_{hl} and σ, this calculation yields $t_{dyn} \simeq 30\,h^{-1}$ Myr. A starburst cannot occur on timescales shorter than the dynamical timescale of the region experiencing star-formation, for reasons of causality. Since a constant star-formation model with an age less than or equal to the dynamical timescale is indistinguishable from a bursting mode with a decay time, τ, limited to be greater than or equal to the dynamical timescale, the young, dusty galaxies in the NIRC LBG sample might well be described as galaxies undergoing bursts of star-formation. Whatever the cause of the burst of star-formation, we see intense star-formation and enhanced dust extinction in the youngest galaxies. At the other extreme are the galaxies whose best-fit constant star-formation t_{sf} values are close to a Hubble time at $z \sim 3$, whose dust extinction is only moderate, and whose star-formation rates are more quiescent. The NIRC LBG sample also contains galaxies with ages, dust-extinction, and star-formation rates which are intermediate between these two extremes.

Since the range of NIRC LBG stellar populations is controlled by two strong correlations— one

between dust and age, and another between dust and intrinsic star-formation rate— we use these correlations to construct a unified evolutionary model for LBGs at high redshift. According to this model, the "young" and "old" samples discussed in this section constitute different evolutionary stages of the same population, which are both selected as LBGs. The "young" galaxies represent objects in the first stage, where the star-formation rate is very active ($\geq 200h^{-2}M_{\odot}$ yr^{-1}), large amounts of dust obscure the sites of star-formation, and a stellar mass on the order of $10^9 M_{\odot}$ is formed in a dynamical timescale. As time passes, dust is either destroyed or blown out, (or both), resulting in lower extinction, and the star-formation rate decays on a $\sim 50 - 100$ Myr timescale to reach the more quiescent rates seen in the "old" sample ($\sim 25h^{-2}M_{\odot}$ yr^{-1}). The "old" sample then represents the most advanced stage of the evolution which we observe in $z \sim 3$ LBGs, by which stage a stellar mass of $\gtrsim 10^{10} M_{\odot}$ has formed. As discussed earlier, for most "old" LBGs, it is not possible to distinguish from a strong Balmer break whether constant star-formation has continued for at least 1 Gyr, or whether exponentially declining star-formation has continued well past the age of the time constant, τ. If the relatively quiescent star-formation rates of the old galaxies are extrapolated back to the ages of the young/dusty sample assuming an exponentially declining star-formation rate with a time constant on the order of the dynamical timescale for LBGs, the star-formation rates obtained are on the order of the active rates in the young-dusty sample.

Such a simple evolutionary picture for LBGs is qualitatively consistent with the strong correlations we see in the NIRC LBG stellar population parameters. This evolutionary picture predicts a relatively flat distribution of t_{sf} values, which is broadly consistent with the observed t_{sf} histogram (Figure 10a) except for the smallest t_{sf} bin, which is "over-sampled" in the NIRC LBG data set by about a factor of two (§2.2). While correcting the youngest bin by this amount makes the t_{sf} distribution flatter, the youngest bin still contains more galaxies than the other bins, implying that some fraction of the young, dusty, actively star-forming galaxies may fade to star-formation rates which are too low to be detected with the (ground-based) LBG criteria.

There are several interesting issues which accompany the above scenario. First, there is the question of what process produces the initial, rapid star-formation phase. Some obvious possibilities are major or minor merger events (e.g., Somerville *et al.* 2001; Mihos & Hernquist 1996), or even the initial collapse of the baryonic component of the galaxy. Second, there is the question of how the large amount of dust in the significantly reddened "young" galaxies forms, given the relatively short timescales implied by the ages of these galaxies— how much of the dust is formed in the current star-formation episode, and how much originated in previous generations of stars?

Another important issue is the process by which dust is depleted as "young" LBGs evolve into "old" galaxies. There are a few proposed mechanisms for the removal of dust from galaxies. The first is radiation pressure, by which dust grains (especially larger ones $\sim 0.1\,\mu$m in size) can be expelled by the general radiation field of a galaxy. Davies *et al.* (1998) have numerically modeled the removal of dust from a present-day L^* spiral galaxy by radiation pressure, and have shown that

up to 90% of the dust formed in such a galaxy may be ejected from the disk. While the relevant physical conditions might not be identical in local spiral galaxies and the high redshift LBGs, radiation pressure provides one viable mechanism by which dust can be removed from galaxies. Perhaps more relevant to the conditions in LBGs is the observational evidence for galactic-scale outflows, so-called "superwinds," in actively star-forming local galaxies. These outflows are due to the combined mechanical energy input from supernovae and winds from massive stars, which sweeps up interstellar material and accelerates it to speeds of several hundred km s^{-1} or greater (Heckman *et al.* 1990, Heckman *et al.* 2000). There is strong kinematic evidence for such outflows in LBGs at high-redshift as well (Franx *et al.* 1997; Steidel *et al.* 1998; Pettini *et al.* 1998, 2000, 2001). Relative to the nebular emission lines representing the systemic velocity of the galaxy, low-ionization interstellar absorption lines in LBG rest-frame UV spectra are blue-shifted by ~ 300km s^{-1}, and Lyman-α emission is redshifted by $200 - 1100$ km s^{-1} (Pettini *et al.* 2001). The implied typical outflow velocities are $\sim 400 - 500$ km s^{-1}, and in the best studied case (Pettini *et al.* 2000) the implied mass outflow rate equals or exceeds the current star-formation rate (similar to what is seen in local starburst galaxies— e.g. Martin 1999).

Recently, there has been direct observational evidence that dust, as well as gas, has been swept up by starburst superwinds and is contained in the material outflowing from local starburst galaxies (Heckman *et al.* 2000; Alton, Davies, & Bianchi 1999). Heckman *et al.* (2000) determine a typical outflowing dust mass of $10^6 - 10^7 M_\odot$ with a typical dust outflow rate of $0.1 - 1 M_\odot$ yr^{-1} for the starbursts in their sample. While there are no direct observations of dust in LBG outflows, the presence of dust in the ISM of LBGs is required by their broad-band colors. It seems very reasonable that the dust in the ISM of LBGs becomes entrained in the outflows implied by the kinematics of UV interstellar and nebular spectral features. The process of dust being expelled in superwinds from starburst galaxies at high redshift is qualitatively consistent with the observed trend between extinction and star-formation age in LBGs. Indeed, the superwind phenomenon has important implications not only for the enrichment of the intergalactic medium, but also for the evolution of dust opacity in galaxies.

8. SUMMARY AND CONCLUSIONS

We have presented the results of a near-IR survey of optically selected $z \sim 3$ LBGs. The survey includes 118 galaxies with K_s measurements, 63 of which also have J measurements. We combined the new near-IR data with previously obtained optical data to compute the distributions of optical-IR colors of LBGs. We have used the photometric data, spanning typical rest-frame wavelengths of 900–5500 Å to obtain the following results:

1. The rest-frame optical luminosity function of UV-selected LBGs greatly exceeds locally determined luminosity functions at the bright end. A Schechter function fit formally yields a very steep ($\alpha = -1.85 \pm 0.15$) faint-end slope, but part of this could be due to the fact that at our detection limit of $K_s = 22.5$ ($M_V = -20.41 + 5\log h$ at $z \sim 3$) the data do not extend significantly

beyond the knee in the luminosity function and the overall shape of the luminosity distribution is quite different from the local functions. Independent of the fitted parameters, the $z \sim 3$ optical luminosity function has a large excess of luminous galaxies relative to locally determined luminosity functions. Down to our detection limit of $K_s = 22.50$ (or a luminosity equivalent to $\sim 1.2L^*$ in the present-day V-band luminosity function), the rest-frame optical co-moving luminosity density of LBGs (uncorrected for dust extinction) is $\rho_V = 1.35 \times 10^8 L_\odot h\,\mathrm{Mpc}^{-3}$. This value is already within a factor of 2 of values determined by integrating local luminosity functions down to arbitrarily small luminosities. Thus, the optical light from LBGs at $z \sim 3$ likely exceeds that produced by all stars in the local universe.

2. We have modeled the stellar populations and extinction of the LBGs with both spectroscopic redshifts and near-IR measurements (81 galaxies) using relatively simple prescriptions. Most of the galaxies have star-formation histories, star-formation rates, and star-formation ages that are only weakly constrained by the photometric observations without limiting parameter space using external constraints on the assumed extinction law and relatively simple forms for the star-formation history. We have chosen to report the results assuming the solar-metallicity Bruzual and Charlot (1996) models, a Salpeter IMF, the Calzetti (1997) starburst attenuation relation, and a constant star-formation history. The systematic effects of changing the any of these assumptions have been summarized.

3. When the interpretation of LBG stellar populations is restricted to BC96 constant star-formation models, we find a large spread of inferred ages, ranging from several Myr to more than 1 Gyr. The median best-fit constant star-formation age is $t_{sf} = 320$ Myr. In model-independent terms, the distribution of best-fit ages indicates that a significant fraction of LBGs have been forming stars on timescales long enough that a detectable Balmer break exists in their spectral energy distributions. Although the specific age assigned to the Balmer break depends on the star-formation history used to fit the colors, we note that very recent work indicates that winds from LBGs similar to those modeled above have shock-heated the intergalactic medium on physical scales of $100 - 200h^{-1}$ kpc (Adelberger *et al.* 2001, in preparation). Such a large sphere of influence, with typical outflow velocities of a few hundred km s^{-1}, suggests star-formation timescales of at least a few hundred million years for typical LBGs. This constitutes completely independent support for the timescales resulting from the stellar population modeling presented in this work. The BC96 constant star-formation distribution of best-fit $E(B-V)$ ranges from $\sim 0.0 - 0.45$ with a median of 0.155. This distribution depends less on star-formation history than the distribution of best-fit ages. The median implied extinction for this sample corresponds to a factor of ~ 4.5 attenuation in the rest-frame UV (1600 Å) and a factor of $\sim$2 in the rest-frame optical. Derived from the distributions of $E(B-V)$ and t_{sf}, the best-fit star-formation rate, $\Psi(t_{sf})$, ranges from $5 - 940h^{-2}M_\odot\,\mathrm{yr}^{-1}$, with a median of $45h^{-2}M_\odot\,\mathrm{yr}^{-1}$. The distribution of formed stellar masses, m_{star}, ranges over more than 2 orders of magnitude with a median of $\sim 10^{10}h^{-2}M_\odot$. We note that the above parameter distributions and median values may not be completely general to LBGs at $z \sim 3$, since the way in which the NIRC LBGs were selected tended

to enhance the number of young, dusty, intensely star-forming, low m_{star} objects, relative to the full LBG sample.

4. Regardless of the star-formation history used in this work to model the colors of the NIRC LBGs, we find a strong correlation between dust extinction and intrinsic luminosity, such that dustier galaxies are intrinsically more luminous. This correlation has been reported by other authors (AS2000; Meurer *et al.* 1999), but here the extinction estimates are supported by observations over a wider wavelength baseline, spanning on average from $900 - 5500$ Å in the rest-frame. This dependence of extinction on luminosity is consistent with a similar relation seen for star-forming galaxies in the local universe, and has the implication that, for the range of galaxies which we select as LBGs, those which are more heavily obscured by dust are as easy to detect in the rest-frame UV and optical as galaxies which are less dusty, because they are also intrinsically more luminous.

5. For most galaxies, we find that the formed stellar mass derived from the integral of the best-fit star-formation rate over time depends relatively weakly on the star-formation history applied to fit the observed colors (cf. Papovich *et al.* 2001). Regardless of star-formation history, the inferred formed stellar mass is only weakly correlated with extinction corrected UV and optical luminosities for our total ground-based sample. This fact, together with the results on the rest-frame optical luminosity function of LBGs, shows that even at observed wavelengths of 2.15 μm, the luminosities are poor proxies for stellar mass in general. Therefore, inferences on stellar mass from optical/near-IR photometry are highly IMF-dependent and will apply only to the stars that have formed in the last several hundred Myr prior to observation. Longer-wavelength observations with SIRTF should improve the situation considerably.

6. We find a strong correlation between inferred star-formation age and extinction in LBGs, such that younger galaxies are dustier than older galaxies, and have higher star-formation rates. Establishing the significance of this correlation is difficult because of the covariance of $E(B-V)$ and t_{sf} in our fits, but we have been unable to reproduce a similarly strong observed correlation from any intrinsically uncorrelated distributions of $E(B-V)$ and t_{sf}. The correlation might be made to vanish with a suitable choice of star-formation histories or dust attenuation curve (i.e. SMC), but its existence appears secure for the most plausible choices of both. We also present evidence that this correlation is not an artifact of either the LBG $G - \mathcal{R}$ selection criteria, or of the typical detection limit of $K_s = 22.5$ for the NIRC observations.

7. Composite rest-frame UV spectra of "young" and "old" subsamples of NIRC LBGs exhibit differences, most dramatically in their respective Lyman-α profiles, offering independent evidence that the youngest galaxies have more dust extinction and/or more active interstellar media. We interpret the dust-age correlation in the context of a unified picture of LBGs in which the younger, dustier, more actively star-forming galaxies evolve into the older, less reddened, and more quiescent galaxies. The evolution of the dust extinction towards lower values is probably governed by the outflow of dust which is entrained in a "superwind" powered by the energy from supernovae

explosions and the winds from massive stars. Objects at various points along this evolutionary sequence are identified by the LBG optical selection criteria. The timescale for the evolution of the young-dusty galaxies into the older-less-reddened galaxies is on the order of $50 - 100$ Myr, while the more quiescent phase can last a Gyr or more.

We would like to thank the staffs of the Palomar, La Palma, Kitt Peak, and Keck Observatories for their assistance in both optical and near-infrared observations. We would also like to thank Matthew Hunt, for assistance with the near-IR data reduction, and Stephane Charlot for helpful discussions and assistance in implementing the most up-to-date Bruzual and Charlot spectral synthesis codes. Finally, we wish to extend special thanks to those of Hawaiian ancestry on whose sacred mountain we are privileged to be guests. Without their generous hospitality, most of the observations presented herein would not have been possible. CCS, KLA, and AES have been supported by grants AST95-96229 and AST-0070773 from the U.S. National Science Foundation and by the David and Lucile Packard Foundation.

REFERENCES

Adelberger, K.L. 2001, Ph. D. Thesis

Adelberger, K.L., & Steidel, C.C. 2000, ApJ, 544, 218

Adelberger, K.L., Steidel, C.C., Giavalisco, M., Dickinson, M.E., Pettini, M., & Kellogg, M. 1998, ApJ, 505, 18

Alton, P.B., Davies, J.I., & Bianchi, S. 1999, A&A, 343, 51

Baugh, C. M., Cole, S., Frenk, C. S., & Lacey, C. G. 1998, ApJ, 498, 504

Blanton, M. et al. 2001, AJ, accepted (astro-ph/0012085)

Binney, J. & Merrifield, M. 1998, Galactic Astronomy (Princeton: Princeton University Press) Prevot-Burnichon, M. L. 1985, A&A, 149, 330

Bruzual, G., & Charlot, S. 1996, BC96 manual (private communication)

Calzetti, D. 1997, AJ, 113, 162

Chapman, S. et al. 2000, MNRAS, 319, 318

Charlot, S., & Fall, S.M. 1993, ApJ, 415, 580

Chen, W.L., & Neufeld, D.A. 1994, ApJ, 432, 567

Cole, S. et al. 2000, MNRAS in press (astro-ph/0012429)

Davies, J.I., Alton, P.B., Bianchi, S., Trewhella, M. 1998, MNRAS, 300, 106

Dickinson, M.E., 2000, Phil. Trans. R. Soc. Lond. A, 358, 2001

Folkes, S. et al. 1999, MNRAS, 308, 459

Franx, M., Illingworth, G. D., Kelson, D. D., van Dokkum, P. G., & Tran, K.-V. 1997, ApJ, 486, L75

Fukugita, M., Hogan, C.J., Peebles, P.J.E. 1998, ApJ, 503, 518

Giavalisco, M., & Dickinson, M. E. 2001, ApJ, 550, 177

Giavalisco, M., Steidel, C. C., Adelberger, K. L., Dickinson, M. E., Pettini, M., & Kellogg, M. 1998, ApJ, 503, 543

Giavalisco, M., Steidel, C. C., & Macchetto 1996, ApJ, 470, 189

Gonzalez Delgado, R.M., Leitherer, C., Heckman, T.M., Lowenthal, J.D., Ferguson, H.C., & Robert, C. 1998, ApJ, 495, 698

Gray, D. F. 1976, The Observation and Analysis of Stellar Photospheres (New York: Wiley)

Heckman, T.M., Lehnert, M.D., Strickland, D.K., Armus, L. 2000, ApJS, 129, 493

Heckman, T.M., & Leitherer, C. 1997, AJ, 114, 69

Heckman, T. M., Armus, L., & Miley, G. K. 1990, ApJS, 74, 833

Kunth, D., Mas-Hesse, J. M., Terlevich, E., Terlevich, R., Lequeux, J., & Fall, S. M. 1998, A&A, 334, 11

Leitherer, C., Leao, J.R.S., Heckman, T.M., Lennon, D.J., Pettini, M., Robert, C. 2001, ApJ 550, 724

Leitherer, C., et al. 1999, ApJS, 123, 3

Lejeune, T., Cuisinier, F., Buser, R. 1997, A&AS, 125, 229

Lejeune, T., Buser, R., Cuisinier, F. 1996, GISSEL96 CD-ROM

Lin, H., Kirshner, R.P., Schechtman, S.A., Landy, S.D., Oemler, A., Tucker, D.L., Schechter, P.L. 1996, ApJ, 464, 60

Liu, M.C., Charlot, S., & Graham, J.R. 2000, ApJ, 543, 644

Lowenthal, J. D., Koo, D., Guzman, R., Gallego, J., Phillips, A., Faber, S.M., Vogt, N.P., Illingworth, G., & Gronwall, C. 1997, ApJ, 481, 673

Madau, P. Ferguson, H. C., Dickinson, M. E., Giavalisco, M., Steidel, C. C., & Fruchter, A. 1996, MNRAS, 283, 1388

Madau, P. 1995, ApJ, 444, 18

Martin C. L. 1999, ApJ, 513, 156

Matthews, K. & Soifer, B.T. 1994, in Infrared Astronomy with Arrays: The Next Generation, ed. I. McLean (Dordrecht:Klewer), 239

Meurer, G.R., & Seibert 2001, in Starburst Galaxies Near and Far eds. D. Lutz & L. Tacconi (Springer) (astro-ph/0101479)

Meurer, G.R., Heckman, T.M., & Calzetti, D. 1999, ApJ, 521, 64

Mihos, J.C. & Hernquist, L. 1996, ApJ, 464, 641

Oke, J. B. et al. 1995, PASP 107, 3750

Papovich, C., Dickinson, M.E., & Ferguson, H.C. 2001, ApJ, accepted (astro-ph/0105087)

Persson, E., Murphy, D., Krzeminski, W., Roth, M., & Rieke, M. 1998, AJ, 116, 2475

Pettini, M., Shapley, A.E., Steidel, C.C., Cuby, J-G., Dickinson, M.E., Moorwood, A., Adelberger, K.L., Giavalisco, M. 2001, ApJ, 554, 981

Pettini, M., Steidel, C.C., Adelberger, K.L., Dickinson, M., & Giavalisco, M. 2000, ApJ, 528, 96

Pettini, M., Kellogg, M., Steidel, C.C., Dickinson, M.E., Adelberger, K.L., & Giavalisco, M. 1998, ApJ, 508, 539

Sawicki, M., & Yee, H. K. C. 1998, AJ, 115, 1329

Schechter, P. 1976, ApJ, 203, 297

Somerville, R.S., Primack, J.R., & Faber, S.M. 2001, MNRAS, 320, 504

Steidel, C.C., Adelberger, K.L., & Pettini, M. 2001, ApJ, 546, 665

Steidel, C.C., Adelberger, K.L., Giavalisco, M., Dickinson, M.E., & Pettini, M. 1999, ApJ, 519, 1

Steidel, C.C., Adelberger, K. L., Dickinson, M.E., Giavalisco, M., Pettini, M. & Kellogg, M. 1998, ApJ, 492, 428

Steidel, C.C., Giavalisco, M., Pettini, M., Dickinson, M.E., & Adelberger, K.L. 1996a, ApJL, 462, 17

Steidel, C.C., Giavalisco, Dickinson, M.E., & Adelberger, K.L. 1996b, AJ, 112, 352

Steidel, C.C., Pettini, M., & Hamilton, D. 1995, AJ, 110, 2519

Steidel, C.C., & Hamilton, D. 1993, AJ, 105, 2017

Steidel, C.C., & Hamilton, D. 1992, AJ, 104, 941

Tenorio-Tagle, G., Silich, S. A., Kunth, D., Terlevich, E., & Terlevich, R. 1999, MNRAS, 309, 332

Trentham, N., Kormendy, J., & Sanders, D. B. 1999, AJ, 117, 2152

Valdes, F. 1982, FOCAS User's Manual (NOAO, Tucson)

Williams, R. E., *et al.* 1996, AJ, 112, 1335

Table 1. NIRC Lyman-Break Galaxy Fields

Field Name	Field Center (J2000)	Area ($\mathcal{R}$) (arc min)^2	Area (K_s) (arc min)^2	# Galaxies (K_s)	Area (J) (arc min)^2	# Galaxies (J)
CDFa	00 53 23.7 +12 34 00	78.42	1.72	7	1.18	5
Q0201	02 03 51.6 +11 34 09	75.77	1.35	3	1.21	3
Q0256	02 59 08.6 +00 11 41	72.28	1.17	6	...	...
B2 0902+34	09 05 30.2 +34 07 55	41.93	2.63	10	1.77	6
HDF	12 36 52.3 +62 12 59	75.32	2.96	14	2.29	10
WESTPHAL	14 17 14.5 +52 24 36	226.93	9.03	30	4.12	15
3C324	15 49 49.6 +21 29 07	44.29	1.85	6	0.56	2
SSA22a	22 17 34.2 +00 15 01	77.75	5.75	22	1.73	6
SSA22b	22 17 34.2 +00 06 18	77.60	0.59	2	...	...
DSF2237a	22 40 08.5 +11 52 34	83.38	0.64	1	0.61	1
DSF2237b	22 39 34.3 +11 51 44	81.62	2.43	17	1.71	15
TOTAL		935.29	30.12	118	15.18	63

Table 2. NIRC Observations and Integration Times

Pointing	Objects	Exposure (K_s) (sec)	Exposure (J) (sec)
CDFa-C8	C8,MD10	2400	···
CDFa-C1	C1,MD2	3780	1620
CDFa-C22	C22,M19,C19	3780	4620
Q0201-C6	C6,MMD21	3480	3780
Q0201-B13	B13	2700	2400
Q0256-M13	M13,C15,MD22	5220	···
Q0256-M17	M17,MD32,MD34	4260	···
B20902-C6	C6,M11,MD31	3780	3240
B20902-MD21	MD21	3240	3240
B20902-D11	D11,D12,MD32	1080	1620
B20902-MD11	MD11,MD14,MD18	2160	···
HDF-MM23	MM23,oC37,oMD49	6000	4680
HDF-DD15	DD15,MM28	3780	1620
HDF-CC24	CC24,oC38,oM5,MM25	2160	···
HDF-DD3	DD3,MM9,MM7	3120	3240
HDF-MM18	MM18,MM17	3240	3240
WESTPHAL-CC70	CC70,MM69,DD49	3240	3240
WESTPHAL-DD8	DD8,MMD14,MMD16,MM8	3240	3240
WESTPHAL-C11	C11	3240	···
WESTPHAL-CC13	CC13	2700	···
WESTPHAL-CC32	CC32,MMD53,MMD54	3240	···
WESTPHAL-CC79	CC79,MMD115	3000	···
WESTPHAL-MMD17	MMD17,MMD20,MM13	6420	2520
WESTPHAL-CC63	CC63,MMD91	3240	3180
WESTPHAL-MMD11	MMD11	1080	1620
WESTPHAL-CC1	CC1	3240	···
WESTPHAL-CC43	CC43,CC45,DD29	3180	3240
WESTPHAL-MMD109	MMD109,MMD112	1620	···
WESTPHAL-MMD113	MMD113,MMD11	1080	···
WESTPHAL-MMD23	MMD23,MM11	1620	···
3C324-C1	C1,C2,MD5	4200	···
3C324-D7	D7,C12	1080	1380
3C324-C3	C3	1620	···
SSA22a-D14	D14,MD42,MD40,M31	1860	···
SSA22a-D3	D3,MD3	7800	2700
SSA22a-MD46	MD46,MD50	3360	···
SSA22a-aug96D1	aug96D1,M8	3780	···
SSA22a-C16	C16,M13,M11	3240	···
SSA22a-C36	C36	3240	3240
SSA22a-C6	C6,M4,MD4	6960	4860
SSA22a-blob1	C11,C15,M10	2160	···
SSA22a-blob2	M14,MD14	2160	···
SSA22b-oct96D8	oct96D8,MD11	2880	···
DSF2237a-C2	C2	1860	2700
DSF2237b-M20	M20,C26,M19,MD56,MD57,M17,M18	7380	7920
DSF2237b-MD2	MD2,MD10	3240	···
DSF2237b-D28	D28,MD81,MD80,C43	3240	3240
DSF2237b-D3	D3,D4,MD9,C1	6480	4860

Table 3. Lyman-Break Galaxy Optical/Near-IR Photometry

Object Name	RA (J2000)	Dec (J2000)	$\mathcal{R}_{\rm AB}$	$(G-\mathcal{R})_{\rm AB}$	$(\mathcal{R}_{\rm AB}-J_{\rm Vega})$	$(\mathcal{R}_{\rm AB}-K_{s\rm Vega})$	z
CDFa-C22	00 53 09.42	+12 36 00.5	23.97	0.73 ± 0.08	0.90 ± 0.50	3.18 ± 0.23	3.046
CDFa-M19	00 53 11.04	+12 36 12.3	25.29	0.84 ± 0.15	0.93 ± 0.75	< 2.79	···
CDFa-C19	00 53 11.27	+12 35 39.9	24.63	0.81 ± 0.13	1.96 ± 0.30	3.79 ± 0.24	2.667
CDFa-C8	00 53 32.85	+12 32 11.4	23.72	0.96 ± 0.08	···	2.16 ± 0.40	3.071
CDFa-MD10	00 53 32.22	+12 31 56.3	25.42	0.48 ± 0.16	···	2.10 ± 0.60	···
CDFa-C1	00 53 34.74	+12 30 30.6	23.53	0.69 ± 0.06	1.29 ± 0.18	2.69 ± 0.21	3.110
CDFa-MD2	00 53 36.31	+12 30 31.2	23.88	0.75 ± 0.06	1.52 ± 0.23	2.96 ± 0.24	2.871
Q0201-C6	02 03 41.81	+11 34 41.5	23.92	0.62 ± 0.07	0.40 ± 0.55	2.39 ± 0.42	3.052
Q0201-MMD21	02 03 41.66	+11 34 44.8	24.67	0.51 ± 0.12	1.46 ± 0.47	2.72 ± 0.28	···
Q0201-B13	02 03 49.23	+11 36 10.8	23.34	0.03 ± 0.08	1.72 ± 0.13	2.81 ± 0.15	2.167
Q0256-C15	02 59 00.02	+00 11 38.6	24.23	0.69 ± 0.09	···	2.46 ± 0.46	3.385
Q0256-M13	02 58 58.83	+00 11 25.4	24.48	0.96 ± 0.12	···	2.89 ± 0.38	3.227
Q0256-M17	02 59 19.86	+00 12 32.4	24.04	1.10 ± 0.11	···	< 1.54	···
Q0256-MD22	02 59 00.79	+00 11 40.3	24.54	0.74 ± 0.11	···	2.30 ± 0.51	···
Q0256-MD32	02 59 18.11	+00 12 41.5	23.61	0.89 ± 0.07	···	2.61 ± 0.25	···
Q0256-MD34	02 59 20.21	+00 13 02.9	24.02	0.72 ± 0.08	···	3.88 ± 0.14	···
B20902-D11	09 05 23.01	+34 09 40.1	22.97	0.29 ± 0.06	0.89 ± 0.27	2.97 ± 0.13	2.837
B20902-D12	09 05 23.45	+34 09 45.0	25.46	-0.12 ± 0.10	< -0.23	< 2.96	···
B20902-MD32	09 05 26.24	+34 09 28.8	24.03	0.73 ± 0.10	1.25 ± 0.37	2.52 ± 0.41	2.860
B20902-C6	09 05 20.58	+34 09 07.7	24.13	0.45 ± 0.08	0.73 ± 0.54	2.39 ± 0.45	3.098
B20902-M11	09 05 19.58	+34 09 04.0	24.19	1.18 ± 0.16	1.36 ± 0.43	2.82 ± 0.32	3.300
B20902-MD31	09 05 20.27	+34 09 29.6	24.74	0.55 ± 0.12	···	3.77 ± 0.24	···
B20902-MD21	09 05 20.08	+34 07 19.7	24.18	1.06 ± 0.16	1.03 ± 0.49	2.51 ± 0.32	3.017
B20902-MD11	09 05 35.20	+34 06 25.2	24.27	1.04 ± 0.16	···	2.22 ± 0.48	3.392
B20902-MD14	09 05 36.58	+34 06 37.0	24.68	0.97 ± 0.14	···	3.44 ± 0.28	···
B20902-MD18	09 05 35.23	+34 06 53.2	24.51	0.41 ± 0.12	···	< 2.01	2.869
HDF-CC24	12 36 51.81	+62 15 16.3	24.33	0.76 ± 0.12	···	2.72 ± 0.40	3.333
HDF-DD3	12 36 47.60	+62 10 54.1	24.25	0.58 ± 0.09	1.45 ± 0.30	2.82 ± 0.32	2.942
HDF-DD15	12 36 48.97	+62 15 43.4	23.61	0.62 ± 0.07	0.36 ± 0.49	2.39 ± 0.37	3.135
HDF-MM7	12 36 47.75	+62 10 32.9	24.79	0.67 ± 0.17	1.02 ± 0.68	< 2.29	2.985
HDF-MM9	12 36 51.45	+62 10 42.7	24.73	0.78 ± 0.16	···	4.04 ± 0.19	2.972
HDF-MM17[a]	12 36 47.67	+62 12 56.8	24.46	1.00 ± 0.15	1.52 ± 0.45	3.54 ± 0.25	2.931
HDF-MM18[b]	12 36 44.01	+62 13 11.9	24.10	1.00 ± 0.11	1.63 ± 0.21	3.46 ± 0.16	2.929
HDF-MM23	12 37 02.64	+62 14 27.0	24.61	1.09 ± 0.16	1.58 ± 0.47	3.65 ± 0.24	3.214
HDF-MM25	12 36 50.72	+62 14 45.6	24.82	0.74 ± 0.17	···	2.45 ± 0.57	3.105
HDF-MM28	12 36 46.64	+62 15 18.1	25.04	0.70 ± 0.18	1.01 ± 0.70	2.89 ± 0.53	3.371
HDF-oC37	12 37 03.18	+62 14 52.1	25.25	0.40 ± 0.16	0.99 ± 0.75	2.14 ± 0.40	2.925
HDF-oC38	12 36 48.81	+62 15 03.6	24.97	0.67 ± 0.18	-0.81 ± 0.61	3.47 ± 0.32	3.114
HDF-oMD49	12 37 04.25	+62 14 47.2	24.78	-0.09 ± 0.11	2.20 ± 0.24	4.21 ± 0.19	2.212
HDF-oM5	12 36 50.46	+62 14 45.5	24.98	0.93 ± 0.16	···	2.93 ± 0.53	3.097
WESTPHAL-CC79	14 17 13.70	+52 36 16.5	24.28	0.87 ± 0.14	···	3.17 ± 0.40	3.061
WESTPHAL-MMD115	14 17 15.48	+52 36 12.6	23.97	0.65 ± 0.11	···	1.62 ± 0.41	3.203
WESTPHAL-MMD109	14 17 27.43	+52 35 49.0	23.94	0.84 ± 0.11	···	3.05 ± 0.20	2.715
WESTPHAL-MMD112	14 17 26.57	+52 35 59.2	25.34	0.63 ± 0.20	···	< 2.84	···
WESTPHAL-MMD113	14 18 24.85	+52 36 10.0	23.29	0.45 ± 0.08	···	2.71 ± 0.24	2.730
WESTPHAL-MMD111	14 18 23.71	+52 36 09.2	25.03	0.08 ± 0.15	···	3.22 ± 0.49	···
WESTPHAL-CC70	14 17 31.43	+52 34 25.6	23.75	0.55 ± 0.08	1.28 ± 0.24	2.41 ± 0.31	2.992
WESTPHAL-MM69	14 17 30.62	+52 34 17.2	25.24	0.83 ± 0.21	1.49 ± 0.57	3.24 ± 0.42	···
WESTPHAL-DD49	14 17 29.23	+52 34 31.5	23.50	0.17 ± 0.06	1.33 ± 0.18	3.35 ± 0.13	2.806
WESTPHAL-CC63	14 18 23.10	+52 32 46.9	23.50	1.14 ± 0.12	1.83 ± 0.14	2.60 ± 0.21	3.133
WESTPHAL-MMD91	14 18 22.93	+52 32 35.9	23.84	0.49 ± 0.09	1.11 ± 0.35	2.73 ± 0.32	2.738
WESTPHAL-CC43	14 17 25.47	+52 29 37.9	23.87	1.04 ± 0.15	1.24 ± 0.33	3.30 ± 0.16	3.081

Table 3—Continued

Object Name	RA (J2000)	Dec (J2000)	$\mathcal{R}_{\rm AB}$	$(G-\mathcal{R})_{\rm AB}$	$(\mathcal{R}_{\rm AB}-J_{\rm Vega})$	$(\mathcal{R}_{\rm AB}-K_{s\rm Vega})$	z
WESTPHAL-CC45	14 17 27.68	+52 29 50.4	24.83	0.67 ± 0.18	1.59 ± 0.53	3.03 ± 0.41	2.758
WESTPHAL-DD29	14 17 25.92	+52 29 32.1	24.82	0.32 ± 0.13	1.60 ± 0.42	3.86 ± 0.24	3.240
WESTPHAL-CC32	14 18 14.45	+52 28 04.7	24.17	0.55 ± 0.11	···	2.40 ± 0.46	3.197
WESTPHAL-MMD53	14 18 12.63	+52 28 06.6	25.22	0.36 ± 0.16	···	3.98 ± 0.25	···
WESTPHAL-MMD54	14 18 14.46	+52 28 16.0	24.64	0.45 ± 0.13	···	2.98 ± 0.45	3.017
WESTPHAL-MMD23	14 17 21.95	+52 23 39.1	24.22	0.82 ± 0.14	···	2.81 ± 0.32	2.857
WESTPHAL-MM11	14 17 22.02	+52 23 27.0	25.24	0.61 ± 0.20	···	3.59 ± 0.32	···
WESTPHAL-CC13	14 18 02.47	+52 24 36.5	23.64	1.06 ± 0.14	···	2.42 ± 0.37	3.396
WESTPHAL-MMD17	14 18 09.56	+52 23 32.1	24.56	0.91 ± 0.17	2.04 ± 0.24	2.49 ± 0.55	2.869
WESTPHAL-MMD20	14 18 09.63	+52 23 37.2	24.59	0.63 ± 0.16	1.87 ± 0.30	2.15 ± 0.50	2.799
WESTPHAL-MM13	14 18 12.15	+52 23 30.4	25.40	0.69 ± 0.21	···	3.96 ± 0.27	2.856
WESTPHAL-west3-C11	14 18 17.63	+52 23 46.2	24.25	1.22 ± 0.16	···	2.69 ± 0.40	3.137
WESTPHAL-DD8	14 18 25.44	+52 23 22.4	24.47	0.68 ± 0.14	1.09 ± 0.56	2.77 ± 0.46	2.841
WESTPHAL-MMD14	14 18 24.72	+52 23 19.8	24.92	0.82 ± 0.20	1.62 ± 0.42	3.08 ± 0.41	···
WESTPHAL-MMD16	14 18 23.61	+52 23 28.8	24.73	0.92 ± 0.17	1.88 ± 0.30	4.06 ± 0.19	···
WESTPHAL-MM8	14 18 23.92	+52 23 07.7	24.13	1.04 ± 0.16	1.74 ± 0.21	3.25 ± 0.19	2.829
WESTPHAL-MMD11	14 18 09.73	+52 22 01.3	24.05	1.04 ± 0.16	2.67 ± 0.10	4.54 ± 0.11	2.979
WESTPHAL-CC1	14 18 21.98	+52 21 22.0	23.83	1.02 ± 0.15	···	2.78 ± 0.32	2.984
3C324-D7	15 49 52.96	+21 30 59.1	23.88	0.52 ± 0.08	0.78 ± 0.49	3.01 ± 0.20	···
3C324-C12	15 49 53.95	+21 31 06.7	25.04	0.54 ± 0.15	0.78 ± 0.71	3.34 ± 0.45	···
3C324-C3	15 49 47.10	+21 27 05.5	24.14	0.85 ± 0.13	···	2.57 ± 0.41	3.283
3C324-C1	15 49 54.27	+21 26 33.2	24.33	0.62 ± 0.14	···	3.12 ± 0.26	2.873
3C324-C2	15 49 53.98	+21 26 35.6	24.26	0.54 ± 0.10	···	3.19 ± 0.26	2.880
3C324-MD5	15 49 54.46	+21 26 34.6	25.48	-0.08 ± 0.24	···	3.93 ± 0.27	···
SSA22a-MD46	22 17 27.28	+00 18 09.9	23.30	0.42 ± 0.09	···	2.34 ± 0.29	3.090
SSA22a-MD50	22 17 26.83	+00 18 30.2	25.18	0.20 ± 0.17	···	3.18 ± 0.47	···
SSA22a-D14	22 17 35.29	+00 17 24.1	24.32	0.19 ± 0.14	···	2.07 ± 0.46	3.018
SSA22a-MD42	22 17 35.83	+00 17 19.8	25.33	0.06 ± 0.17	···	4.04 ± 0.25	···
SSA22a-MD40	22 17 35.96	+00 17 08.3	24.89	0.70 ± 0.19	···	2.21 ± 0.57	3.015
SSA22a-M31	22 17 36.87	+00 17 12.4	25.41	0.42 ± 0.18	···	3.22 ± 0.44	···
SSA22a-C36	22 17 46.10	+00 16 43.1	24.06	0.78 ± 0.13	1.23 ± 0.37	3.07 ± 0.23	3.065
SSA22a-C16	22 17 31.96	+00 13 16.1	23.64	0.98 ± 0.10	···	2.86 ± 0.20	3.061
SSA22a-M13	22 17 31.46	+00 12 55.2	25.46	0.74 ± 0.24	···	< 2.96	···
SSA22a-M11	22 17 31.77	+00 12 51.3	25.35	0.50 ± 0.18	···	< 2.85	···
SSA22a-M14	22 17 39.05	+00 13 30.1	25.47	0.75 ± 0.24	···	2.99 ± 0.62	3.091
SSA22a-MD14	22 17 37.93	+00 13 44.2	24.14	0.86 ± 0.14	···	1.96 ± 0.43	···
SSA22a-C11	22 17 25.68	+00 12 35.3	24.20	0.47 ± 0.12	···	2.82 ± 0.32	3.108
SSA22a-C15	22 17 26.12	+00 12 55.3	25.19	0.55 ± 0.19	···	3.50 ± 0.32	3.092
SSA22a-M10	22 17 26.79	+00 12 21.1	24.45	1.03 ± 0.18	···	2.32 ± 0.51	3.098
SSA22a-aug96D1	22 17 24.00	+00 12 02.8	23.60	0.32 ± 0.09	···	2.79 ± 0.12	2.202
SSA22a-M8	22 17 25.11	+00 11 56.8	24.72	0.89 ± 0.19	···	3.64 ± 0.24	···
SSA22a-D3	22 17 32.42	+00 11 33.0	23.37	0.97 ± 0.10	-0.60 ± 0.40	2.24 ± 0.32	3.086
SSA22a-MD3	22 17 31.89	+00 11 38.3	24.60	0.15 ± 0.13	1.40 ± 0.47	2.17 ± 0.50	2.483
SSA22a-C6	22 17 40.93	+00 11 26.0	23.44	0.79 ± 0.09	0.36 ± 0.44	2.01 ± 0.37	3.099
SSA22a-M4	22 17 40.92	+00 11 27.9	24.83	0.76 ± 0.19	0.93 ± 0.68	2.68 ± 0.56	3.091
SSA22a-MD4	22 17 39.95	+00 11 39.6	24.25	0.24 ± 0.12	1.03 ± 0.49	2.92 ± 0.32	2.611
SSA22b-MD11	22 17 23.07	+00 03 42.2	25.23	0.37 ± 0.15	···	3.14 ± 0.47	···
SSA22b-oct96D8	22 17 23.52	+00 03 57.3	23.53	0.77 ± 0.08	···	2.87 ± 0.18	3.323
DSF2237a-C2	22 40 08.30	+11 49 04.9	23.55	1.13 ± 0.10	1.47 ± 0.20	3.02 ± 0.17	3.318
DSF2237b-D28	22 39 20.25	+11 55 11.4	24.46	0.32 ± 0.08	1.34 ± 0.49	2.42 ± 0.52	2.934
DSF2237b-MD81	22 39 21.72	+11 55 10.5	24.16	0.31 ± 0.07	2.23 ± 0.17	4.27 ± 0.14	2.819
DSF2237b-MD80	22 39 22.23	+11 55 08.3	25.37	0.94 ± 0.20	1.16 ± 0.77	3.08 ± 0.37	···

Table 3—Continued

Object Name	RA (J2000)	Dec (J2000)	$\mathcal{R}_{\rm AB}$	$(G-\mathcal{R})_{\rm AB}$	$(\mathcal{R}_{\rm AB}-J_{\rm Vega})$	$(\mathcal{R}_{\rm AB}-K_{s\rm Vega})$	z
DSF2237b-C43	22 39 21.57	+11 54 44.9	24.35	0.70 ± 0.11	1.73 ± 0.34	< 1.85	2.885
DSF2237b-M20	22 39 38.88	+11 52 22.1	24.20	1.12 ± 0.13	1.33 ± 0.43	2.96 ± 0.20	3.156
DSF2237b-C26	22 39 38.02	+11 52 11.4	24.73	0.57 ± 0.12	1.03 ± 0.60	2.64 ± 0.50	3.251
DSF2237b-M19	22 39 38.04	+11 52 20.6	24.80	0.96 ± 0.18	1.47 ± 0.53	2.79 ± 0.56	3.259
DSF2237b-MD56	22 39 39.00	+11 52 19.2	25.43	0.65 ± 0.17	1.81 ± 0.41	3.10 ± 0.39	···
DSF2237b-MD57	22 39 39.92	+11 52 27.2	24.56	0.73 ± 0.13	0.95 ± 0.66	2.51 ± 0.55	3.331
DSF2237b-M17	22 39 39.87	+11 52 06.5	24.67	1.03 ± 0.18	1.06 ± 0.60	2.53 ± 0.55	3.020
DSF2237b-M18	22 39 40.16	+11 52 16.0	25.33	0.76 ± 0.16	0.78 ± 0.72	< 2.83	···
DSF2237b-MD2	22 39 29.89	+11 47 12.5	24.17	0.90 ± 0.12	···	2.28 ± 0.36	2.505
DSF2237b-MD10	22 39 30.58	+11 47 34.3	25.04	1.01 ± 0.19	···	2.87 ± 0.53	3.115
DSF2237b-D3	22 39 18.91	+11 47 40.4	24.19	0.51 ± 0.09	1.07 ± 0.49	2.02 ± 0.37	2.931
DSF2237b-D4	22 39 18.75	+11 47 40.5	24.35	0.17 ± 0.10	1.13 ± 0.56	2.20 ± 0.29	2.935
DSF2237b-MD9	22 39 17.68	+11 47 39.2	24.97	0.45 ± 0.07	0.31 ± 0.56	< 2.47	···
DSF2237b-C1	22 39 16.90	+11 47 47.5	24.99	0.37 ± 0.12	1.60 ± 0.51	2.95 ± 0.32	3.064

[a]This galaxy is in the central Hubble Deep Field (HDF), and is referred to as "4-52.0" in Williams *et al.* (1996) and "HDF/NIC 813/814" in Papovich *et al.* (2001).

[b] This galaxy is in the central HDF, and is referred to as "1-54.0" in Williams *et al.* (1996) and "HDF/NIC 522" in Papovich *et al.* (2001).

Table 4. Lyman-Break Galaxy Constant SFR Best-Fit Parameters

Object Name	$E(B-V)$	t_{sf} (Myr)	SFR ($h^{-2}M_{\odot}\mathrm{yr}^{-1}$)	$\log(m_{star}(h^{-2}M_{\odot}))$
CDFa-C1	0.08	905	35	10.5
CDFa-C19	0.38	203	156	10.5
CDFa-C22	0.13	1278	36	10.7
CDFa-C8[b]	0.26	10	275	9.4
CDFa-MD2	0.20	321	65	10.3
Q0201-C6	0.08	321	23	9.9
Q0201-B13	0.04	2500	14	10.5
Q0256-C15	0.02	905	12	10.0
Q0256-M13	0.15	404	32	10.1
B20902-C6	0.05	509	15	9.9
B20902-D11	0.09	1278	53	10.8
B20902-M11	0.21	143	80	10.1
B20902-MD11	0.17	30	69	9.3
B20902-MD21	0.23	35	99	9.5
B20902-MD32	0.24	35	110	9.6
HDF-CC24	0.08	806	19	10.2
HDF-DD15	0.10	227	42	10.0
HDF-DD3	0.12	719	23	10.2
HDF-MM17	0.30	321	104	10.5
HDF-MM18	0.32	203	179	10.5
HDF-MM23[a]	0.18	2000	36	10.8
HDF-MM25	0.09	360	11	9.6
HDF-MM28[a]	0.05	1800	8	10.1
HDF-MM9[a]	0.24	2100	49	11.0
HDF-oC37	0.11	114	9	9.0
HDF-oC38[a]	0.15	2000	18	10.5
HDF-oM5	0.29	55	81	9.6
WESTPHAL-CC1[b]	0.34	10	516	9.7
WESTPHAL-CC13	0.11	227	51	10.1
WESTPHAL-CC32	0.06	454	16	9.9
WESTPHAL-CC43	0.23	454	104	10.6
WESTPHAL-CC45	0.23	255	33	9.9
WESTPHAL-CC70	0.10	321	32	10.0
WESTPHAL-CC79	0.18	641	45	10.4
WESTPHAL-DD49	0.17	1139	68	10.9
WESTPHAL-CC63[b]	0.36	10	942	10.0
WESTPHAL-DD8	0.32	15	175	9.4
WESTPHAL-MM8	0.37	40	324	10.1
WESTPHAL-MMD109[b]	0.41	10	662	9.8
WESTPHAL-MMD113	0.23	81	156	10.1
WESTPHAL-MMD115[b]	0.13	10	71	8.9
WESTPHAL-MMD23	0.32	20	219	9.6
WESTPHAL-MMD54	0.10	1278	14	10.3
WESTPHAL-MMD91	0.16	286	42	10.1
WESTPHAL-west3-C11	0.29	15	223	9.5
3C324-C1	0.12	1434	20	10.4
3C324-C2	0.12	1700	22	10.6
3C324-C3	0.07	641	19	10.1
SSA22a-aug96D1	0.17	321	37	10.1
SSA22a-C11	0.08	1139	18	10.3
SSA22a-C15[a]	0.12	2000	11	10.3
SSA22a-C16	0.21	181	109	10.3

Table 4—Continued

Object Name	$E(B-V)$	t_{sf} (Myr)	SFR ($h^{-2}M_{\odot}\mathrm{yr}^{-1}$)	$\log(m_{star}(h^{-2}M_{\odot}))$
SSA22a-C36	0.17	571	48	10.4
SSA22a-C6[b]	0.20	10	204	9.3
SSA22a-D14	-0.01	571	6	9.6
SSA22a-M10[b]	0.30	10	212	9.3
SSA22a-M14	0.15	571	12	9.8
SSA22a-M4	0.13	321	17	9.7
SSA22a-D3[b]	0.29	10	540	9.7
SSA22a-MD3	0.24	15	54	8.9
SSA22a-MD4	0.14	641	21	10.1
SSA22a-MD40	0.21	20	45	9.0
SSA22a-MD46	0.01	806	22	10.2
SSA22b-oct96D8[a]	0.06	1900	32	10.8
DSF2237a-C2	0.15	719	76	10.7
DSF2237b-C1[a]	0.05	2100	6	10.1
DSF2237b-C26	0.05	1139	9	10.0
DSF2237b-D28	0.06	719	10	9.9
DSF2237b-D3	0.16	30	46	9.1
DSF2237b-D4	-0.04	1278	5	9.8
DSF2237b-M19	0.20	161	40	9.8
DSF2237b-M20	0.21	227	69	10.2
DSF2237b-MD10	0.29	35	88	9.4
DSF2237b-MD2[b]	0.39	10	377	9.6

[a]The best-fit ages for marked galaxies, when unconstrained, were older than the age of the universe at the galaxy's redshift. The best-fit quantities listed for these galaxies reflect the constraint that the age of a galaxy should not be older than the age of the universe. Such a constraint still provides statistically acceptable fits for marked galaxies.

[b]The best-fit ages for the marked galaxies, when unconstrained, were younger than 10 Myr. Such young ages are physically implausible, and therefore we restricted the best-fit ages to be at least 10 Myr. The best-fit quantities listed for marked galaxies reflect this constraint, and provide statistically acceptable fits for marked galaxies.

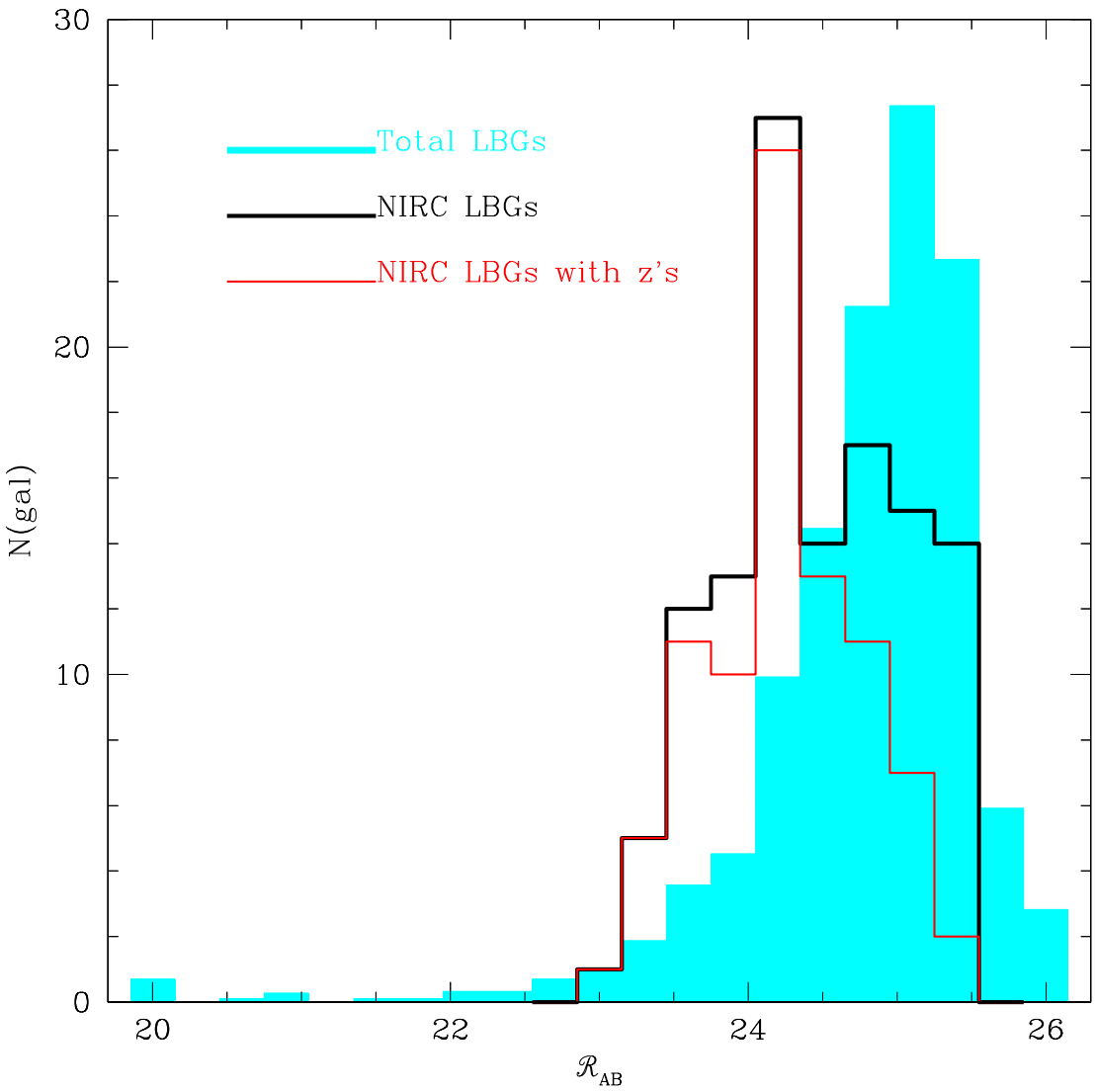

Fig. 1a.— The distribution of $\mathcal{R}$ magnitudes for the NIRC LBG sample, relative to that of the LBG survey as a whole. The LBG total sample histogram has been normalized to the number of galaxies contained in the NIRC LBG subsample, for the purpose of comparison. Also indicated is the $\mathcal{R}$ distribution for the NIRC LBGs with measured redshifts, which comprise a slightly brighter sample than the NIRC LBG sample as a whole.

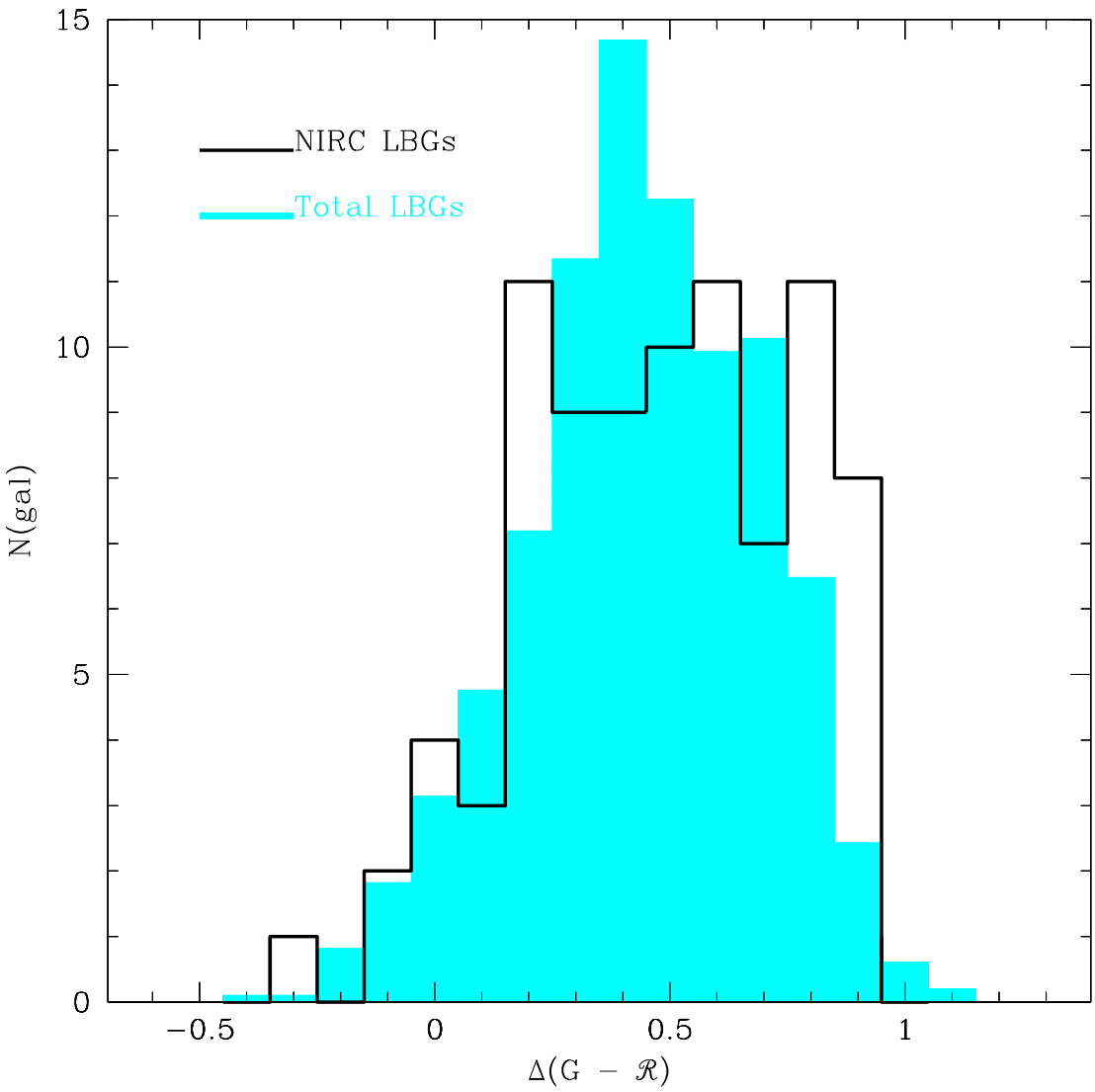

Fig. 1b.— The distribution of $(G-\mathcal{R})_0$, the IGM-absorption-corrected $G-\mathcal{R}$ color, for galaxies in the NIRC LBG sample with redshifts, relative to that of the LBG spectroscopic sample as a whole. The total LBG histogram has been normalized to the number of objects in the NIRC LBG histogram. This figure shows that the NIRC LBG spectroscopic sample contains an excess of highly reddened galaxies, relative to the total LBG spectroscopic sample.

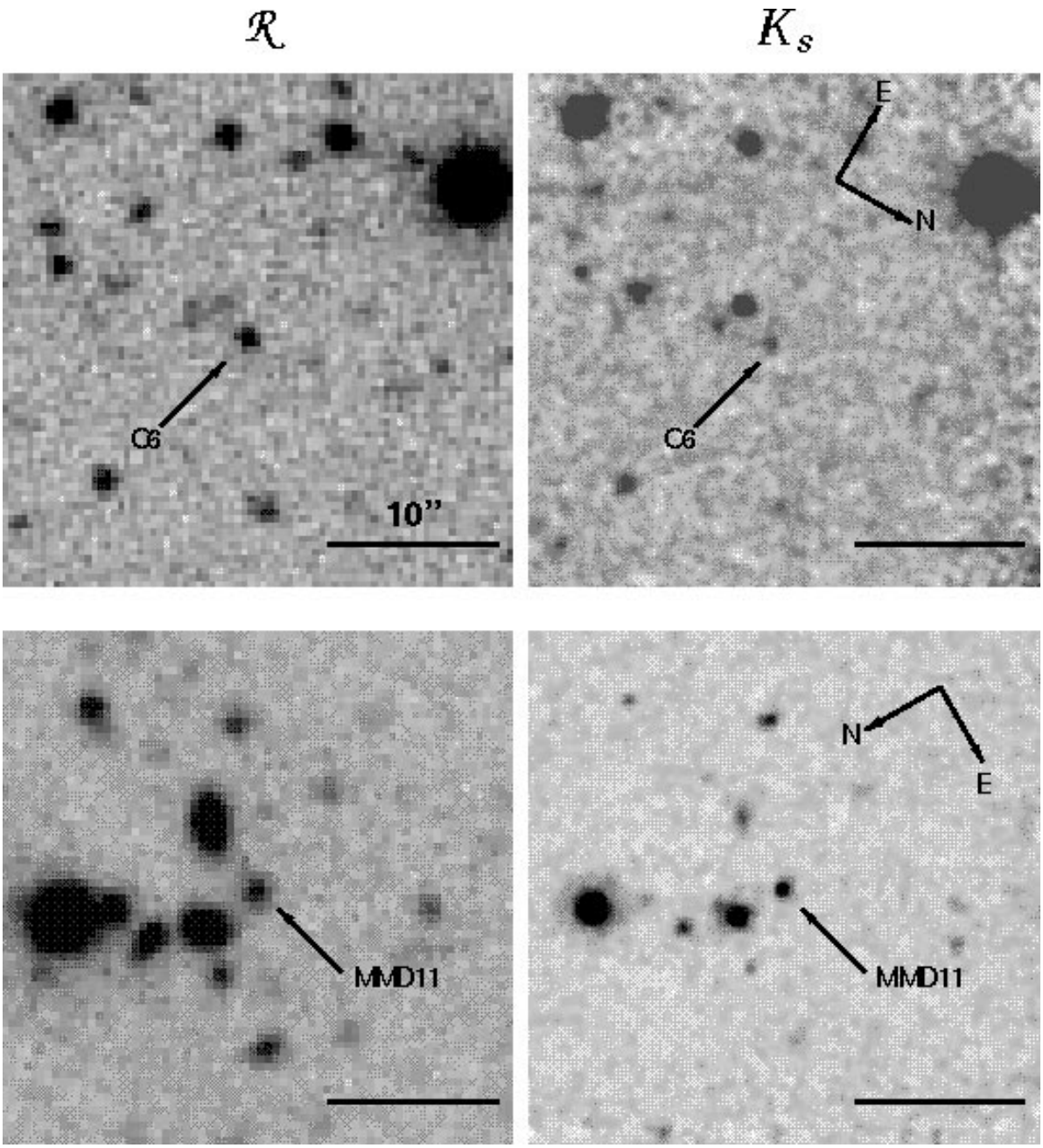

Fig. 2.— $\mathcal{R}$ and K_s images for two objects in the NIRC LBG sample. A bar indicating 10” is in the lower right-hand corner of each image. The N-E orientation of the $\mathcal{R}$ and K_s images for each object is indicated in the K_s images. NIRC orientations were chosen to locate a guide star on the guide camera, as well as to maximize the number of galaxies per pointing. Top: B20902-C6 has $\mathcal{R} = 24.13$ and $\mathcal{R} - K_s = 2.39$ which puts it in the bluer half of the sample of $\mathcal{R} - K_s$ measurements, with a fairly typical signal-to-noise ratio. Bottom: Westphal-MMD11 has $\mathcal{R} = 24.05$ and $\mathcal{R} - K_s = 4.54$, which gives it the reddest and highest signal-to-noise $\mathcal{R} - K_s$ measurement in the NIRC LBG sample.

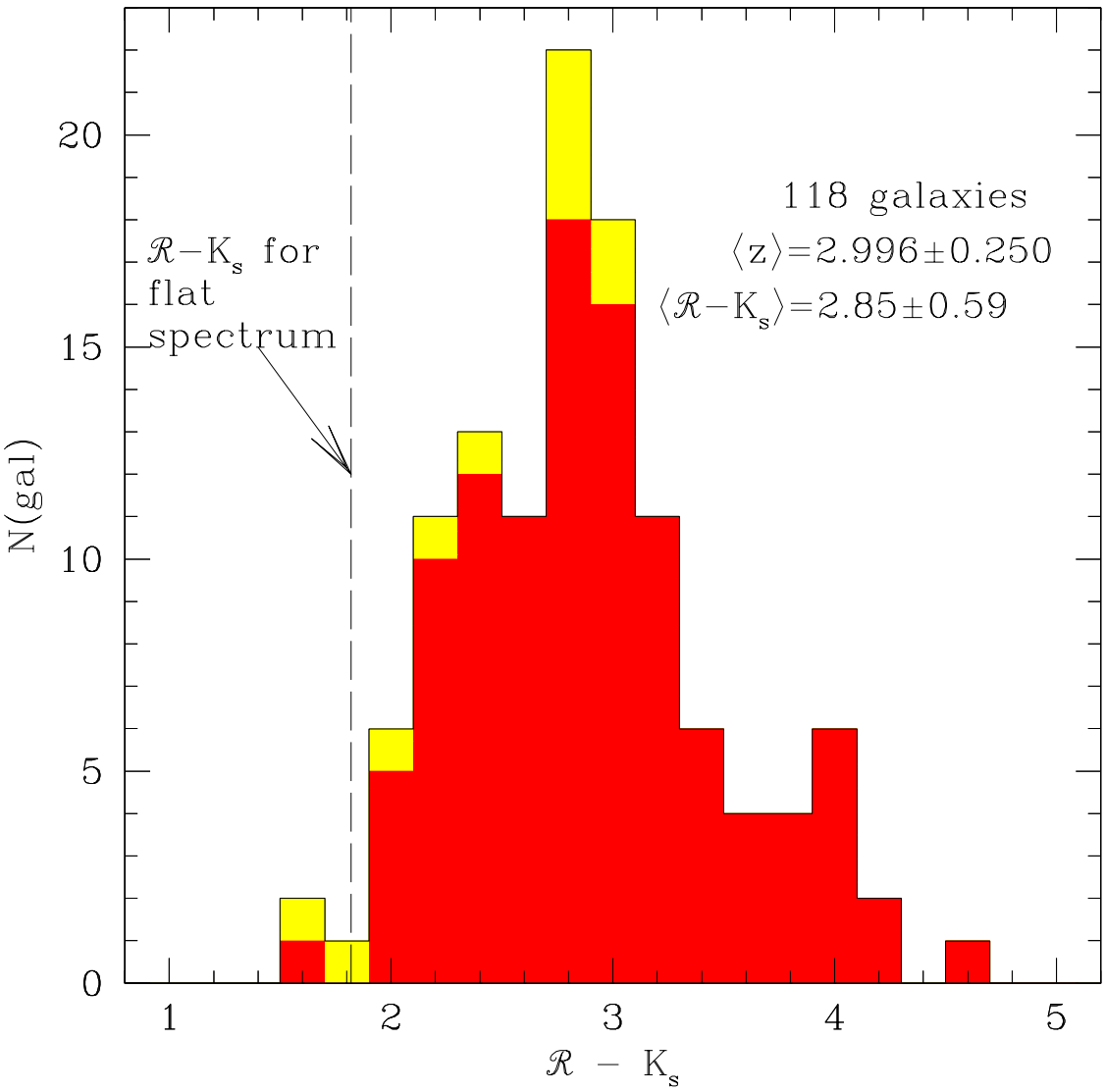

Fig. 3.— The distribution of observed $\mathcal{R} - K_s$ colors for the NIRC LBG sample. Of the 118 galaxies, 107 have $\mathcal{R} - K_s$ detections, and 11 have upper limits, corresponding to the typical K_s detection limit of $K_s = 22.5$. Detections are indicated in the red (dark) shaded histogram, while upper limits are in the yellow (light) shaded bins. A dashed line at $\mathcal{R} - K_s = 1.82$ marks the color for a flat spectrum in F_ν. The average color in the sample is $< \mathcal{R} - K_s >= 2.85$. 81 of 118 galaxies in the NIRC LBG sample have measured redshifts, with $< z >= 2.996$.

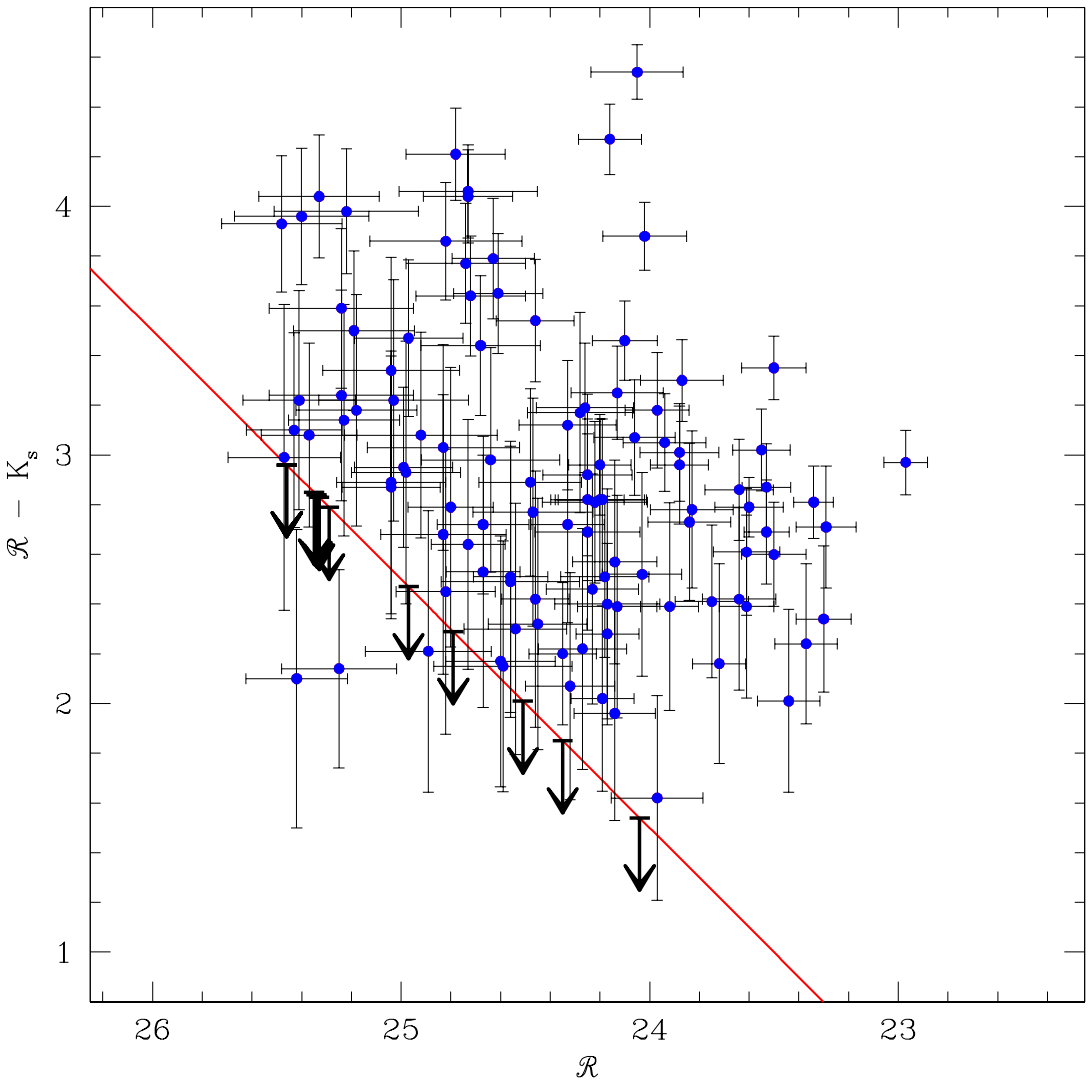

Fig. 4.— $\mathcal{R} - K_s$ vs. $\mathcal{R}$. Dots indicate $\mathcal{R} - K_s$ detections, while down-arrows indicate upper limits. The diagonal line traces the typical sample detection limit of $K_s = 22.5$. There are three points below this detection line, representing galaxies in K_s images with more sensitive detection limits than the typical one.

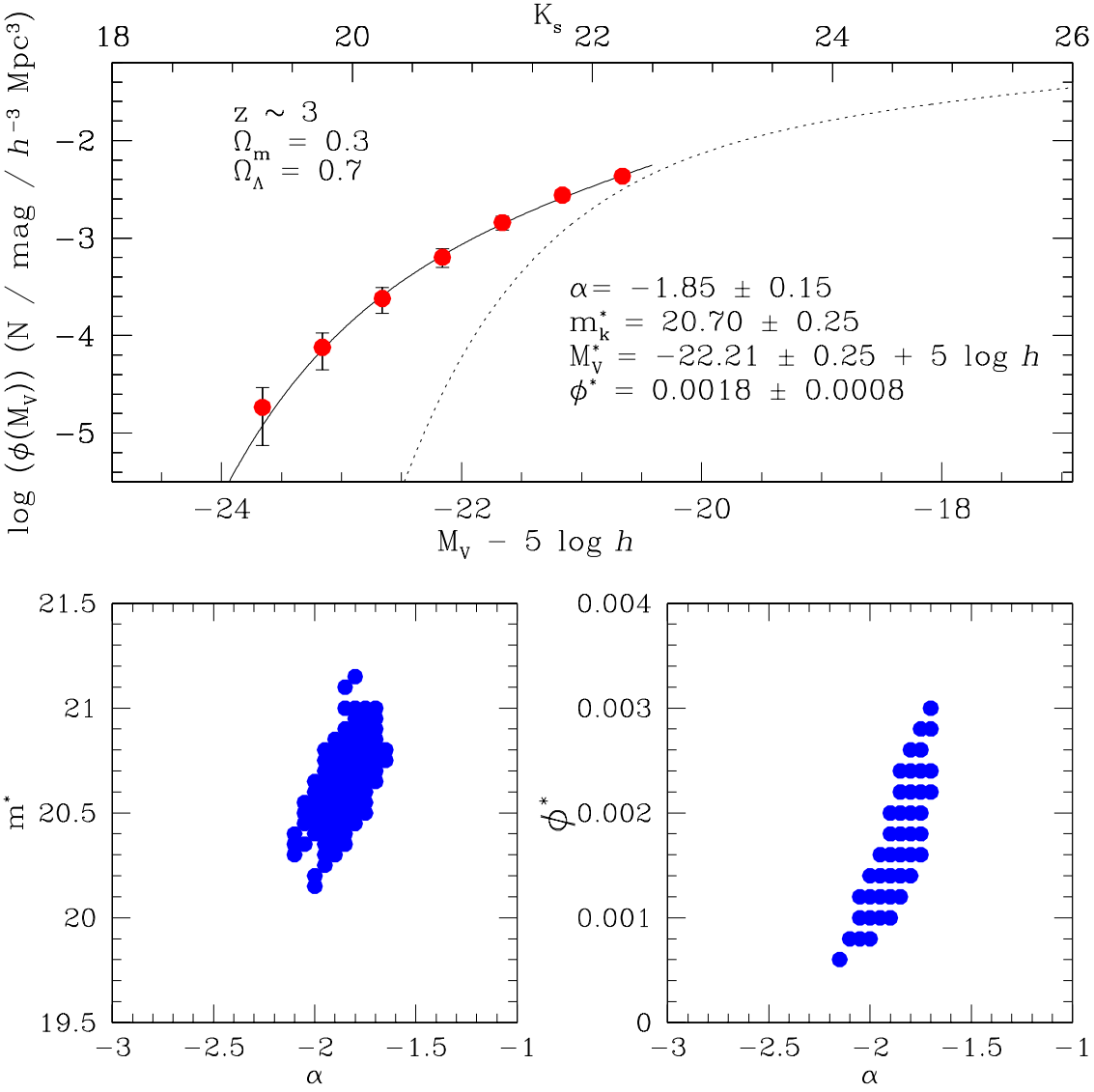

Fig. 5.— Top: The rest-frame optical luminosity function of LBGs. The points and solid line indicate the magnitude range used for the Schechter function fit. The error bars on the points include the photometric uncertainties on the $\mathcal{R}$ and $\mathcal{R} - K_s$ measurements. The lower x-axis indicates the range in optical absolute magnitude, M_V, spanned by the K_s luminosity function (assuming $h = 1$). The dotted line indicates the locally determined 2dFGRS b_j luminosity function, offset by a color of $b_j - V = 0.5$ magnitudes (for comparison at the same rest wavelength as the LBG optical luminosity function). Bottom: The 68.3% confidence intervals for the best-fit Schechter function parameters. The covariance between the best-fit parameters is indicated by the confidence regions. As the faint-end slope (α) becomes steeper, the characteristic luminosity (m^*) increases, and the overall normalization (ϕ^*) decreases.

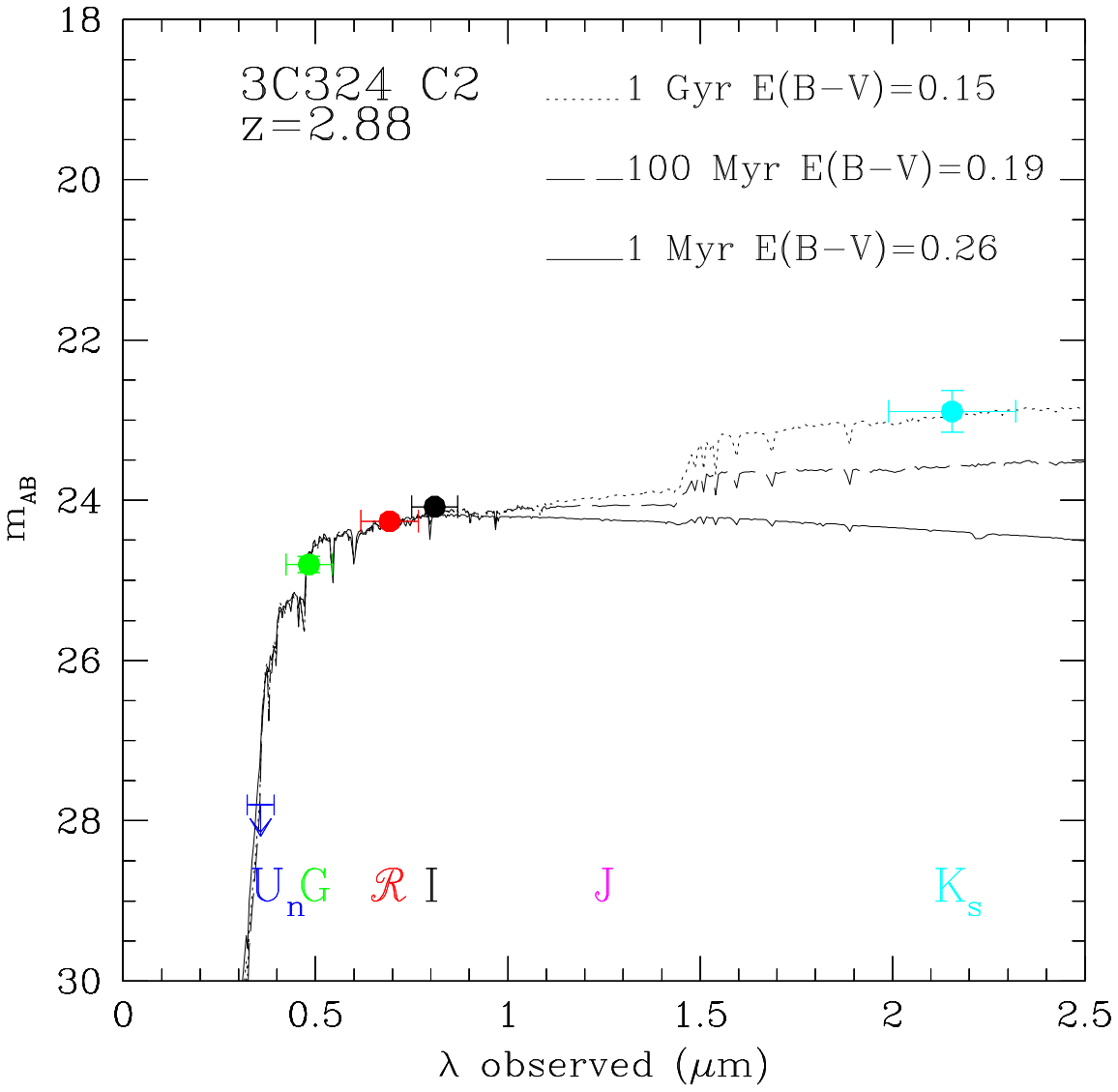

Fig. 6.— The Age-Dust Degeneracy. The points indicate the observed spectral energy distribution of 3C324-C2, a LBG at $z = 2.880$. Shown with the points are BC96 constant star-formation models of different ages, modified by the amount of dust extinction required to reproduce the observed $G - \mathcal{R}$ color. The dotted line is a 1 Gyr model with $E(B-V) = 0.149$; the dashed line is a 100 Myr model with $E(B-V) = 0.186$; and the solid line is a 1 Myr model with $E(B-V) = 0.263$. All of these models describe the observed optical photometry equally well. However, only the 1 Gyr model successfully describes the the observed $\mathcal{R} - K_s$ color.

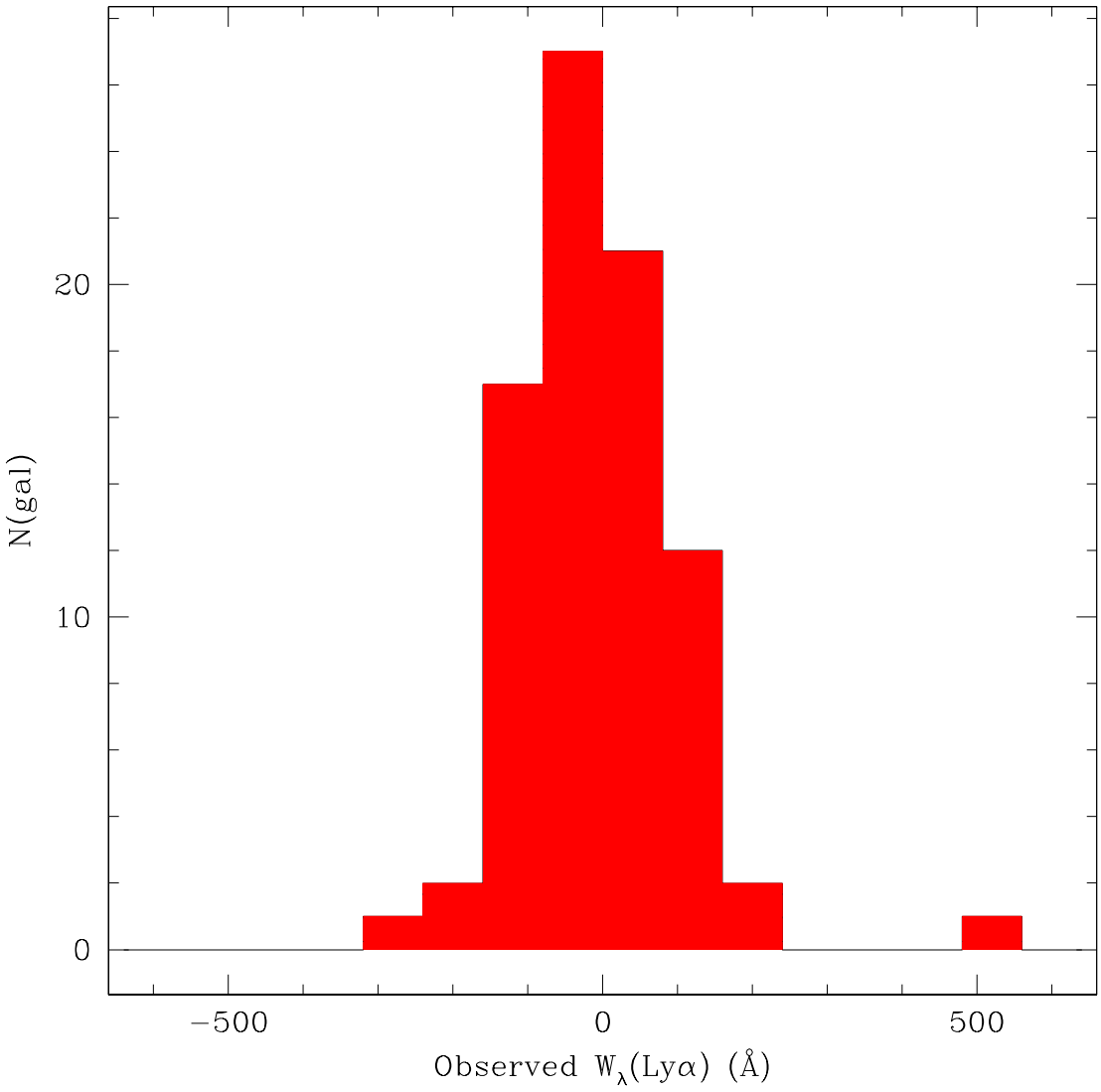

Fig. 7.— The distribution of observed Lyman α equivalent widths. The median equivalent width is 0. However, there are extreme cases of observed equivalent widths greater than 300 Å in either emission or absorption. If unaccounted for, such large equivalent widths would bias the modeling of the stellar population— especially the estimate of the dust extinction, but, to a certain extent, the age as well.

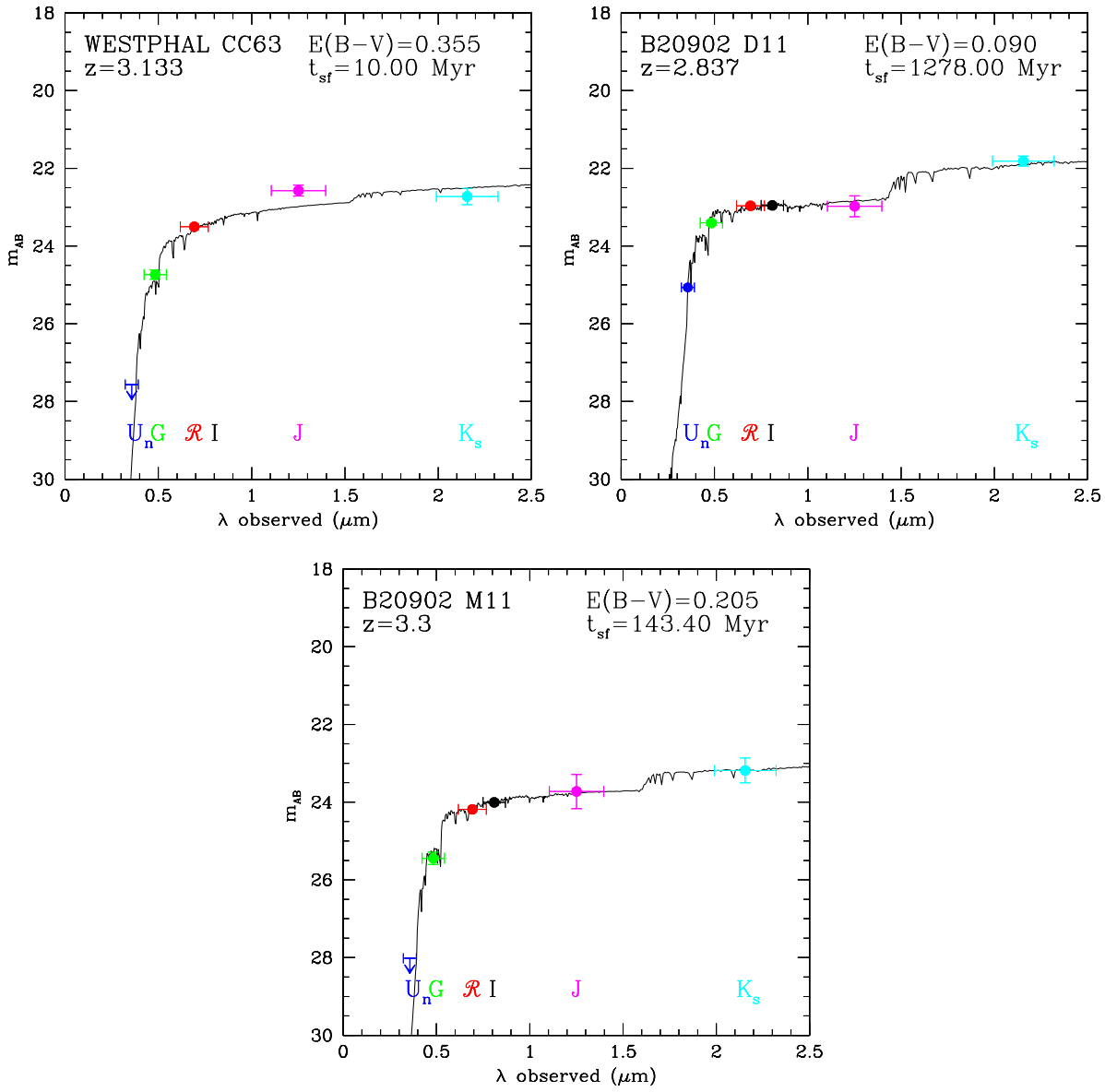

Fig. 8a.— The best-fit BC96 constant star-formation models for three galaxies in the NIRC LBG sample. These three examples span the range of properties in the sample. A young and dusty galaxy with very little evidence for a Balmer break, Westphal-CC63 is fit with a 10 Myr model with $E(B-V) = 0.355$ (while the formal best-fit age for CC63 is 4 Myr, we have restricted the best-fit age parameter space to values which are physically plausible (≥ 10 Myr)). At the other extreme, B20902-D11 has a best-fit age of 1.3 Gyr and $E(B-V) = 0.09$— much older with much less dust extinction. Intermediate between these two extremes, B20902-M11 has a best-fit age of 140 Myr and $E(B-V) = 0.205$. Each plot shows the galaxy's redshift and best-fit parameters. The photometric measurements are plotted as magnitudes, yet the error bars on the G, J, and K_s points refer to the uncertainties in the $G-\mathcal{R}$, $\mathcal{R}-J$ and $\mathcal{R}-K_s$ colors, respectively. The U and I measurements are plotted, even though they were not used to determine the best-fit models. There is no I data for the Westphal field, hence the lack of an I point for CC63.

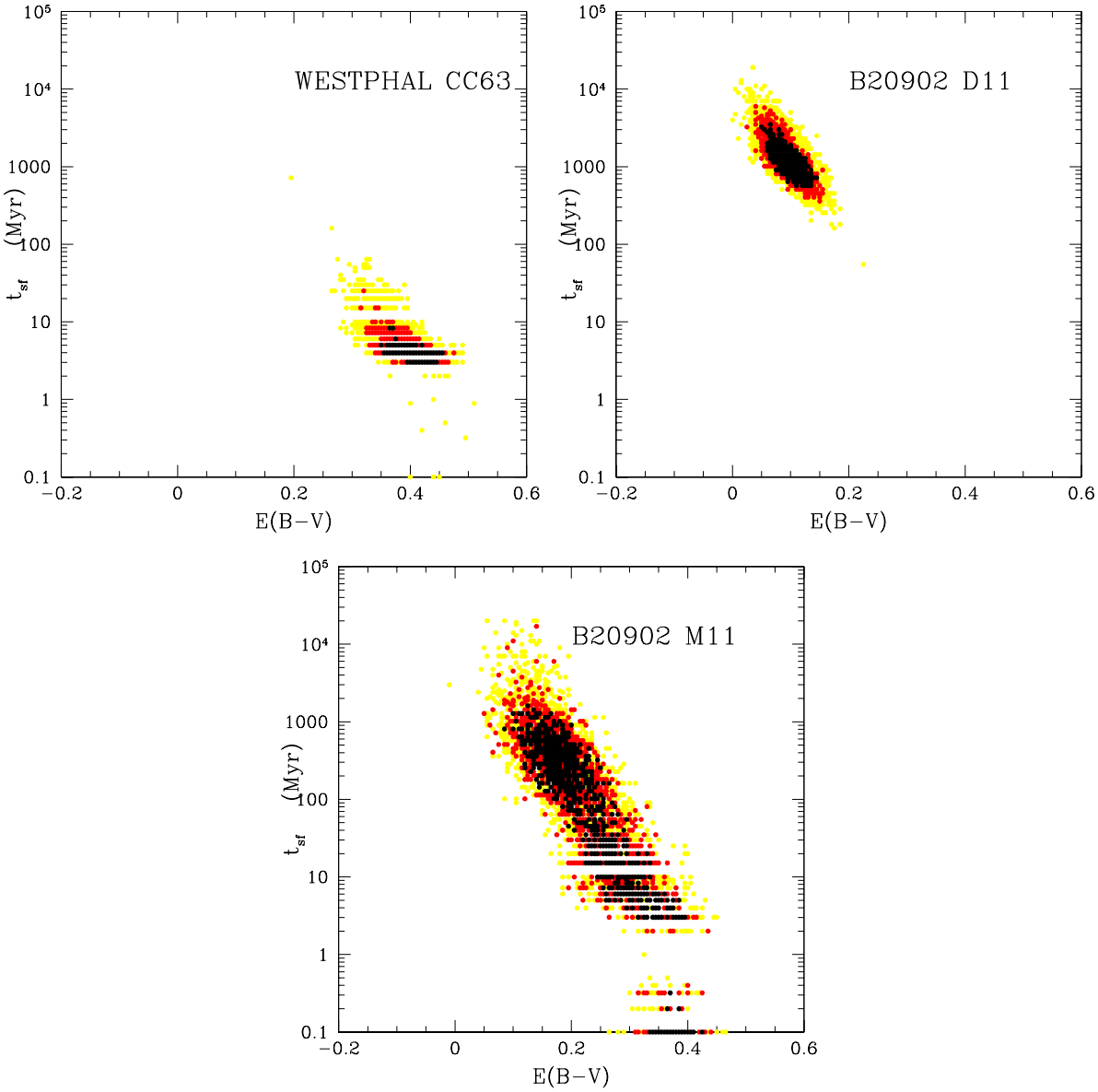

Fig. 8b.— Confidence intervals in the $E(B-V)-t_{sf}$ parameter space for the three galaxies featured in Figure 8a. Each confidence region is determined by generating a large sample of artificial colors for a galaxy (based on its measured colors and photometric uncertainties), and finding the best-fit $E(B-V)$ and t_{sf} for each set of artificial colors. The black region indicates the 68.3% confidence region; the red (dark grey) region indicates the 90% region, and the yellow (light grey) region indicates the remaining 10% of the realizations. Colors were assigned by probability density— i.e. the black points contain the highest density of realizations, while the red (dark grey) points contain intermediate densities, and the yellow (light grey) points have the lowest densities. Westphal-CC63 and B20902-D11 both have better determined optical-IR colors than B20902-M11, as demonstrated by the smaller confidence regions for those galaxies.

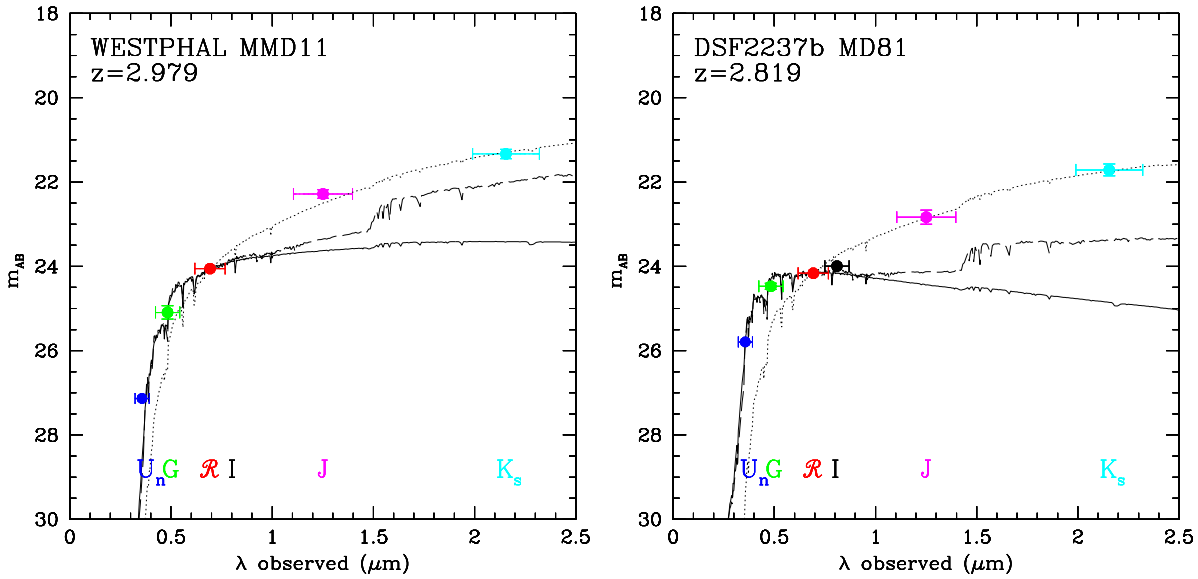

Fig. 9.— Anomalous Galaxies. Westphal-MMD11 and DSF2237b-MD81 are not described by any of the simple models which successfully fit the majority of galaxies in the NIRC LBG sample. For both galaxies, there is no combination of dust and age which simultaneously fits the $G-\mathcal{R}$, $\mathcal{R}-J$ and $\mathcal{R}-K_s$ colors. The $\mathcal{R}-J$ and $\mathcal{R}-K_s$ colors are simply too red to be fit by any of the simple models, including models with different star-formation histories. 1 Myr and 1 Gyr BC96 constant star-formation models were fit to the observed $G-\mathcal{R}$ color alone, excluding other colors. Solid lines represent 1 Myr BC96 constant star-formation models, and dashed lines indicate 1 Gyr models. Dotted lines indicate fits to the $\mathcal{R}-J$ and $\mathcal{R}-K_s$ colors, excluding the $G-\mathcal{R}$ color. For both galaxies, the $\mathcal{R}-J$ and $\mathcal{R}-K_s$ colors alone are fit by large amounts of extinction ($E(B-V) \geq 0.6$) and very young ages ($t_{sf} \leq 10\,\mathrm{Myr}$). The extrapolation of the dotted line to shorter wavelengths significantly underpredicts the flux observed in the U_n and G filters.

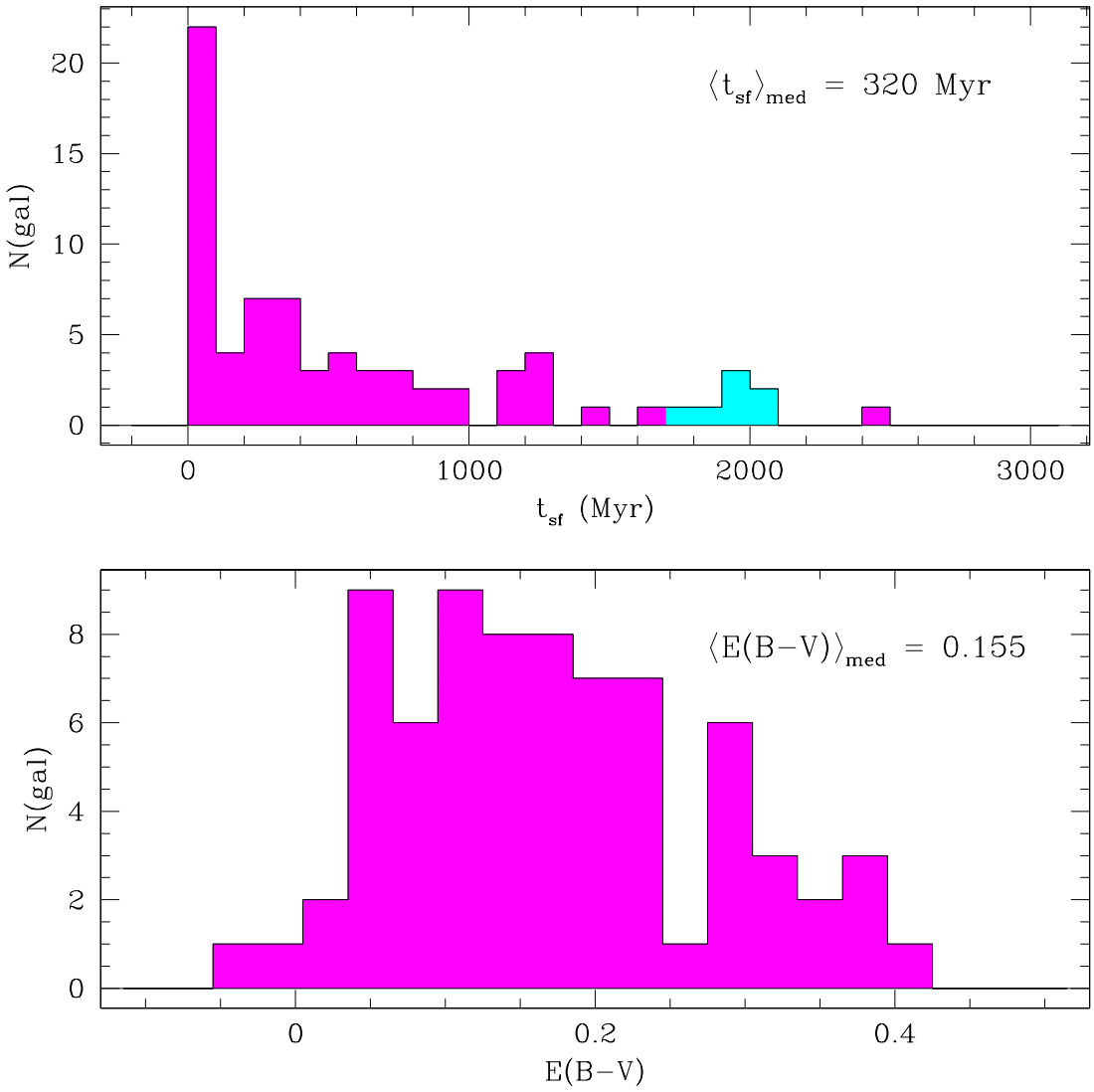

Fig. 10a.— Histograms of t_{sf} and $E(B-V)$ values derived from BC96 constant star-formation models. Top: The t_{sf} histogram. The cyan (light grey) bin indicates seven galaxies whose unconstrained best-fit t_{sf} values were older than the age of the universe at $z \sim 3$. Constraining each of these galaxies to have a best-fit t_{sf} younger than the age of the universe at its redshift (assuming an $\Omega_m = 0.3$, $\Omega_\Lambda = 0.7$, $h = 0.7$ cosmology) resulted in best-fit t_{sf} values of roughly 2 Gyr. The galaxy Q0201-B13 is at $z = 2.167$, so its best-fit t_{sf} of 2.5 Gyr (the oldest bin) does not pose a problem. Bottom: The $E(B-V)$ distribution, derived from both optical and near-IR photometry. This distribution probably over-represents the dustiest galaxies, relative to the LBG population as a whole, as shown by Figure 1b.

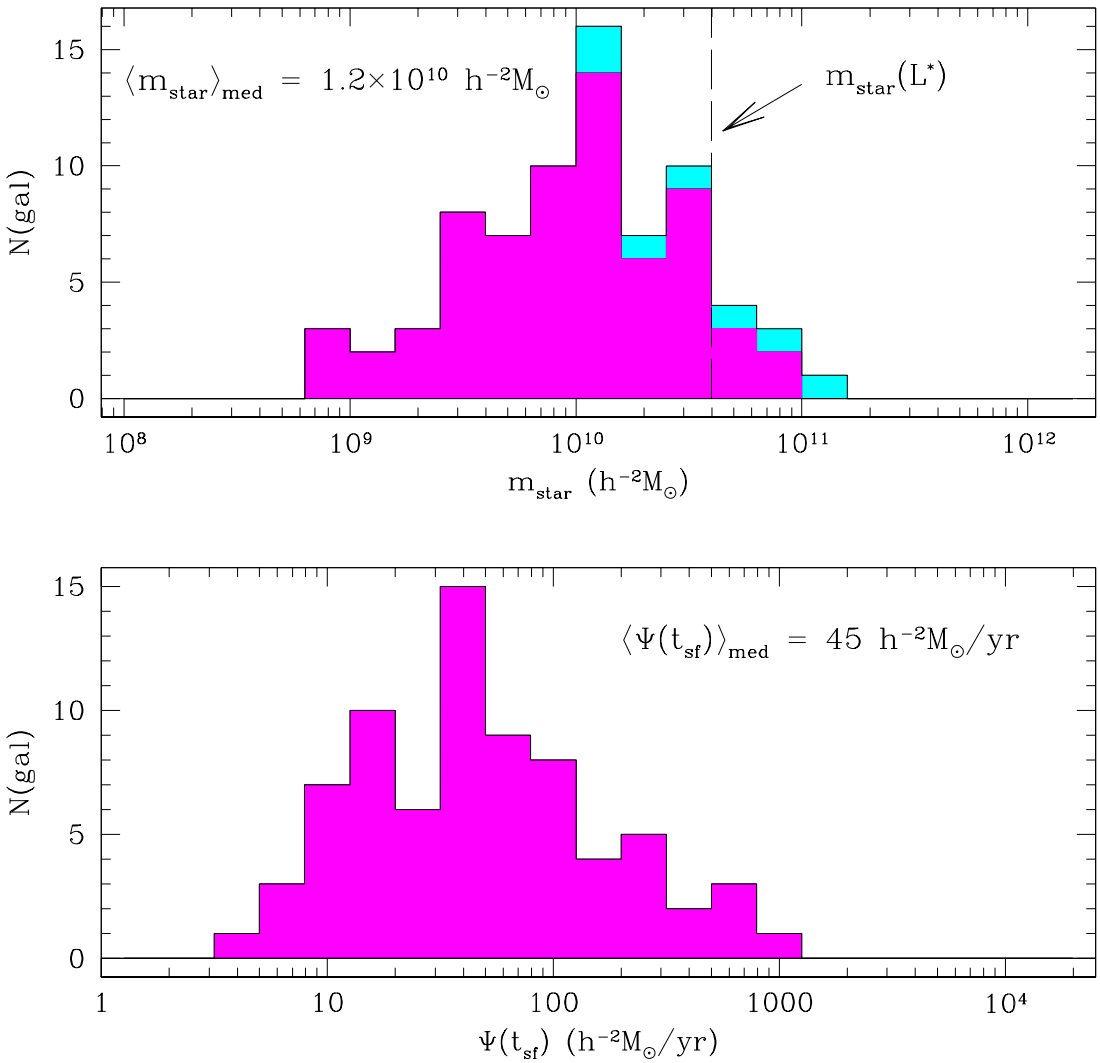

Fig. 10b.— Histograms of m_{star} and instantaneous star-formation rate, $\Psi(t_{sf})$, derived from the best-fit BC96 constant star-formation models. Top: The formed m_{star} distribution. The cyan (light grey) bins contain the seven galaxies with unconstrained best-fit t_{sf} values older than the age of the universe at $z \sim 3$. A significant fraction of the NIRC LBG sample have m_{star} values approaching the formed stellar mass in a current L^* galaxy ($4 \times 10^{10} h^{-2} M_\odot$), while a significant fraction have m_{star} values that are an order of magnitude smaller. Bottom: The distribution of instantaneous star-formation rates, determined by applying the inferred extinction corrections to the distribution of rest-frame UV luminosities.

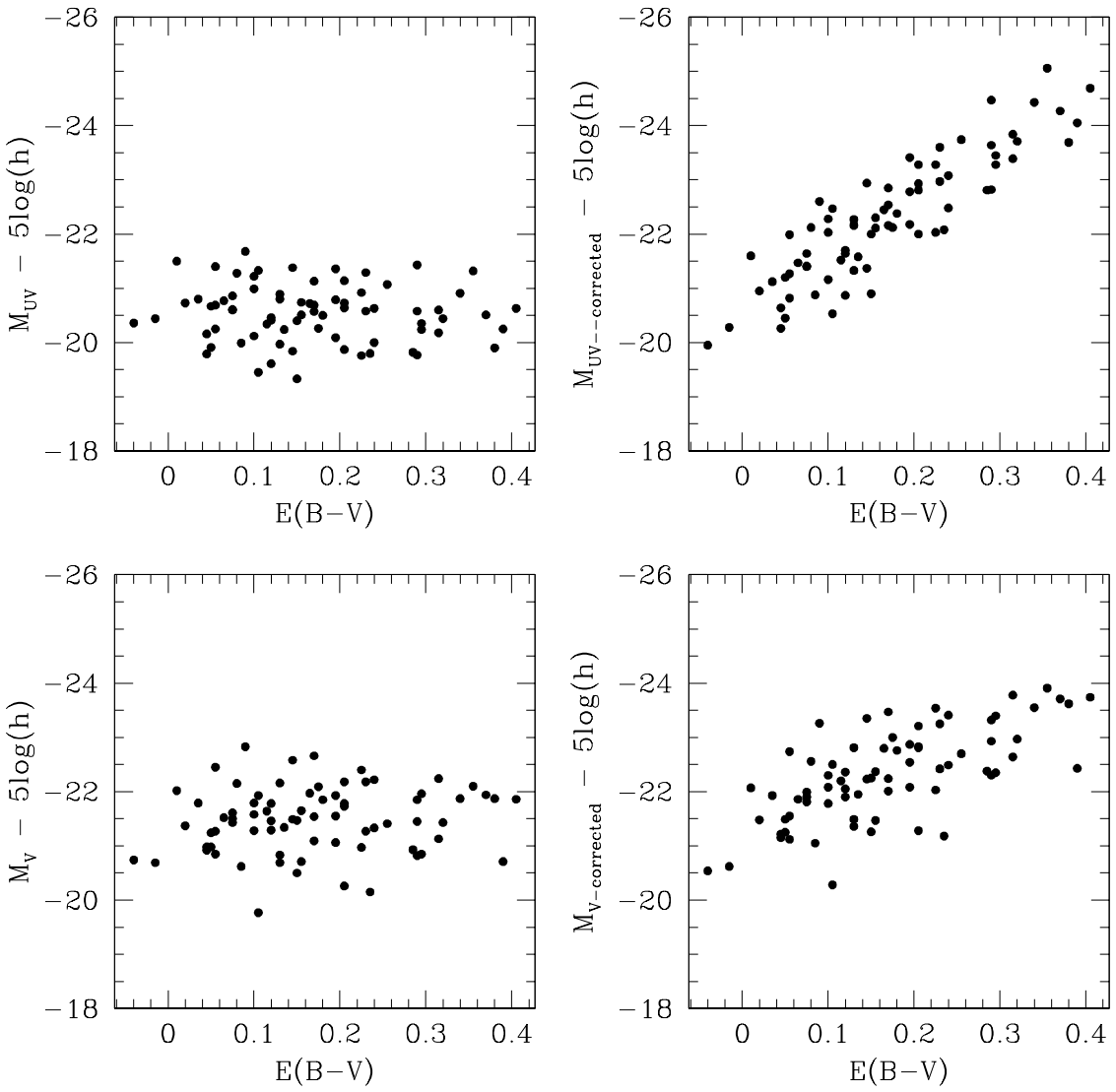

Fig. 11.— M_{UV} and M_V vs. $E(B-V)$. M_{UV} and M_V refer to the rest-frame UV and optical (V) absolute magnitudes which are probed by the $\mathcal{R}$ and K_s apparent magnitudes, respectively, at $z \sim 3$. The two left-hand panels show the relationship of rest-frame UV and optical luminosities with best-fit $E(B-V)$. Both UV and optical luminosities are uncorrelated with $E(B-V)$. When the luminosities are corrected for dust-extinction (shown in the right-hand panels), strong correlations result between intrinsic luminosity and dust extinction. The correlation holds not only in the rest-frame UV but also in the rest-frame optical, where the effects of dust-extinction are less extreme (but clearly still important, as shown by the lower right-hand panel). The correlation between intrinsic luminosity and dust extinction is independent of the star-formation history used to fit the observed spectral energy distributions.

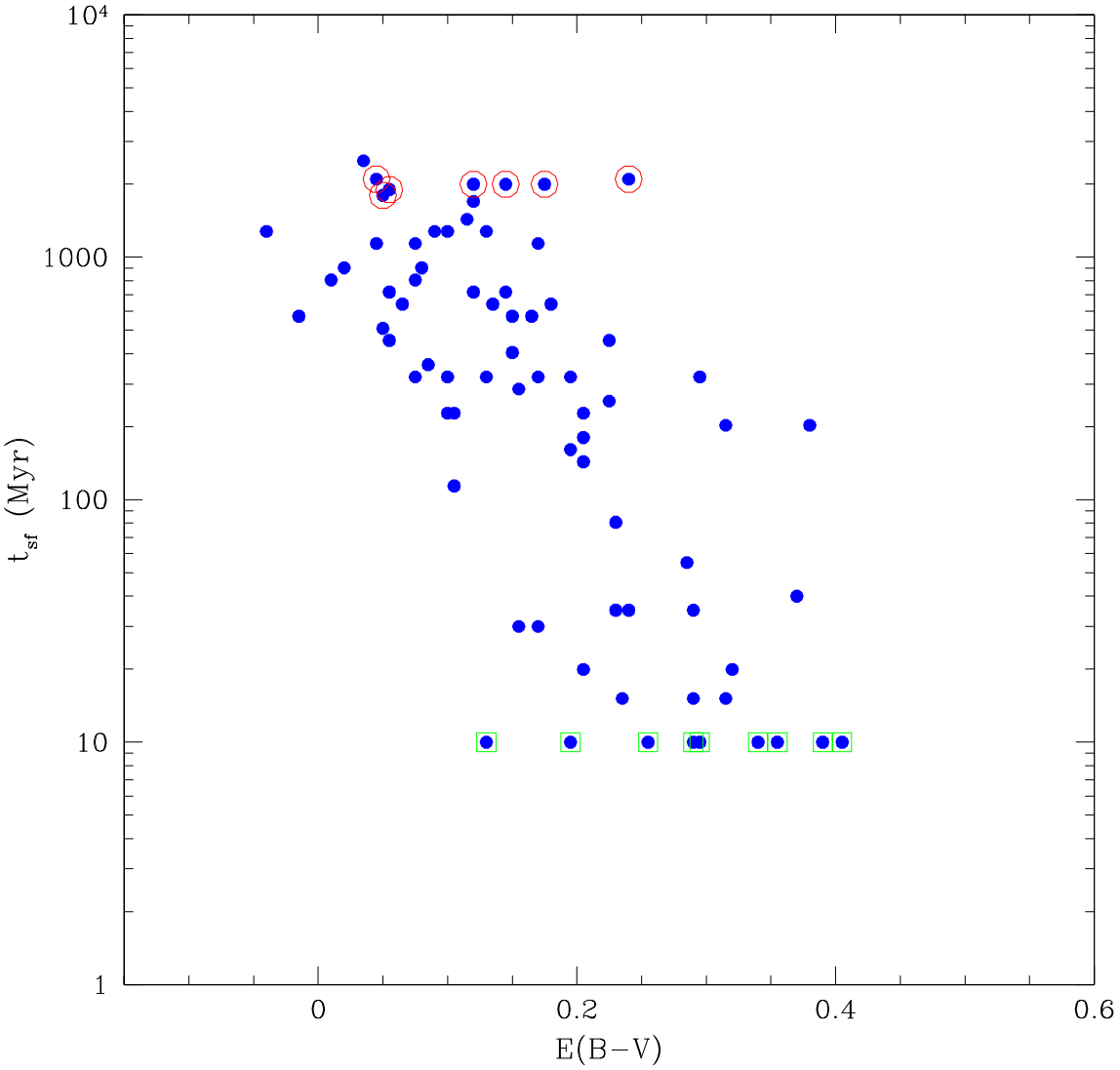

Fig. 12.— The Extinction-Age Correlation. This is the joint distribution of best-fit BC96 constant star-formation $E(B-V)$ and t_{sf} parameters. There is a significant correlation between the two best-fit parameters, which holds for all of the star-formation histories which we used to fit the observed spectral energy distributions. However, the strength of the correlation does depend on the assumed dust attenuation law. This plot assumes a Calzetti dust law, but if an SMC curve is used instead, the correlation is greatly reduced. Open circles indicate galaxies whose unconstrained best-fit t_{sf} values were older than the age of the universe at $z \sim 3$. Open squares indicate galaxies whose unconstrained best-fit ages are < 10 Myr.

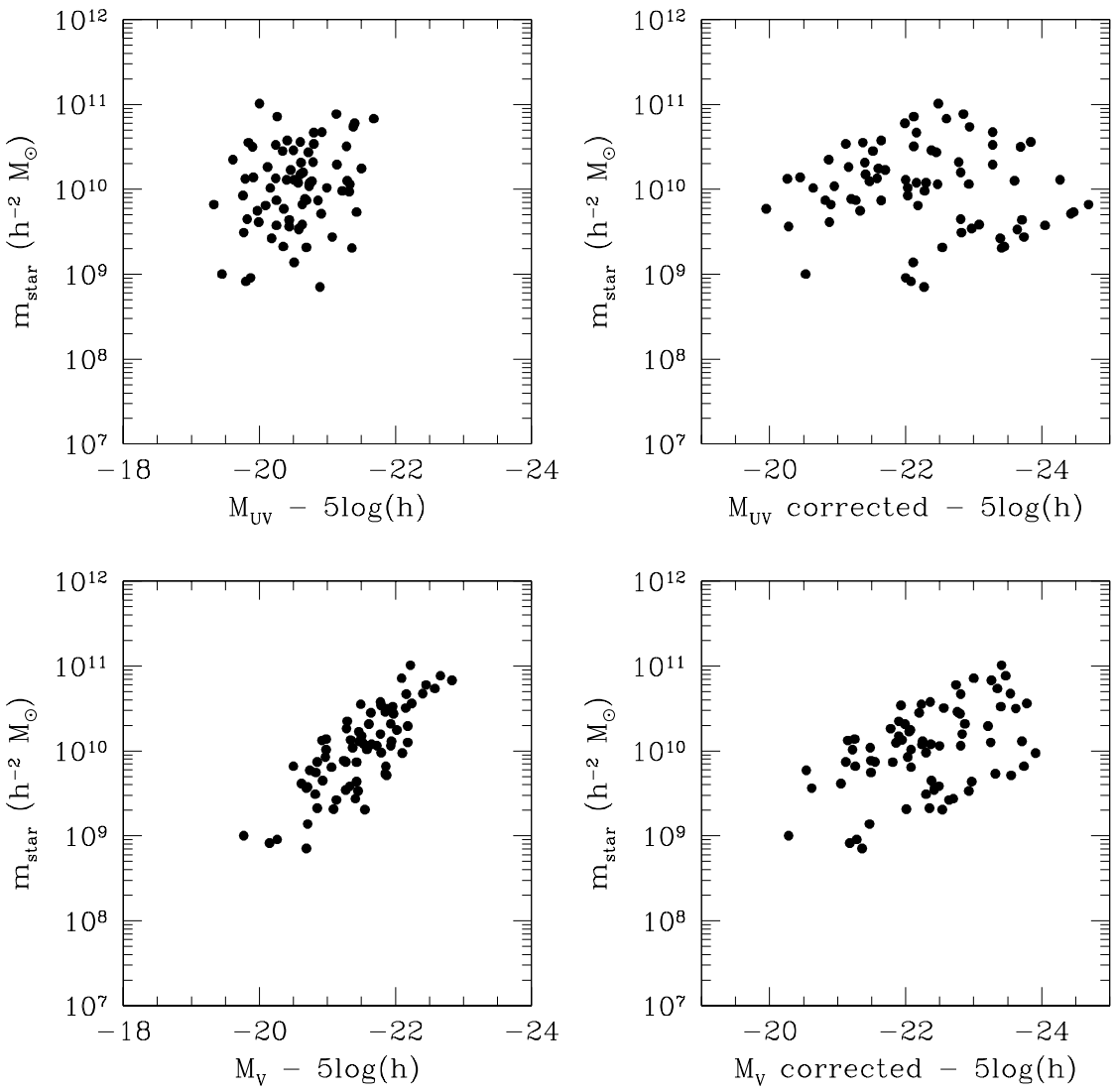

Fig. 13.— m_{star} vs. M_{UV} and M_V. Relationships are shown between m_{star} derived from the best-fit BC96 constant star-formation models, and the UV and optical luminosities. M_{UV} and M_V refer to the rest-frame UV and optical (V) absolute magnitudes. The left-hand panels show the relationships for luminosity which is uncorrected for extinction, while the right-hand panels show the relationships for extinction-corrected luminosity.

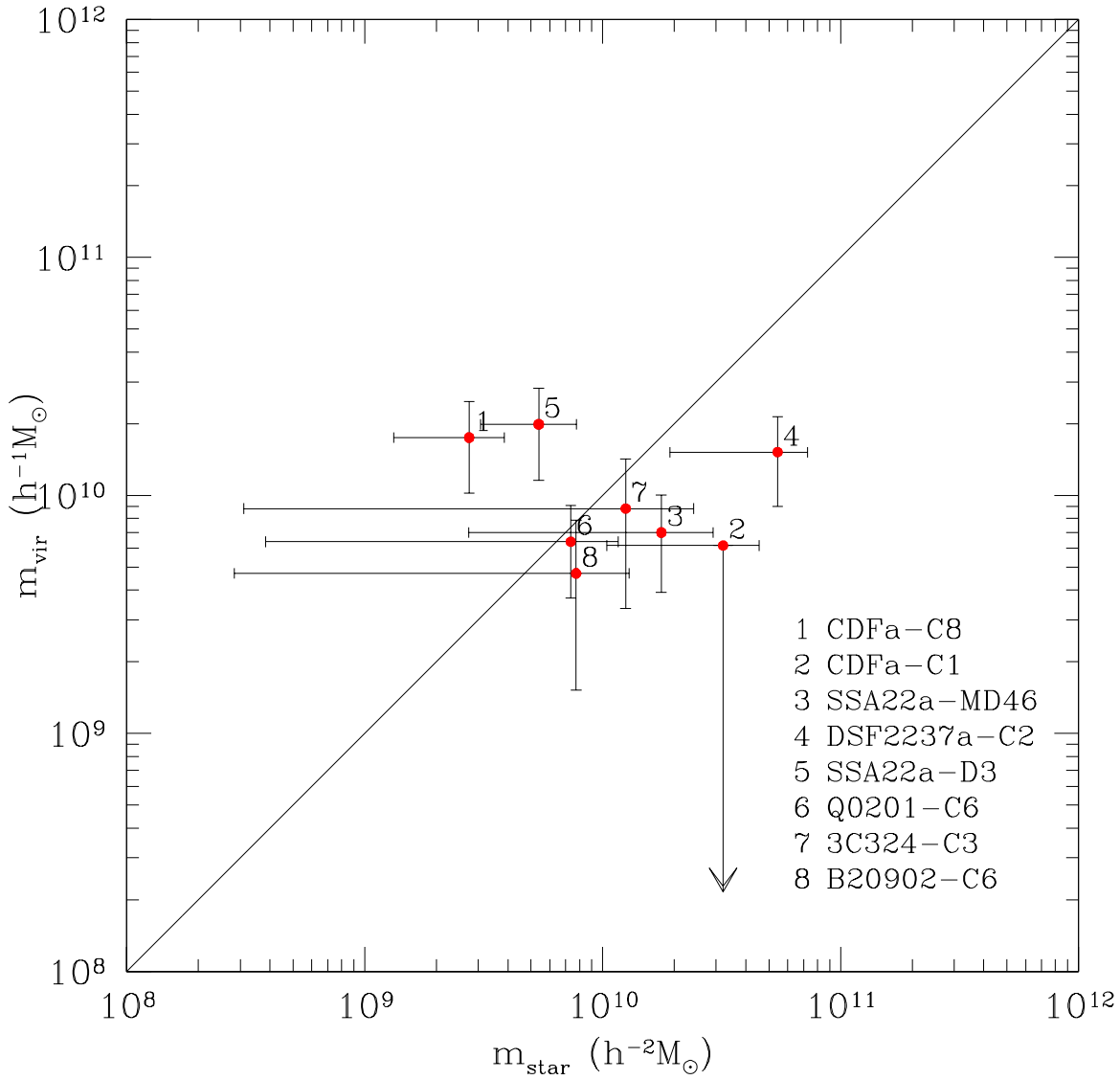

Fig. 14.— m_{vir} vs. m_{star}. This plot shows the relationship between the dynamical mass implied by nebular line widths, assuming virial equilibrium (m_{vir}), and the best-fit constant star-formation formed stellar mass (m_{star}). The solid line describes $m_{vir} = m_{star}$. Horizontal error bars reflect the 1σ model confidence region of m_{star}, while vertical error bars reflect the uncertainties in the measured nebular line width and angular half-light radius. The inferred dynamical masses should reflect approximate upper limits to the formed stellar mass in the physical region probed by the NIRC observations. We find broad consistency between the mass scales inferred from near-infrared spectroscopic and photometric measurements. In the two cases where there are significant differences, the best-fit stellar mass is significantly smaller than the inferred dynamical mass.

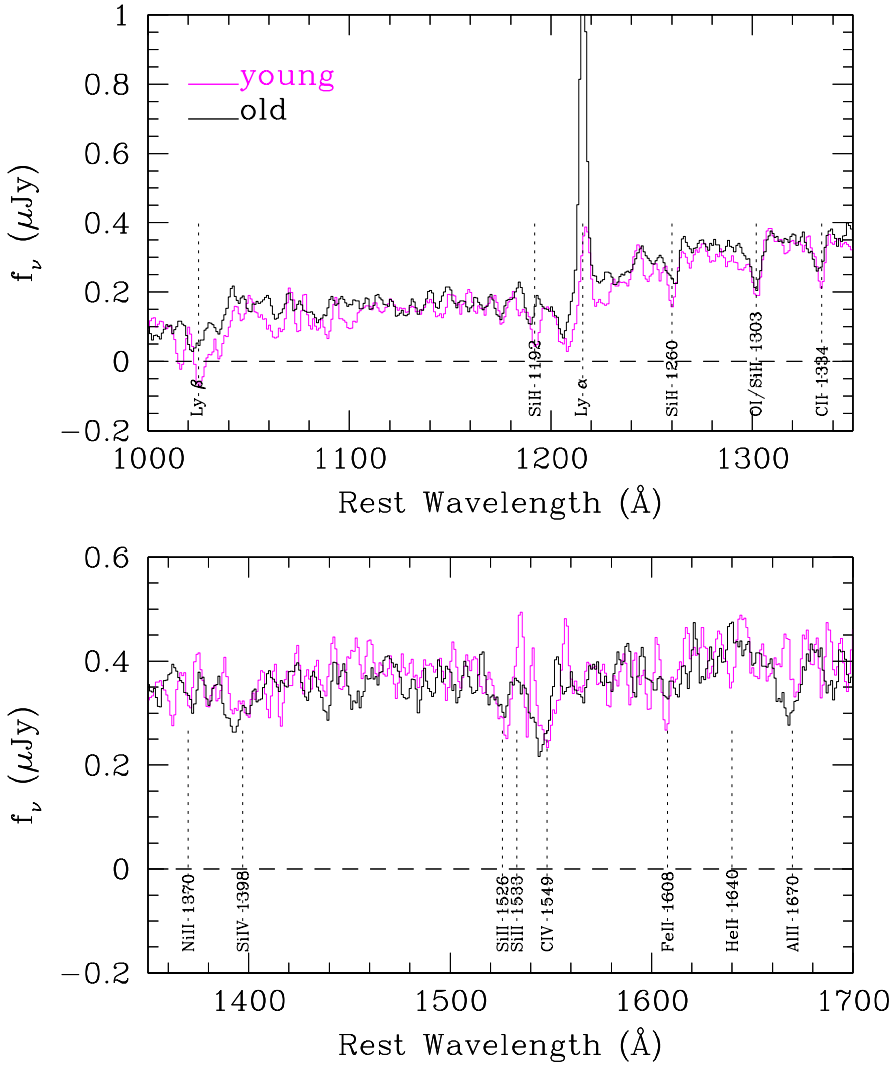

Fig. 15.— Comparison of "young" and "old" LRIS spectra. The composite spectrum of a subsample of galaxies with best-fit constant star-formation $t_{sf} \leq 35\,\mathrm{Myr}$ is shown in magenta (grey), while the composite spectrum of a subsample of galaxies with $t_{sf} \geq 1\mathrm{Gyr}$ is shown in black. The most striking differences between the two composite spectra are the relative strengths of Lyman-α emission; the relative strengths of the interstellar features Si II 1192, 1260, 1526 Å, CII 1334 Å, and Al II 1670 Å; and the relative CIV 1549 Å P-Cygni profiles.

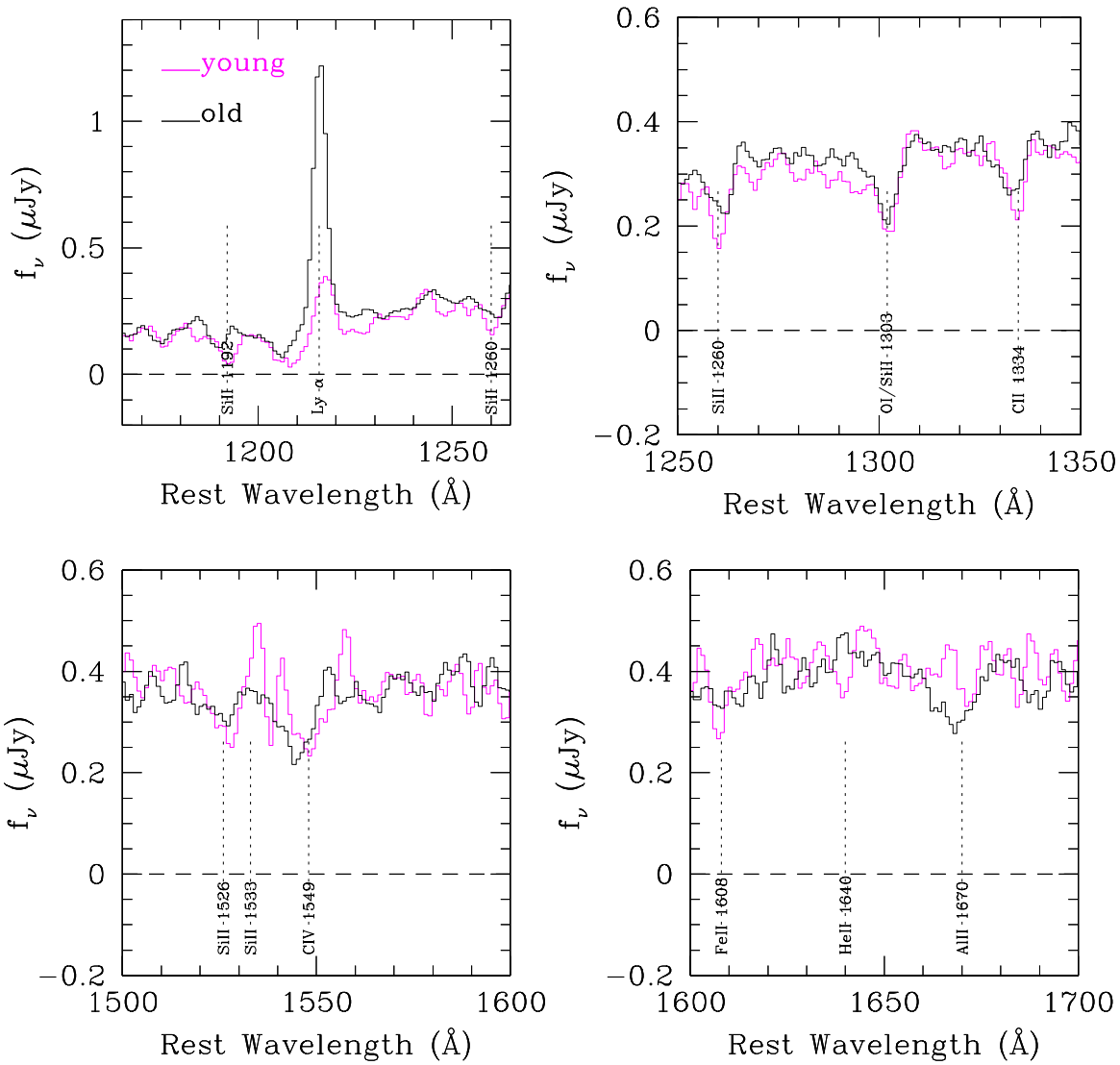

Fig. 16.— Zoomed in comparison of "young" and "old" LRIS spectra. Four regions of the composite young and old spectra are expanded for a more detailed view. The vertical axis of the detailed plot of Lyman-α spans a larger range in intensity than the other plots, for the purpose of showing the full extent of the strong Lyman-α emission in the old spectrum.